January 2013

Molecular Simulation For Neurodegenerative Diseases: From Modelling Alpha-Synuclein In Aqueous Solutions To Drug Delivery Systems

Erica Ann Hicks

Recommended Citation

Hicks, Erica Ann, "Molecular Simulation For Neurodegenerative Diseases: From Modelling Alpha-Synuclein In Aqueous Solutions To Drug Delivery Systems" (2013). *Theses and Dissertations*. 1543.
https://commons.und.edu/theses/1543

MOLECULAR SIMULATION FOR NEURODEGENERATIVE DISEASES: FROM MODELLING ALPHA-SYNUCLEIN IN AQUEOUS SOLUTIONS TO DRUG DELIVERY SYSTEMS

by

Erica Ann Hicks

Associate of Arts, Northland Community and Technical College, 2007
Bachelor of Science, University of North Dakota, 2011

A Thesis

Submitted to the Graduate Faculty

of the

University of North Dakota

in partial fulfillment of the requirements

for the degree of

Master of Science

Grand Forks, North Dakota
December
2013

This thesis, submitted by Erica Hicks in partial fulfillment of the requirements for the Degree of Master of Science from the University of North Dakota, has been read by the Faculty Advisory Committee under whom the work has been done and is hereby approved.

Dr. Jerome Delhommelle, Chairperson

Dr. Mark Hoffmann

Dr. Evguenii Kozliak

This thesis is being submitted by the appointed advisory committee as having met all of the requirements of the School of Graduate Studies at the University of North Dakota and is hereby approved.

Wayne S. Swisher

Dr. Wayne Swisher
Dean, School of Graduate Studies

December 12, 2013

Date

Title	Molecular simulation for neurodegenerative diseases: From modelling alpha-synuclein in aqueous solutions to drug delivery systems
Department	Chemistry
Degree	Master of Science

In presenting this thesis in partial fulfillment of the requirements for a graduate degree from the University of North Dakota, I agree that the library of this University shall make it freely available for inspection. I further agree that permission for extensive copying for scholarly purposes may be granted by the professor who supervised my thesis work or, in his absence, by the Chairperson of the department or the dean of the Graduate School. It is understood that any copying or publication or other use of this thesis or part thereof for financial gain shall not be allowed without my written permission. It is also understood that due recognition shall be given to me and to the University of North Dakota in any scholarly use which may be made of any material in my thesis.

Erica Hicks
December 20, 2013

TABLE OF CONTENTS

CHAPTER

LIST OF FIGURES

LIST OF TABLES

ACKNOWLEDGEMENTS

First off, this work would not have been possible without the special favor of God. He was my rock through the many trials I endured through my time as a graduate student. He gave me enough strength for each day, peace that surpassed all understanding, and unfailing love through the most difficult of times. I could not have managed this journey without him.

Next, I would like to thank my incredible and supportive husband, Jason. His sacrificial service, encouraging nature, and unfailing love, as exemplified in Corinthians 13:4-8, allowed me to thrive in graduate school. His patience is like no other I have seen. Even after getting extremely frustrated by problems, especially in homework, he would kindly and humbly stop what he was doing to help me with it.

I would like to express my deepest gratitude to the many supporters in my life. Where to even start? My parents, Tom and Linda, for their encouragement and my siblings, T.J. and Kya, who helped me keep my sanity. My grandma Ruth who loves unconditionally and gave me the determination to continue. My in-laws, especially Twyla, who prayed for me throughout graduate school. I would also like to thank Epiphany Station where I am constantly learning to live life to the fullest by, "Loving God. Loving People. Period."

I would like to especially thank my advisor, Dr. Delhommelle, and committee members. Their help with my research has been greatly appreciated. The School of Graduate Studies and the Chemistry Department have been incredibly helpful and knowledgeable. Finally, I would like to thank all the chemistry graduate students at UND for their friendship and willingness to help.

I would like to dedicate my thesis
in loving memory of my daddy-o, Tom Kastl.

ABSTRACT

Using computer simulations, we developed a better understanding of some key chemical steps of alpha-synuclein aggregation as well as amantadine for drug delivery systems. The aggregation and fibrillation of alpha-synuclein, a brain protein of 140 residues, has been linked to several neurodegenerative diseases, including Parkinson's and Alzheimer's diseases. Using molecular dynamics, α-synuclein, at various temperatures of 293 K, 310 K, 323 K and 348 K, was shown to undergo rapid conformational change. The non-amyloid-β component (NAC) of α-synuclein that is not sterically hindered is suspected to undergo aggregation.

Amantadine has been shown to help regulate the symptoms of Parkinson's disease, and single-walled carbon nanotubes (SWCNs) could be a potential drug carrier. Adsorption of amantadine within SWCNs, at differing diameters of 10.9 $\AA$, 16.3 $\AA$, 21.7 $\AA$ and 27.1 $\AA$, was studied using Expanded Wang-Landau (EWL) simulations. It was shown that increasing the diameters of the SWCNs increased amantadine loading - monolayers formed for the two smaller SWCNs while bilayers formed for the larger. The diffusion process was studied through molecular dynamics. For the larger two SWCNs, there was a dramatic decrease in the rate of self-diffusion with respect to increasing amantadine loading followed by a moderate decrease. This was attributed to the transition from a monolayer to a bilayer structure.

CHAPTER I

INTRODUCTION

1.1 Neurodegenerative diseases

α-synuclein plays a major role in neurodegenerative diseases such as Parkinson's disease, dementia with Lewy Bodies, multiple system atrophy, and Alzheimer's disease. The three most prevalent diseases in the U.S. will be discussed further, i.e. Parkinson's disease, dementia with Lewy Bodies, and Alzheimer's disease.

1.1.1 Parkinson's Disease

James Parkinson, a London physician, first identified Parkinson's disease (PD) in 1817 when he noticed patients exhibiting involuntary tremors observed especially in the limbs.[24] Parkinson's disease is defined as a neurodegenerative disorder that affects movement and coordination. It develops usually after the age of 50 but can occur earlier. In some cases, PD may be genetic. Currently, it is estimated that 500,000 Americans live with Parkinson's disease with 50,000 new cases every year. Due to an influx in baby boomers, these numbers are expected to rise.[25,26]

The cause of PD is due to its pathological characteristics of Lewy body (LB) formation and the progressive degeneration of dopaminergic neurons in the substantia nigra.[27] Lewy bodies are alpha-synuclein-immunoreactive inclusions that are found in the surviving nerve cells of the substantia nigra, see Figure 1 below.[6]

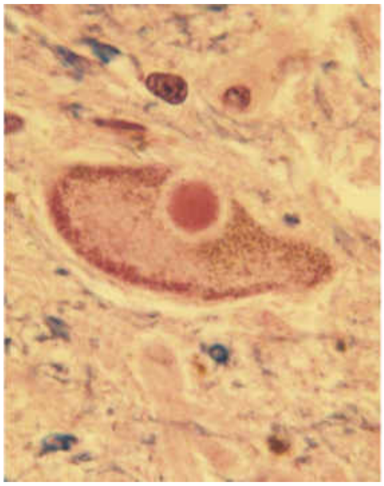

Figure 1. A typical Lewy body found in a dopaminergic neuron in the substantia nigra. The red circle contained in the cytoplasm is the LB.[1]

A Lewy body is created from an abnormal accumulation of aggregated filaments which include alpha-synuclein as well as many other proteins involved in proteolysis, i.e. breakdown of proteins into polypeptides or amino acids, see Figure 2.

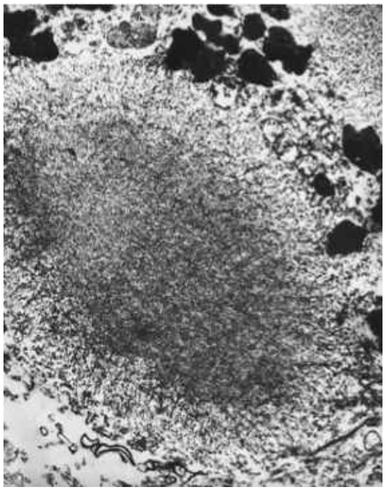

Figure 2. A Lewy body showing the accumulation of mainly α-synuclein.[1]

As mentioned previously, PD is also characterized by the loss of dopamine releasing neurons. The loss of neurons occurs throughout specific brain regions but none are more prevalent than in the substantia nigra especially in the pars compacta. In this region there are approximately 450,000 dopaminergic neurons.

The symptoms of PD usually will not occur until 60 to 70 percent of the dopaminergic neurons have died in this region. The mechanism behind this kind of cell death is unclear but many believe that Lewy bodies contribute. Growing evidence suggests that nerve cell death may be apoptotic in the pars compacta region. This refers to the decomposition of cells into membrane-bound particles which are removed through phagocytosis or by shedding. However, others suggest that neuronal degeneration could be a cause of mitochondrial dysfunction, oxidative stress, action of excitotoxins, deficient neurotrophic support, and immune mechanisms.[1]

The major symptoms of PD are described by resting tremors (tremors that occur when the individual is at rest); symptoms include uncontrollable shaking of limbs, especially hands and fingers), muscular rigidity, bradykinesia (slowness of movement) and postural instability.[28] In some cases, dementia can occur leading to Parkinson's disease with dementia (PDD). As the nerve cells die in the brain, dopamine is not readily available causing a decrease in fluid muscle movement.

As of yet, there is no cure for Parkinson's disease, barring the drugs that can help manage its symptoms. Most of the drugs are used to release dopamine in the brain. The most common and effective drug is levodopa. Levodopa is transported to the brain's nerve cells and is converted into dopamine. This allows the nerve cells to use it as a neurotransmitter.[29]

Due to the degenerative nature of Parkinson's disease, patients may become completely debilitated. Though PD is not a fatal disease, the secondary complications may lead to death, i.e. pneumonia, falling, and choking

1.1.2 Dementia with Lewy Bodies

Dementia with Lewy bodies (DLB) is believed to be the second most common type of degenerative dementia, the first being Alzheimer's disease, and accounts for 10-15 % of patients with dementia,[30] roughly 1.3 million Americans. It mainly affects individuals who are over the age of 60. DLB occurs when α-synuclein aggregates to form insoluble fibrils which are the major contributor to Lewy bodies, as mentioned previously.[31] These Lewy bodies prevent proper cell functioning and viability.

First identified in the mid-1990s, DLB shares similarities to Parkinson's disease with dementia (PDD). The main difference is that in PDD, dementia occurs after more than one year of parkinsonism while DLP can occur either before, simultaneously, or within one year of parkinsonism.[32]

The major symptoms of DLP are cognitive impairment, recurrent visual hallucinations and parkinsonism.[33] Visual hallucinations and delusions are the result of more abundant Lewy bodies in the temporal cortex than that of PDD.[34] Like Parkinson's disease, there are only drugs that can help with the symptoms; there is no cure. The most common drugs used are those that are involved with Parkinson's disease and Alzheimer's disease.

1.1.3 Alzheimer's Disease

Alzheimer's disease (AD) was identified in 1906 by a German neuropathologist and psychiatrist Alois Alzheimer. AD is the sixth-leading cause of death and affects 5.3 million Americans.[35] This disease also accounts for more cases of dementia than any other disease.[36] Worldwide, it is estimated that over 26.6 million people have AD and, by 2050, it will quadruple to 106.8 million[37]

The majority of AD patients is over the age of 65 but it can develop as early as the patient's 40's (early onset AD), although this is more rare. The major risk factor is age. For people over the age of 65, the risk doubles every five years. By the age of 85, nearly half of all people are affected. The progression of AD can last up to twenty years depending on the health and age of the individual.[38] Due to the progressive nature of this neurodegenerative disease, it can be divided into three main stages: mild, moderate, and severe. In the mild stage, plaques and tangles (types of proteins) form in the brain. Here, patients show trouble with memory and thinking. In the moderate stage, more plaques and tangles are formed causing significant memory loss. Patients also experience trouble speaking and changes in personality and behavior. In the severe stage, plaques and tangles have spread to the cortex. Because of cell death, the brain shrinks. Patients are unable to communicate coherently and require total assistance for personal care because of the disease's debilitating nature.[39]

Associated with Alzheimer's disease is the build-up of proteins. There are two types of protein accumulation: plaques and tangles, see Figure 3. Plaques exist outside the neurons in the brain while tangles exist inside the neuronal cell. It is common for these types of proteins to develop in the brain as individuals age, but, for AD patients, the production is much greater. Although researchers are not sure what role these proteins play in AD, one suggestion is that they block neuron signals which make it difficult for the nerve cell to survive.

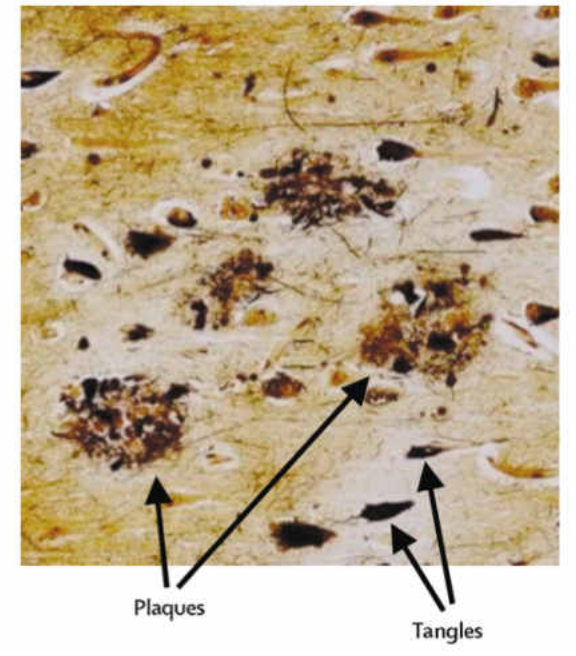

Figure 3. Plaques and tangles of Alzheimer's Disease.[2]

Plaques of AD consist of Amyloid-β (Aβ) peptides. These peptides are formed when the amyloid precursor protein, found in neurons, undergoes abnormal proteolysis, due to a gene mutation. Aβ peptides aggregate in the extracellular milieu forming toxic soluble oligomers during the first stage of self-assembly. The Aβ monomers aggregate through multiple pathways and at different rates. The results are a metastable mixture where oligomeric assemblies are noncovalently associated. It has been proposed that alpha-synuclein may aid, in some way, in the aggregation of these peptides.[40]

In both DLB and AD, it has been shown that cognitive abilities are lost through synaptic degradation[41] and that α-synuclein plays a crucial role in the pathogenesis of these diseases.[42] It has been proposed that misfolded α-synuclein causes this.[43]

Like the other previous diseases mentioned, there are no cures for AD - only drugs that can help with the symptoms. The drugs for AD are cholinesterase inhibitors that help stop the decomposition of neurotransmitters. Still another drug may be used for the regulation of glutamate by helping block NMDA receptors.

1.2 Self-Assembly

Before delving into the subject of aggregation of α-synuclein, it is important to first introduce the nature of the protein.

α-synuclein is found mainly in the presynaptic nerve terminal[44] and the normal behavior of this protein is not clearly understood. Some of the presumed functions include regulation of synaptic plasticity, neuronal differentiation, and dopamine release, see Figure 4. Synaptic plasticity refers to the synapse's ability to change in strength for different responses. α-synuclein has been shown to play a role at synapses by interacting with brain vesicles and phospholipid membranes.[45,46] Neuronal differentiation refers to the ability of α-synuclein to assist in the development of neurons from other types of cells such as oligofendrocytes or astrocytes. This has been shown in several different studies.[47–49] α-synuclein may also inhibit dopamine release due to interactions with vesicle membranes.[50] It is uncertain whether α-synuclein induces cell death (apoptosis) or protects cells.[3]

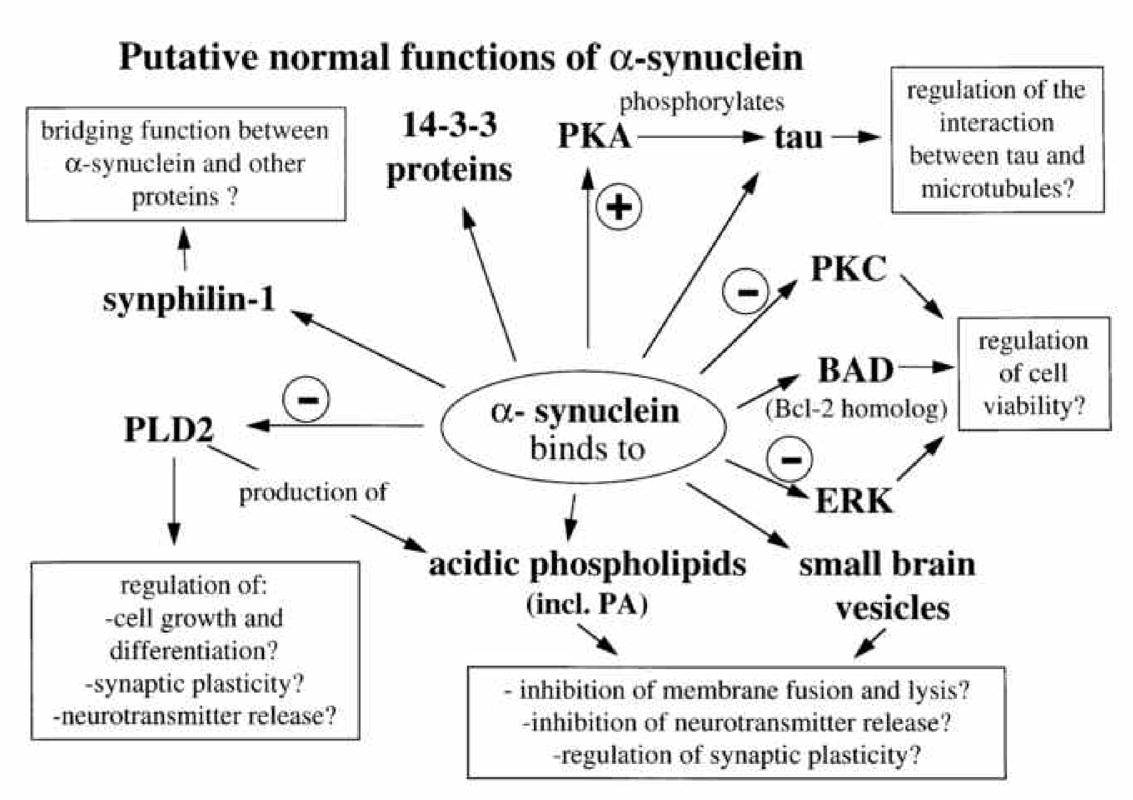

Figure 4. Presumed normal function of α-synuclein. "-" means enzyme inhibition while "+" indicates enzyme activation from α-synuclein. The molecules are: PA, phosphatidic acid; PLD2, phospholipase D2; PKC, protein kinase C; PKA, protein kinase A; ERK, extracellular-regulated kinase.[3]

α-synuclein consists of 140 amino acids which can be divided into three main regions. The first region, residues 1-60, consists of an amphipathic N-terminal region, which shows an alpha helix structure. Residues 61-95 contain a hydrophobic region where aggregation usually occurs. The third region, residues 96-140, contains a highly acidic C-terminal,[51] see Figure 5 below.

The synthesis of α-synuclein is encoded by the SNCA gene, synuclein, alpha (non a4 component of amyloid precursor). Problems can occur when the synthesis of α-synuclein leads to a mutated form or an excess of the protein. Mutations of α-synuclein, resulting in a misfolded configuration, occur when alanine is replaced

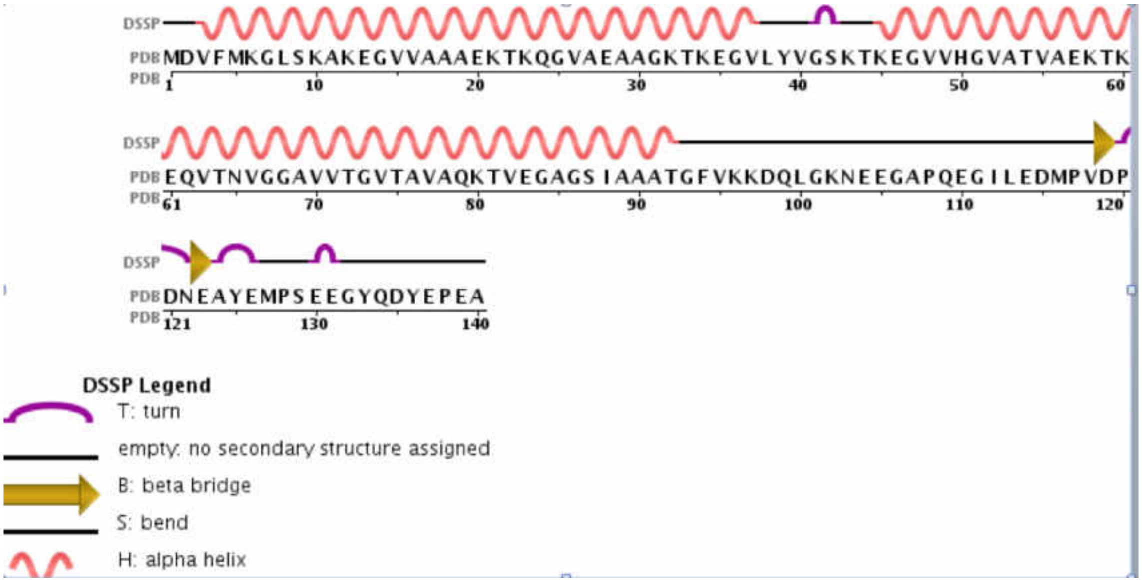

Figure 5. α-synuclein showing turns, beta bridges, bends, and alpha helices. Letters represent amino acids.

by another amino acid at positions 30[52] or 53.[53] SNCA can also be inappropriately duplicated or triplicated resulting in excess α-synuclein.[54] When α-synuclein is in its mutated form or when there is an excess, it becomes a toxic protein since α-synuclein can act as a nucleation/seeding agent for aggregation.[55] This leads to an increase in neuronal cell death which causes the various neurodegenerative diseases. Therefore, understanding the mechanism behind aggregation is crucial as it could allow for drug development for the various diseases.

The aggregation mechanism that produces insoluble forms of α-synuclein is unknown.[56] Prior work has shown that aggregation starts when α-synuclein undergoes a conformational change to form a partially folded intermediate. Several of these intermediates may then aggregate to form oligomers, amorphous aggregates or fibrils.[57] This aggregation leads to Lewy body formation which has been mentioned previously. A representation of the different stages of folding for α-synuclein can be seen in Figure 6.

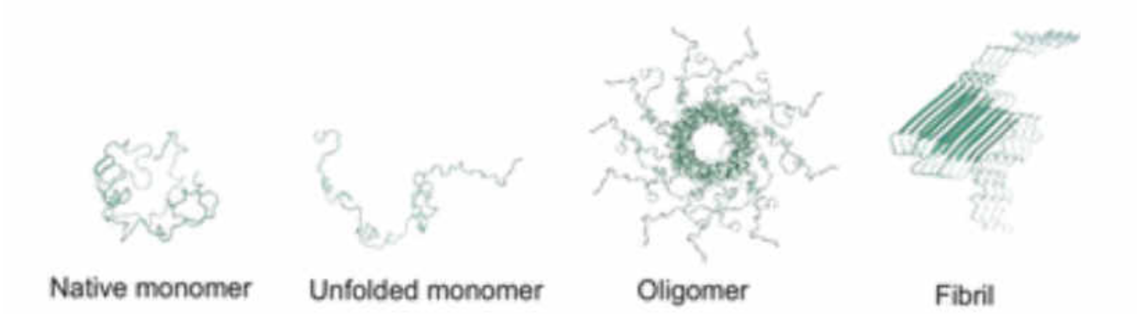

Figure 6. α-synuclein in different stages of aggregation[4]

A general overview of the aggregation and the events leading to toxicity can be seen in Figure 7. The middle column shows the main pathway of aggregation. Here, α-synuclein is natively unfolded and can bind to membranes or start forming oligomeric species. These oligomers are then stabilized by β-sheet-like interactions. Later, this will turn into insoluble fibers leading to Lewy bodies. The left column contains known modifiers that have been shown to increase the aggregation process. In the right column are cellular structures that have been suggested to be affected by the aggregation of α-synuclein.[5]

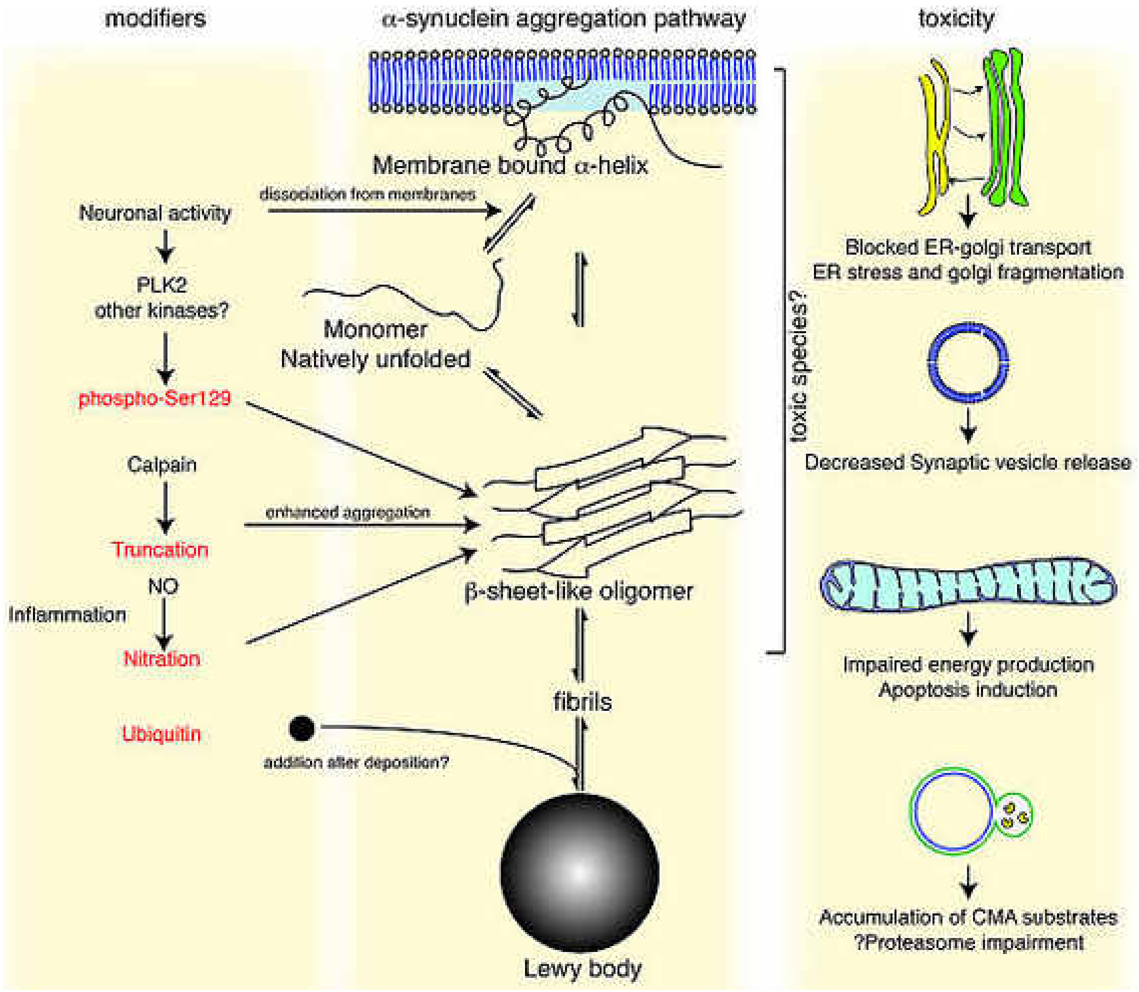

Figure 7. Pathway of α-synuclein aggregation leading to toxicity to proposed cellular structures.[5]

Behind aggregation, there are a number of different factors that could lead to cell death as can be seen in the outline of Figure 8. We will discuss a few of these factors that can lead to an increase in aggregation.

The first factor that could increase aggregation is protein mutation. Comparing the A30P and A53T mutations with wild-type (WT) α-synuclein, it was demonstrated that the rate at which aggregation occurred was fastest for the A53T mutant, followed by the A30P mutant and finally, the WT α-synuclein.[58] It was shown that A30P formed fibrils at a slower rate than the other two.[59] However, A30P formed oligomers that could even be more toxic than fibrils. This mutation

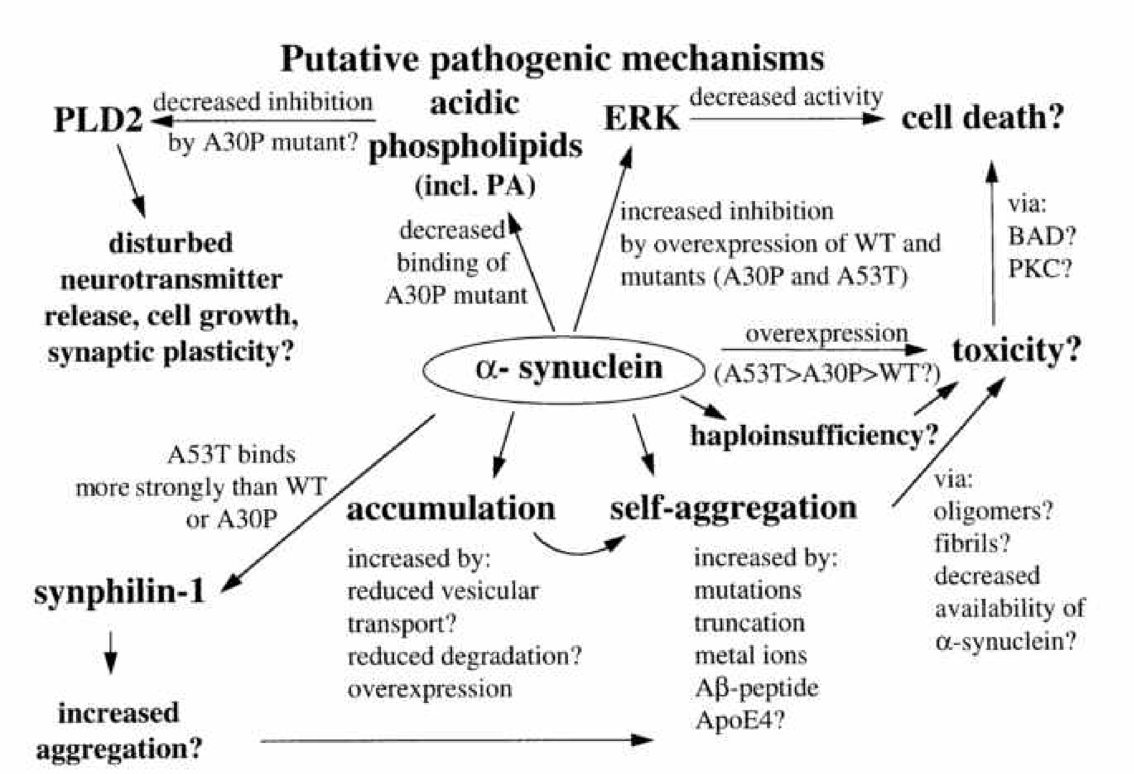

Figure 8. Possible mechanisms behind α-synuclein aggregation. The molecules are described by: PA, phosphatidic acid; PLD2, phospholipase D2; ERK, extracellular regulated kinase; WT, wild type; A30P and A53T are α-synuclein mutations.[3]

also led to α-synuclein's inability to bind to vesicles. Becuase α-synuclein could no longer do its normal function, it has been thought that this could lead to an increase in concentration within the cell body. This accumulation could lead to aggregation, which would result in the formation of Lewy bodies.[45]

The second factor is truncation. The truncated form of α-synuclein, i.e., residues 1-120, were found to be more likely to form filaments compared to that of the full α-synuclein, i.e., residues 1-140.[60]

The occurrence of metal ions is the third factor. One example is the Fe^{3+} ion. It was shown that if these ions were found in the substantia nigra, there was an increase in aggregation of α-synuclein.[61] Finally, it was shown that Aβ25-35 fragments promotes oligomerization of α-synuclein.[62]

After fibrillization has occurred, Lewy body formation will appear. Lewy bodies are made up of filaments that are between 7 to 15 nm long and arranged either radially or randomly. This abnormal accumulation can be either age or disease related. They are found within the substantia niagra, although finding them in brainstem neurons are one of the diagnostic criteria for Parkinson's.[63] Due to this feature, their structure and composition (found by staining with eosin) may change slightly. LBs are found within the cytoplasm of the cell (intracytoplasmic). Most LBs are round (between 5 to 25 μm) and surrounded by a halo when stained, see Figure 9 below. Some Lewy bodies occur elongated or are complex in shape.[64] Also, some will exhibit darker centers (cores) and/or darker rings (laminae).

Figure 9. A LB showing the core (C), body (B), and halo (H).[6]

1.3 Outline

This thesis will be divided into several parts. The first will include recent experimental and molecular simulation results. Next, the basis of molecular dynamics as well as key properties will be discussed. Then, α-synuclein, in a system of water and ions, will be looked at. Finally, the latter will lead into using computer simulations for potential drug delivery systems, specifically amantadine and carbon nanotubes.

CHAPTER II

STATE OF THE ART

2.1 Recent experiments/treatments

As mentioned previously, the accumulation of α-synuclein and Lewy body formation are the attributes of various neurodegenerative diseases. The progressive nature of these diseases is a direct result of the spread of Lewy pathology. For example, in PD patients, α-synuclein aggregation starts in the lower brainstem and olfactory bulb and spreads into the limbic system and finally into the neocortex.[65] It has been shown that the spreading, which could be a result of pathological propagation, of the Lewy pathology, can occur from a host tissue to grafted neurons within the brains of PD patients.[8,66,67] However, the mechanism behind the spreading is unknown and will be further looked at through recent experimental studies.

α-synuclein was thought to be an intracellular protein localized mainly in the the cytosol with a small portion found in vesicle fractions.[68,69] However, later α-synuclein was found in human CSF and blood plasma.[70,71] Due to these findings, α-synuclein secretion from the cell through exocytosis was investigated. It was found by Lee et al. that the small portion of the protein contained in the lumen of vesicles could be released through an unconventional exocytic pathway. Additionally, the α-synuclein found in the vesicles was more prone to aggregation and this aggregated substance could also be secreted.[7]

Overexpression of human α-synuclein in differentiated SH-SY5Y human neuroblastoma cells was shown to release the protein in a culture medium after 2 hours and accumulated thereafter, see Figure 10. This proposes that α-synuclein is constitutively secreted by exocytosis. Lee et al. then showed that the release of the protein was not due to byproducts of overexpression or to leakage of the membrane due to a dying cell by the following: (1) when the protein, β-galactosidase, was overexpressed in SH-S5Y, it was not discovered in the medium, unlike α-synuclein; (2) there was a clear correlation to the amount of α-synuclein released to that of intracellular expression levels; (3) when α-synuclein was followed over time by pulse labeling with ^{35}S, the quantity of the protein in the medium reached a saturation point in 2 hours. This signifies that the secretion of α-synuclein could not be due to membrane leakage as there would be a continuous supply of this protein in the medium; (4) α-synuclein that had been secreted was found in the medium containing rat primary cortical neurons. This suggests that neuronal endogenous α-synuclein can also be constitutively released.[7]

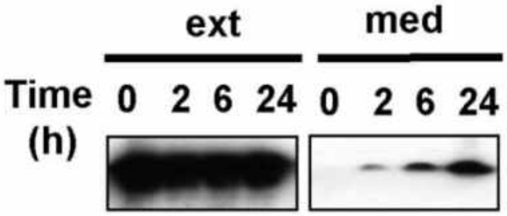

Figure 10. Secretion of α-synuclein using Western blotting. The whole-cell extracts (ext) and medium (med) were obtained at the designated times.[7]

Exocytosis is inhibited by low temperature, which is a classical blocker for vesicular exocytosis. To determine if the α-synuclein released was mediated by this process, SH-SY5Y cells, which had an overexpression for α-synuclein, were incubated at two different temperatures, 18°C or 37°C. At 18°C, the release of α-synuclein was greatly reduced indicating that its secretion is due to exocytosis, see Figure 11.[7]

The mechanism behind α-synuclein release into a medium is uncertain. It was shown that α-synuclein lacks a signal sequence, which was somewhat unusual since it still could be secreted from the cell. Other studies have shown that similar proteins that lack a signal sequence could be secreted from the cell through nonclassical vesicular exocytosis.[72,73] These proteins are resistant to BFA, which is a

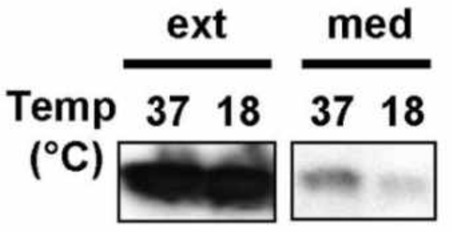

Figure 11. The release of α-synuclein is blocked at low temperature, i.e. 18°C. The whole-cell extracts (ext) and medium (med) were obtained at 3 hours. Results were obtained through Western blotting.[7]

classical inhibitor of endoplasmic reticulum (ER)/Golgi-dependent protein secretion. SH-SY5Y cells that expressed α-synuclein were studied with and without BFA. α-synuclein was pulse labeled with ^{35}S so it could be tracked. It was shown that in the presence of BFA, α-synuclein secretion was greatly reduced, showing that the classical export pathway was disrupted. However, the protein was still released indicating that the secretion is from an unconventional export pathway, which is ER/Golgi-independent, see Figure 12.[7]

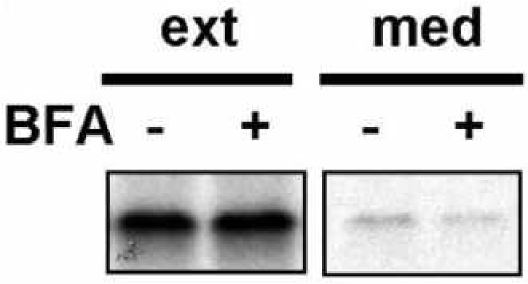

Figure 12. BFA does not block the secretion of α-synuclein. Thus, there is some other type of secretion mechanism that does not rely upon ER/Golgi-related classical vesicular transport.[7]

Aggregation of α-synuclein in three different brain fractions, i.e. P3 (microsomal vesicles), LP2 (crude synaptic vesicles) and S3 (cytosol), were observed. It was found that high-molecular-weight aggregates occurred more quickly in P3 and LP2 vesicle fractions than in S3, see Figure 13. It was also shown that the vesicles from SH-SY5Y cells had an increase in aggregation rate, which had been created from the intravesicular α-synuclein instead of cytosolic contaminants or vesicle-surface-bound α-synuclein, compared to that of the cytosol. This was also found to be true in intact cells of SH-SY5Y, see Figure 14. The aggregation of α-synuclein occurs faster in the vesicle lumen than that of the cytosol.[7]

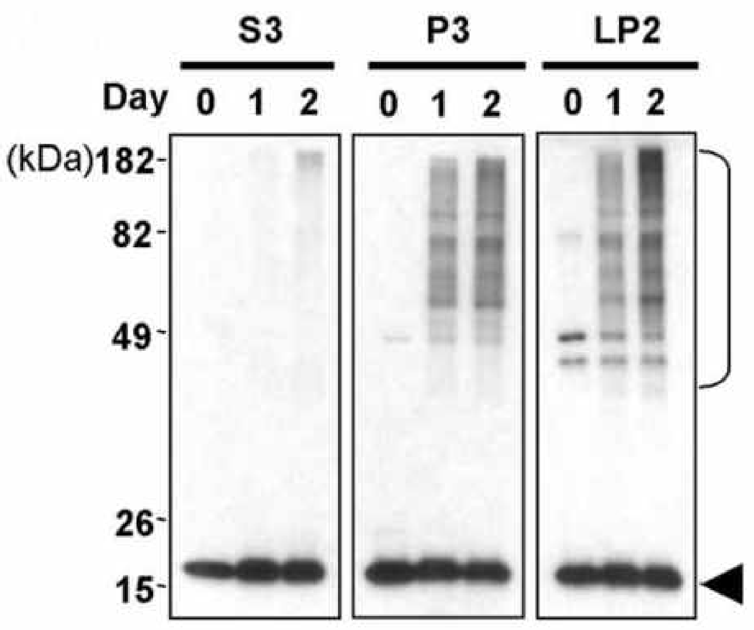

Figure 13. S3, P3, and LP2 brain fraction aggregation rates for α-synuclein. The vesicles, i.e. P3 and LP2, had an increase in aggregation compared to that of the cytosol, i.e. S3. The bracket indicates high-molecular-weight aggregates, while the arrowhead indicates monomeric α-synuclein. Aggregation was observed through Western blotting.[7]

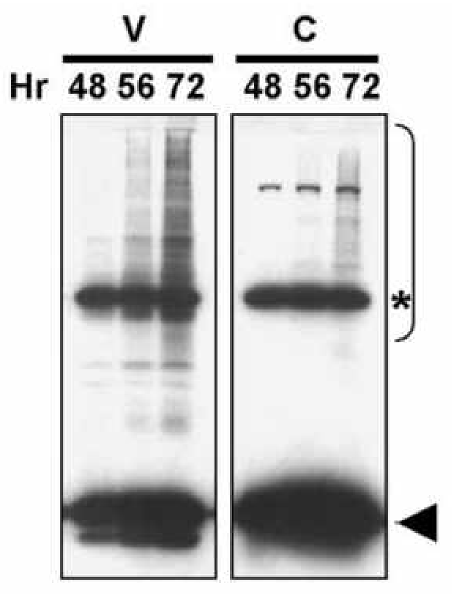

Figure 14. Vesicles, V, versus cytosol, C, aggregation. A bracket indicates high-molecular-weight aggregates, an arrowhead indicates monomeric α-synuclein, and an asterisk indicates an side protein that cross-reacts with Syn-1 antibody.[7]

It has been shown that at low levels of α-synuclein expression in SH-SY5Y cells, only monomeric α-synuclein is present in both cell extracts and in the medium. At higher levels, α-synuclein aggregated within the cell and the accumulated mass was secreted, see Figure 15A. Like that for α-synuclein, aggregates of α-synuclein were secreted through exocytosis since inhibition occurred at low temperatures, i.e., a classical blocker for vesicular exocytosis, see Figure 15 B.

So far, we have been discussing α-synuclein secretion through an exocytosis pathway. We will now consider the uptake of the protein through endocytosis.

Extracellular α-synuclein aggregates (fibrils, oligomers, and monomers) were studied since they have been shown to cause neurotoxicity to surrounding cells. It was demonstrated that these aggregates were internalized through endocytosis, which ultimately led to the degradation of the proteins. The internalization of fibrils was demonstrated to go through endocytosis-mediated internalization since the uptake of α-synuclein from a cultured medium could be blocked by both low temperature and the expression of dynamin-1 K44A, which is a dominant-negative

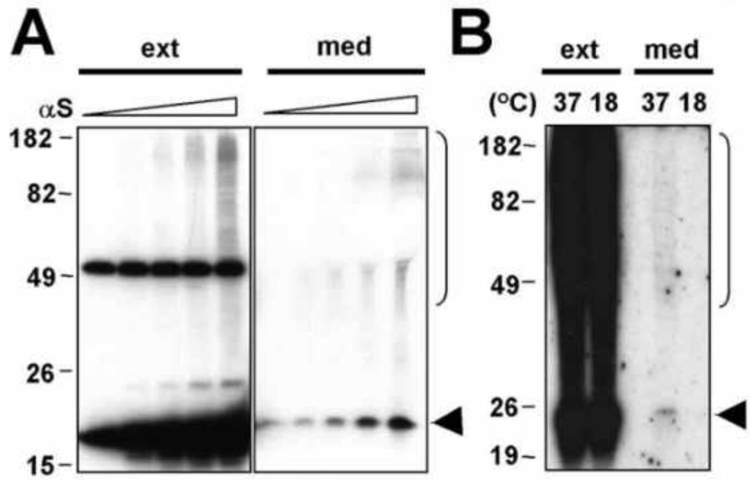

Figure 15. (A) Release of α-synuclein at increasing levels of expression in SH-SY5Y. Proteins released were collected for 16 hours. A bracket indicates high-molecular-weight aggregates, an arrowhead indicates monomeric α-synuclein, "ext" indicates whole-cell extracts and "med" indicates the conditioned medium. (B) Release of α-synuclein aggregates is blocked at low temperature.[7]

mutant. Once internalized, the fibrils migrated through the endosomal pathway and were degraded within the lysosome. Similarly, oligomers were internalized through endocytosis and were degraded by the lysosome. Monomers were shown to be impervious to low temperature and dynamin-1 K44A signifying the direct translocation across the plasma membrane. The monomers are then degraded by the cellular proteolytic system. These discoveries may imply that the removal of extracelluar aggregates of α-synuclein occurs through the, uptake of the aggregates through endocytosis, followed by a transportation of the endosomal pathway and then finally degraded by lysosomes.[74]

There have been investigations on transplantation of neurons into patients with Parkinson's disease that have shown, years later, i.e., between 11 and 16 years, that the grafted cells tested positive for α-synuclein and contained Lewy body-like inclusions.[66,67] This observation demonstrates that progression of α-synuclein can occur from host to grafted neuron cells.

Since previous studies have shown that neurons are capable of internalizing extracellular aggregates of α-synuclein through endocytosis,[74] mouse cortical neuronal stem cells (MCNSCs) were tested to determine if a similar process could occur. Through Western blotting and immnofluorescence, it was determined that MCNSCs could internalize extracellular aggregates of α-synuclein.[8] MCNSCs were incubated with a medium consisting of Alexa-Fluor-488-labeled α-synuclein. Figure 16 illustrates the internalization of extracellular α-synuclein in mice stem cells.

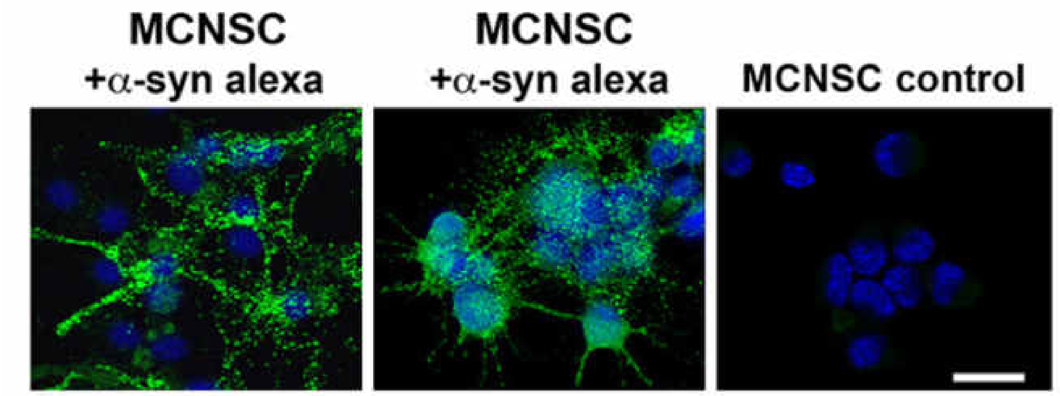

Figure 16. MCNSC uptake of the fluorescent tagged α-synuclein (green) found outside the stem cell.[8]

The transmission of α-synuclein from host cells to grafted MCNSCs were studied in vivo. MCNSCs were labeled with the green fluorescent protein, GFP, and were subsequently placed into transgenic mice brains, which expressed α-synuclein, via stereotaxic intrahippocampal injection. After 1 week, 2.5% MCNSCs had taken up α-synuclein, see Figure 17 A, while after 4 weeks, 15% of MCNSCs had significant levels of α-synuclein. A few of the MCNSCs, 2.5% of total injected stem cells, after 4 weeks displayed Lewy-body like inclusions, see Figure 17 B. For nontransgenic mice that were injected with MCNSCs, no inclusions were found. It was also determined that after 1 week, transgenic mice showed mild inclusions in the MCNSCs and this number grew as time progressed, up to 4 weeks. Compared to mice that had no expression towards α-synuclein, no α-synuclein was found in the MSNSCs, see Figure 17 E. Therefore, it is suggested that without an expression for α-synuclein, the protein will not propagate from neuron to neuron, Figures 17 C and D.[8]

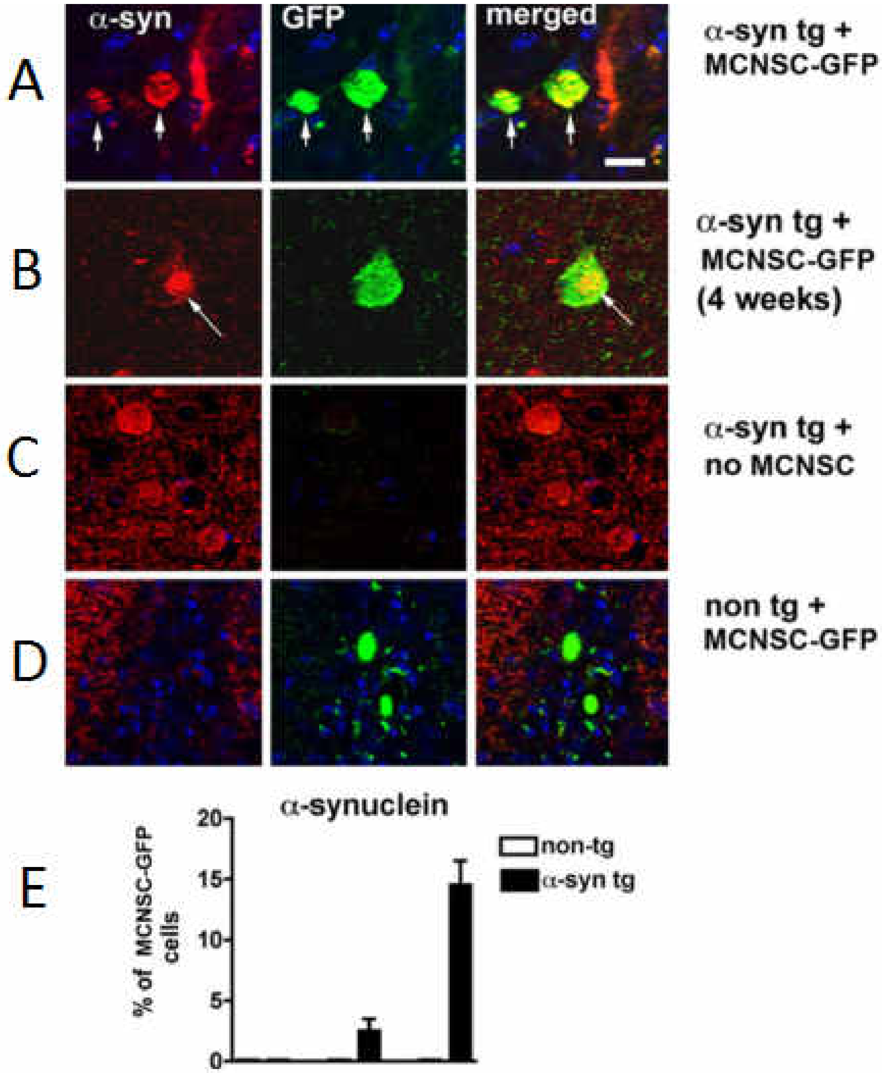

Figure 17. (A) α-synuclein (red) found in transgenic mice were later found in the grafted MCNSCs that were labeled with GFP (green, arrows). (B) After 4 weeks, some MCNSCs displayed an inclusion body that tested positive for α-synuclein. (C) Transgenic mice that had no injection of MCNSCs. (D) Nontransgenic mice that were injected with MSCNSs. No α-synuclein was found in the stem cells. (E) α-synuclein was shown to propagate from the host cells of transgenic mice that had an expression of α-synuclein to MCNSCs. In nontransgenic mice, α-synuclein was not transferred.[8]

Similarly, human dopaminergic neuron cells were cocultured *in vitro* to study the effects of cell-to-cell transmission. One group of cells was expressed with myc-tagged-α-synuclein, i.e. donor cells, while the other group's cells were labeled with Qtracker and had no expression of α-synuclein, i.e. acceptor cells. It was shown that α-synuclein was transmitted from the donor cells to the acceptor cells after 24 hours, Figure 18 A. With this, it was demonstrated that there was a correlation between the expression levels of α-synuclein in the donor cells to that of the acceptor cells that contained the transferred protein, see Figure 18 C, left panel. In some instances, inclusion bodies formed near the nucleus, Figure 18 B, in proportion to the donor's expression levels, Figure 18 C, right.[8]

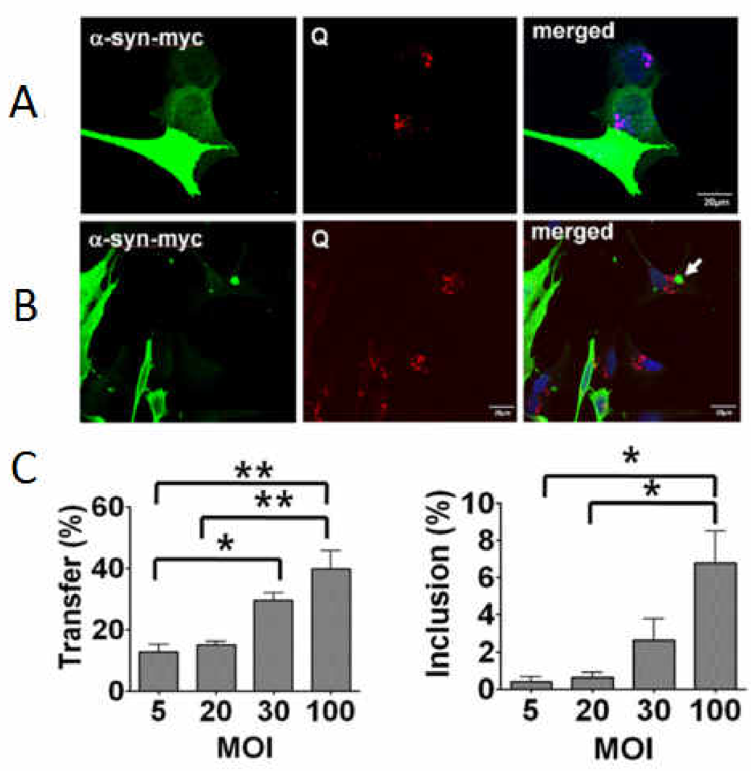

Figure 18. (A) α-synuclein (green) found in the acceptor cells (red) that was transferred from donor cells. (B) Inclusions (arrows) found in acceptor cells. (C) Left, percentage of α-synuclein transferred to the acceptor cells within 3 days. Right, percentage of α-synuclein found in acceptor cells. Error bars correlate to: $*$, $P < 0.05$; $**$, $P < 0.01$.[8]

α-synuclein causing apoptosis in neurons is unknown. Studies of neuron transplantation in humans showed no apparent cell death.[67,74,75] Desplatsa et al. studied the effects of endoyctosed α-synuclein *in vitro* by allowing rat primary cortical neurons, MCNSCs, to exist in the presence of of a medium consisting of either α-synuclein or β-galactosidase (LacZ medium). Figure 19 illustrates their findings. Cells existing in the α-synuclein medium showed neuronal degeneration due to the observed nuclear fragmentation and caspase 3 activation. The longer the time period, the more neuronal cells were killed. In the LacZ medium, the neurons indicated no nuclear fragmentation and there was a negligible increase in caspase 3 activation, Figure 19 A and B. Then, an *in vivo* study was done by injecting MCNSCs into the hippocampus of transgenic mice exhibiting human α-synuclein. During 4 weeks, MCNSCs had an increase in activated caspase 3 immunoreactivity. When tested amongst nontransgenic mice, there was no activation of caspase 3, Figure 19 C. These results were also found to be true for recombinant α-synuclein found outside the cell.[76] However, these results are based on overexpression for α-synuclein.

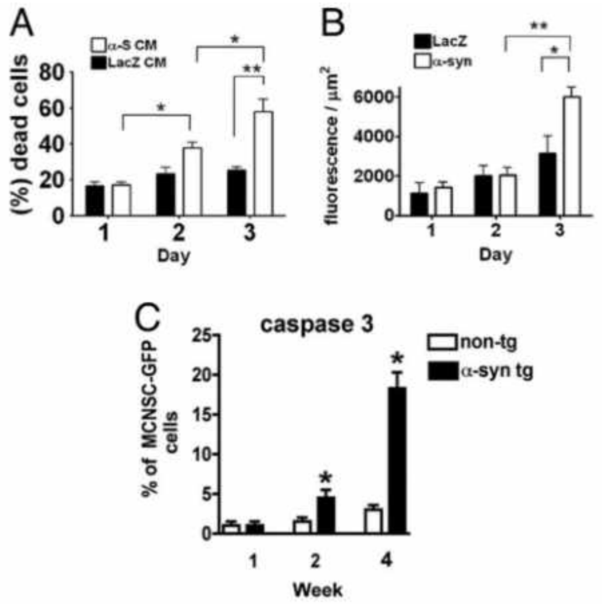

Figure 19. (A and B) Neuronal cell death in two different mediums: SH-SY5Y cells overexpressing either α-synuclein or β-galactosidase (LacZ medium). (A) Nuclear fragmentation observed. (B) Activation of caspase 3 observed through immunofluorescence. Error bars correlate to: $*$, $P < 0.05$; $**$, $P < 0.01$. (C) caspase 3 activation in MCNSCs when injected into either transgenic mice showing an expression for human α-synuclein or nontransgenic mice.[8]

2.2 Recent molecular simulation results

Advancements have been made to understand the molecular mechanisms behind aggregation through *in vitro* studies. However, it has not been until recently that computer simulations have aided in the understanding of the role of different proteins in the aggregation causing neurodegenerative diseases. The reason for not implementing studies using computer simulations sooner was due to the need for lengthy timescales as well as large system sizes.[10] Computer simulations were first used for small peptides but, with a better understanding of protein interactions and system requirements, have grown to simulating many proteins, which help in better understanding the aggregation process. We will discus recent molecular simulations that have aided in a better understanding of neurodegenerative diseases.

It has been suggested the abnormal accumulation of α-synuclein, which is natively unfolded, may contribute significantly to the aggregation found in Lewy bodies. These aggregates are due to a partially folded intermediate, i.e. α-synuclein monomers, that get converted into oligomers and later annular protofibrils and pore-like structures.[77,78] It has been hypothesized that oligomers, rather than fibrils, are the agents leading to neuronal cell death.[59] However, little is known about the mechanism of transforming α-synuclein into oligomers at the early stages of aggregation.

Tsigelny et al. investigated the dynamics of α-synuclein during the beginning of α-synuclein aggregation and the possible role of β-synuclein on the prevention of aggregation using molecular modeling and molecular simulations. They first subjected the two proteins, separately, to a simple system consisting of water in order to study the effects of structural changes to the the different proteins. For the starting structure of α-synuclein, the PDB file, 1xq8, was used as it was predicted that it would more easily result in oligomerization. This file contained the micelle-bound α-synuclein structure obtained through NMR.[79] β-synuclein was created using the homology module of the INSIGHT II program and was then minimized for 10,000 iterations using the DISCOVER program.

α-synuclein contains two regions within the curved N-terminal domain, i.e. helix-N and helix-C. The angle between these two regions at the start was 55 ±3°, after 2.0 ns it decreased to around 42-44°, and then increased after 5.0 ns to 64-70°, see Figure 20 A and B. During the 5.0 ns, the N-terminal region converted from the two curved helical domains into three uncurved helical structures. This resulted when the second curved helix (aa 46-84) transformed into uncurved helix 2 (aa 46-63) and uncurved helix 3 (aa 74-84). These findings demonstrate that α-synuclein developed into a different three-dimensional shape (because of the movement of the C-terminal region compared to that of the N-terminal region) and that the helical structure that α-synuclein assumed was highly stable due to the fact that it never returned to its natively unfolded state.[9]

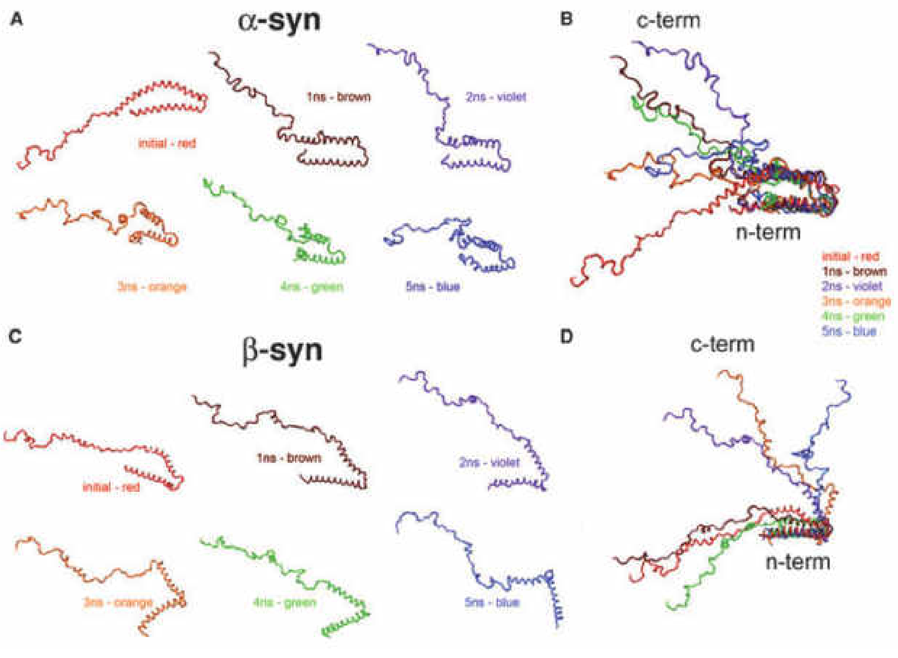

Figure 20. α-synuclein and β-synuclein transfomrations through molecular dynamics. (A) Structural changes of α-synuclein at different times in the simulation. Simulation was done in a simplified system of water. (B) Superimposed images of α-synuclein at aa 1-15.(C) Structural changes of β-synuclein at different times in the simulation. Simulation was done in a simplified system of water. (D) Superimposed images of β-synuclein at aa 1-15.[9]

When comparing α-synuclein to β-synuclein, they found that β-synuclein did not undergo a transformation at the second helix to form the two distinct helices, though sharing a similar structure to that of α-synuclein. Rather, β-synuclein's curved helices converted into a nearly straight configuration after 2.0 ns. The angle of the N-terminal helices varied as well as the motility of the C-terminal tail, noting that β-synuclein's tail provided greater motility than that of α-synuclein's. Finally, the stability of the β-synuclein monomer increased from 2.0 to 3.5 ns.[9]

α-synuclein aggregation was studied through membrane docking. Two initial conformations of the protein were docked on a flat surface without providing limitations. 'Head-to-tail' low energy configurations formed, Figure 21 A and B. These complexes were named due to their interactions, i.e. mainly electric charge, of the amino acids of one α-synuclein's N-terminal domain with the amino acids of the C-terminal domain of the second protein. These homodimers may interact with additional monomers of α-synuclein but this is unlikely resulting in a lack of higher order aggregates. This is because the homodimers restrict the amount of low-energy docking sites needed for successive docking. Because of the lack of propagation towards higher order aggregation, these head-to tail complexes were described as a nonpropagating dimer.[9]

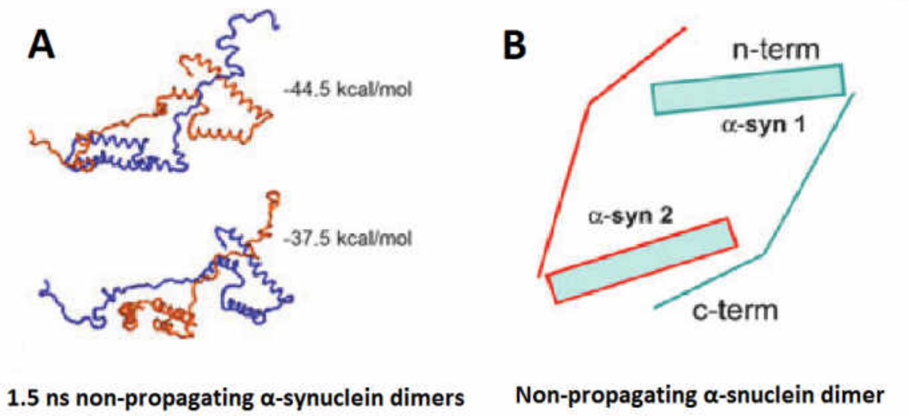

Figure 21. Nonpropagating (head-to-tail) α-synuclein dimers on a flat surface without explicit limitations. (A) Minimal energy of the head-to-tail α-synuclein dimers. (B) α-synuclein monomers are arranged in the head-to-tail configuration which prevents low-energy docking of more α-synuclein.[9]

Additionally, α-synuclein monomers were studied on a membrane surface. The surface used was 1-palmitoyl-2-oleoyl-sn-glycero-3-phosphocholine (POPC) membrane. The protein's surface, i.e. membrane-contacting, was faced towards the membrane. This resulted in α-synuclein's N-terminal helices to be distributed along the membrane as can be seen in Figure 22 A. Figure 22 B illustrates the docking of two α-synuclein monomers onto the POPC membrane.[9]

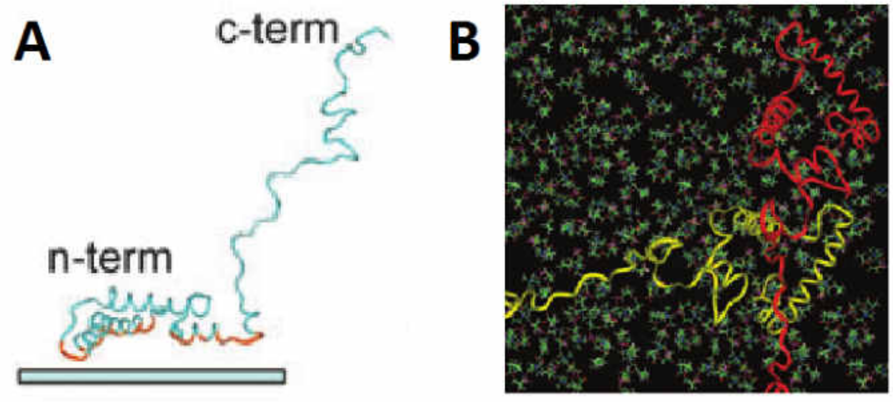

Figure 22. Docking of α-synuclein. (A) Docking of α-synuclein to the membrane's surface at 4.0 ns. Orange depicts the residues in contact with the membrane. (B) Two conformers of α-synuclein at 4.5 ps docked onto the POPC membrane.[9]

Normally, two different complexes would form when docked to the membrane: head-to-tail and head-to-head. Like that for a flat surface, the head-to-tail configurations were not likely to propagate into higher order aggregates since low-energy binding sites were not common. The head-to-head configuration made it possible for additional propagation, i.e., more low energy binding sites, thus known as the propagating dimer. Low-energy binding sites became available, possibly due to an increase in intermolecular interactions. Comparing the conformations that ranged from 1.5 to 5.0 ns, it was observed that for longer simulation times, i.e., greater than 4.0 ns, an increase in residues on the C-terminal tail, which contained mostly the positive charge of the protein, were involved in intermolecular interactions. This, possibly, resulted in the ability to form lower docking energies. Table 1 shows the intermolecular interaction energies involved when dimers of α-synuclein were docked to the POPC membrane at different timer intervals.

Because of the ability to propagate, when similar low energy α-synuclein proteins to that of the propagating dimer were added consecutively, energetically favorable higher order aggregates formed, i.e. trimers, tetramers, pentamers, and hexamers.[9]

Table 1. Electrostatic energies involved in propagating dimers of α-synuclein that were docked onto the POPC membrane. MD, molecular dynamics.[9]

MD time (ns)	Electrostatic energy (kcal$\cdot mol^{-1}$)
1.50	-10.6
2.00	-10.6
2.50	-13.4
3.50	-15.1
4.00	-19.7
4.50	-32.9

When the most likely multimers of α-synuclein were chosen (based off of favorable energies), it was found that six configurations formed at different time periods, see Figure 23.[9] These multimers developed ring-like structures which appeared to be similar to those found using atomic force microscopy.[77]

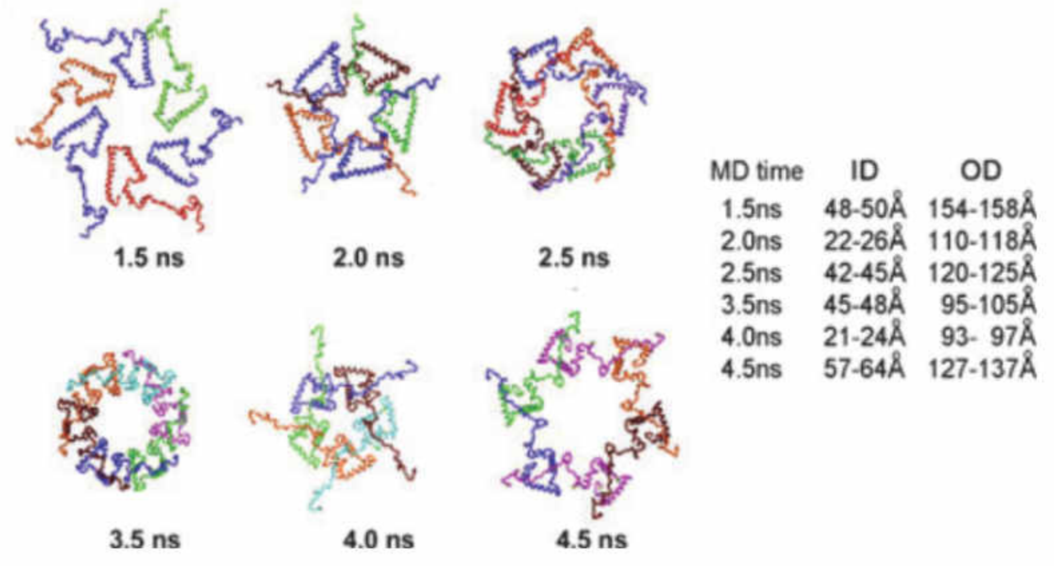

MD time	ID	OD
1.5ns	48-50Å	154-158Å
2.0ns	22-26Å	110-118Å
2.5ns	42-45Å	120-125Å
3.5ns	45-48Å	95-105Å
4.0ns	21-24Å	93- 97Å
4.5ns	57-64Å	127-137Å

Figure 23. Simulations via molecular dynamics of multimers at different time periods. Table on right indicates the inner diameters (ID) and outer diameters (OD).[9]

Because the amyloid diseases, for example, Parkinson's and Alzheimer's diseases, occur due to the slow progression of proteins aggregating to form plaques and tangles, this was studied computationally via molecular dynamic simulations. Simulation of fibrils were done by using the protein model, Protein Intermediate-Resolution Model (PRIME) coupled with discontinuous molecular dynamics (DMD). Polyalanine peptides containing 16 residues in a random-coil state were chosen since they (1) were the simplest peptide recognized to form fibrils undergoing a change from an α-helix structure to a β-sheet structure and (2) contained simple sidechain structures creating simplicity for modeling.[10]

Fibrillization occurred by first forming amorphous aggregates. These aggregates, through time, became rich in β-sheet structure. Finally a nucleus for fibrillization occurred. The fibrillization process can be seen in Figure 24. The simulation consisted of 48 peptides at reduced times, t^*, constant temperature, T^*=0.14, and constant peptide concentration of 10 mM. Small amorphous aggregates form from a random coil state that can be seen at t^*=0. The aggregates grow, t^*=10.0, until they morphed into one large aggregate at t^*=12.0. One aggregate with a β-sheet formed after the large aggregate broke into smaller aggregates at t^*=14.6. This is exemplified as the purple sheet on the lower-right side of the snapshot. The broken aggregates, at t^*=36.1, have become β-sheets, light-blue, white, and dark-blue, while the first β-sheet, purple, has grown. Two of the β-sheets, i.e. light-blue and white, have merged resulting in a two-sheet fibrillar structure at t^*=40.2. This structure grows as the purple and dark-blue sheets join, t^*=49.7. Finally, at t^*=205.9, the final fibrillar structure is stable and continues to grow as more peptides become attached to the ends of the β-sheets.[10] These findings were found to be typical, experimentally, as first proteins join together to form aggregates, than develop a critical nuclei, and finally grow into large fibrils.[80]

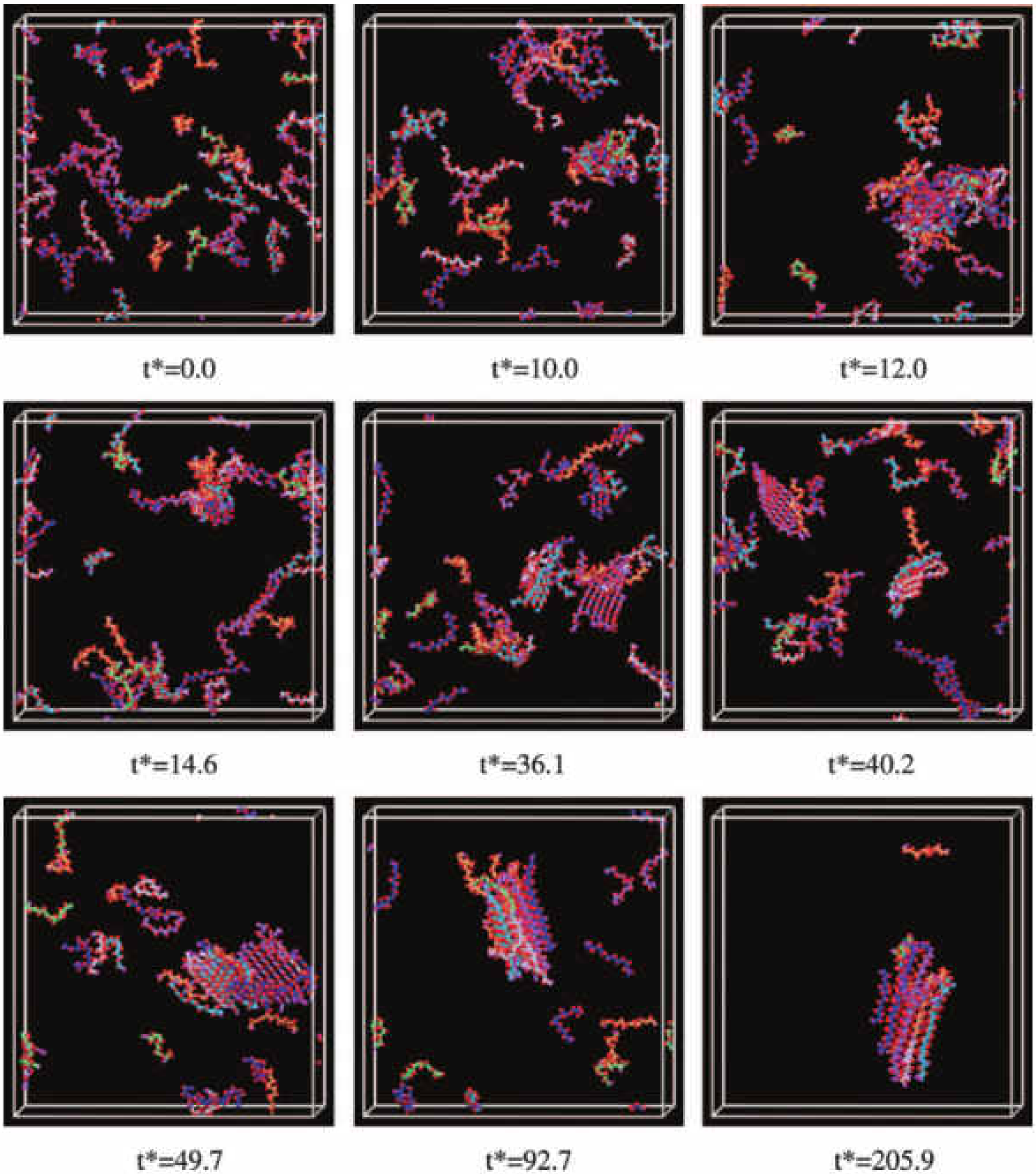

Figure 24. Snapshots of the fibrillization process.[10]

Proteins that are involved in fibril formation, i.e. plaque formation, are small peptides known as amyloid-β (Aβ) with 40 (Aβ_{1-40}) or 42 (Aβ_{1-42}) residues. Proteolytic cleavage, which occurs in Alzheimer's disease, creates smaller fragments which are amyloidogenic and toxic. Studying the kinetics of smaller peptides forming amyloid plaques is much like that for their larger counterpart. By examining the role of these peptides, the overall amyloid formation may be better understood. Nussinov and coworkers studied small amyloid-β peptides with high temperature molecular (MD) simulations in the hopes of understanding the structures that form, particularly multilayer β-sheet oligomer organizations. They studied three different fragments: Aβ_{16-22}, Aβ_{16-35}, Aβ_{10-35} but only Aβ_{16-22} will be looked at here.[11]

Octamers of Aβ_{16-22} were simulated using three parallel (two of which the two layers are parallel, and one of which the two layers are antiparallel) and two antiparallel orientations, Figure 25.[11]

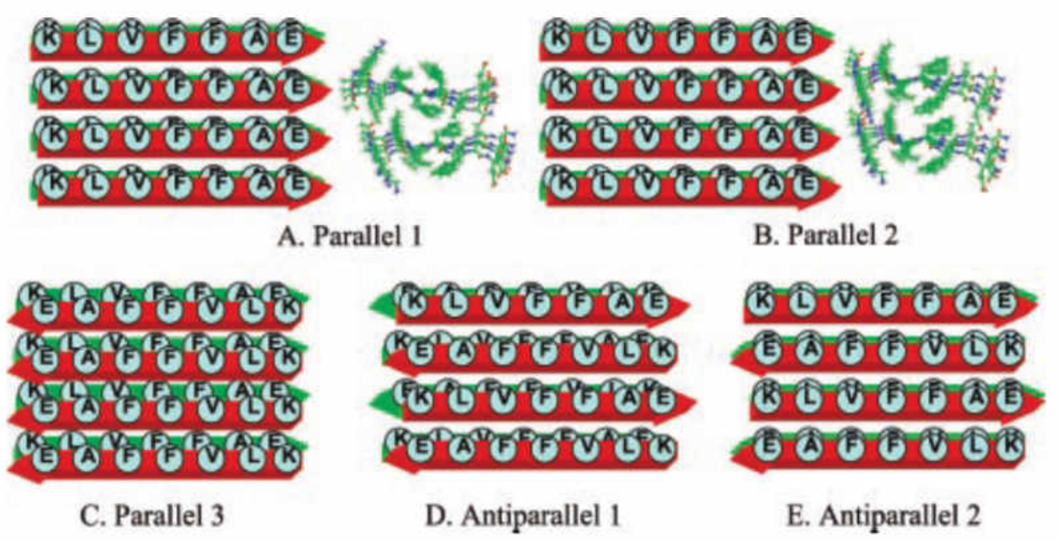

Figure 25. Arrangement of the starting structures simulated for Aβ_{16-35}.[11]

It was determined that Parallel 1 and Parallel 2 dissociated within 1 ns at 330K due to the large rms deviation (rmsd). This was due to weak interactions between the parallel β-sheet layers. This arrangement was therefore considered not to contribute significantly to the formation of amyloid fibrils. However, Parallel 3 was shown to have greater stability than the other two. Two $3-$ns simulations were run. One simulation indicated that the structure remained in a stable β-sheet cluster while the other showed the β-strands separating within the layer. Still, the rmsd of Parallel 3 was substantially lower than those of Parallel 1 and Parallel 2.

The antiparallel arrangements were found to be of a higher stability than all parallel arrangements. Antiparallel 1, which consisted of antiparallel sheets/antiparallel layers, had slight deviations from each other when run in two independent simulations at 330 K. Antiparallel 2, which consisted of antiparallel sheet/parallel layers, had insignificant deviations from each other. This arrangement was also shown to be the most stable of all the configurations. The stability could come from salt bridges but more than likely it was due to hydrophobic interactions. Therefore, for Aβ_{16-22}, both parallel and antiparallel β-sheet configurations could occur but the antiparallel β-sheet orientation was the most common and the most stable.[11] This was in agreement to previous solid state NMR data.[81]

The simulations provided by Nussinov and coworkers are helpful in that they provide the stabilities of certain Aβ arrangements, but this does not reveal the aggregation process for these peptides. Santini et al. investigated this phenomenon with three Aβ_{16-22} peptides via the activation-relaxation technique (ART) and a generic energy model, OEP. In randomly selected Studies of neuron transplantation in humans showed no apparent cell death states, the most stable structure, i.e. antiparallel orientation, was found to superimpose within 1 $\mathring{A}$ rmsd of its arrangement when found in fibrils. The complete structural order of the peptides within the fibrils needed larger aggregates since the structure was in equilibrium with antiparallel β-sheets and mixed parallel-antiparallel β-sheets. Finally, folding occurred when dimers formed with the consecutive addition of monomers. Folding continued through a common mechanism between disordered and native alignments of β-strands.[82]

CHAPTER III

MOLECULAR DYNAMICS

3.1 Gromacs

GROMACS, GROningen MAchine for Chemical Simulations, is a computer software package aimed to run molecular dynamics mainly on biomolecules such as proteins, lipids, and nucleic acids. It was designed at the University of Groningen and is now maintained by many universities worldwide.

GROMACS has many advantages that make computer simulations for α-synuclein simple compared to other methods. This package is free and open source allowing for anyone to be able to use it since it is also user-friendly. For example, topologies and run parameters are written in a clear text format and error messages are given if something is inaccurate. Also, it has a graphical user interface and the option -h can be used if help is needed about different tools. It runs on both CPUs (Central Processor Unit) and GPU (Graphics Processing Unit). GROMACS has an exceptional high performance compared to other software packages since the code is optimized. It can also be run in parallel by using the standard MPI communication. GROMACS also contains different force fields and many different trajectory analysis resulting in not having to write codes[83]

3.2 Molecular Dynamics

Molecular Dynamics (MD) simulations have become a powerful computational tool because it can simulate a large variety of systems. MD is performed in much of the same way as real world experiments. For example, a sample must be prepared and a tool must be used to measure a property. If there is statistical noise, the longer the average measurement, the more accurate the results. In our case, we prepared our system: alpha-synuclein, water molecules, and ions. Solving Newton's equations of motion until the properties of the system no longer change over time equilibrates the system.[84] Newton's equations of motion for a system can be described by equation 3.1.[13]

$$\mathbf{F}_i = m_i \cdot a_i = m_i \cdot \frac{dv_i}{dt} = m \cdot \frac{\partial^2 \mathbf{r}_i}{\partial t^2}, i = 1...N \tag{3.1}$$

where N is the number of interacting particles, m is the mass of atom i, r is the position of atom i as a function of time, and t is time. The force on atom i can is described by equation 3.2

$$\mathbf{F}_i = -\frac{\partial V}{\partial \mathbf{r}_i} \tag{3.2}$$

where force is the negative derivative of a potential function.[13] After this equilibration, where temperature and pressure remain at the set values, results can be obtained.

Molecular Dynamics can be illustrated by the following flow chart, see Figure 26.

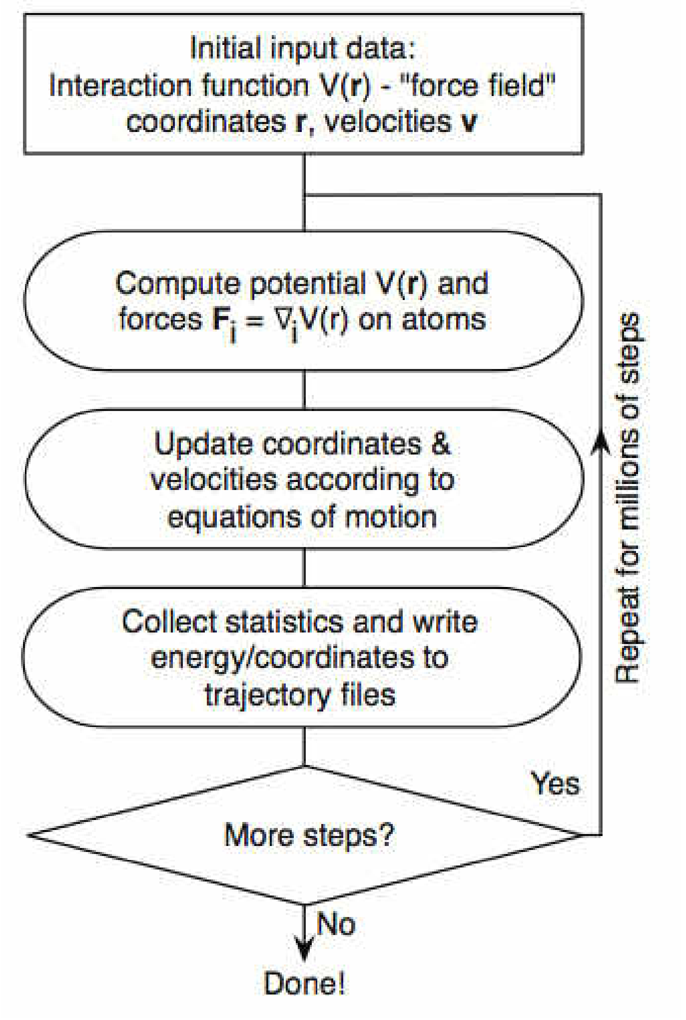

Figure 26. Simplified flowchart of Molecular Dynamics. Note, force should be the negative gradient of the potential.[12]

MD is first started by (1) inputting initial conditions. This includes the potential interaction V, positions r, and velocity v, of all atoms in the system. Next, (2) forces are computed. Forces on any atom (see equation 3.2) are calculated by: determining both the force on any non-bonded pairs, forces due to bonded interactions, restraining forces, and external forces. The force on any non-bonded pair can be described by equation 3.3

$$\mathbf{F}_i = \sum_j \mathbf{F}_{ij} \tag{3.3}$$

Potential energy, kinetic energy, and pressure tensor are also calculated at this point. Then (3) the configuration is updated by solving for Newton's equations of motion (see equation 3.1). Finally, (4) the output is written. For example, this could include positions, velocities, energies, temperature, and pressure. This procedure is done iteratively until the required number of steps is met.[13]

3.2.1 Integrators

Integrators have been created in order to integrate Newton's equations of motion. There have been many different algorithms to do this but the most common is the Verlet integrator, which is usually the simplest and the best. However, we used the leap-frog integrator for studying α-synuclein in water, which is equivalent to the Verlet integrator. The Leap Frog algorithm calculates the velocities v at half-integer time steps $t - \frac{1}{2}\Delta t$ to evaluate the new positions r. The velocities at half-integer time steps are defined by equations 3.4 and 3.5.

$$v(t - \frac{\Delta t}{2}) \equiv \frac{r(t) - r(t - \Delta t)}{\Delta t} \tag{3.4}$$

$$v(t + \frac{\Delta t}{2}) \equiv \frac{r(t + \Delta t) - r(t)}{\Delta t} \tag{3.5}$$

Based on the old positions and velocities, we attain equation 3.6 for the new positions based on equation 3.5

$$r(t + \Delta t) = r(t) + \Delta t v(t + \frac{\Delta t}{2}) \tag{3.6}$$

In order to update the velocities, the Verlet algorithm is utilized giving equation 3.7. Therefore, by using the forces $f(t)$ determined at the new positions, the positions and velocities are updated.

$$v(t + \frac{\Delta t}{2}) = v(t - \frac{\Delta t}{2}) + \Delta t \frac{f(t)}{m} \tag{3.7}$$

The Leap Frog algorithm, because of being derived from the Verlet algorithm, will produce identical trajectories, see equation 3.8. However, the velocities are not determined at the same time as the positions. Due to this, the total energy cannot be calculated because both the kinetic and potential energy are not determined at the same time.[13,84]

$$r(t + \Delta t) = 2r(t) - r(t - \Delta t) + \frac{1}{m} f(t) \Delta t^2 + O(\Delta t^4) \tag{3.8}$$

The trajectory of the Leap Frog algorithm can be seen in Figure 27 where the positions and velocities are jumping over each other, much like how frogs leap over each other's backs.[13]

For studying carbon nanotubes, symplectic integrators developed by Martyna et al. were used [56, 57].

3.2.2 Velocity Generation

Velocity generation is used to assign velocities to different particles. This is done by utilizing the Maxwell distribution at the given temperature. A simple

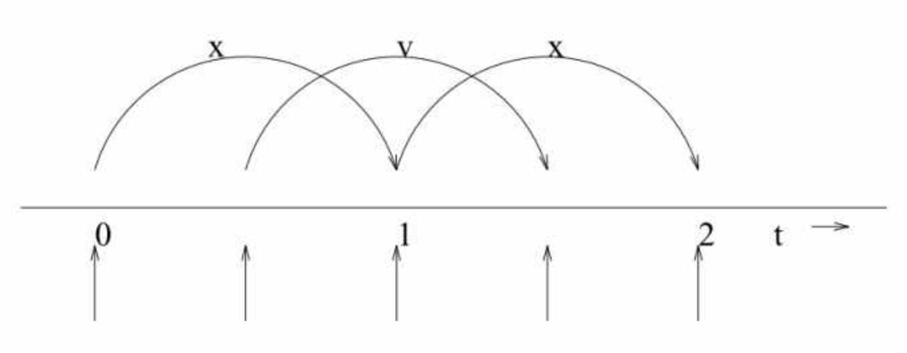

Figure 27. Leap-frog integrator.[13]

illustration of Maxwell's distribution can be seen in Figure 28. As the temperature increases, the distribution is shifted to higher velocities and is broadened at higher temperatures. A random seed (*gen_seed*) is also used to give random velocities by using a random generator.[13]

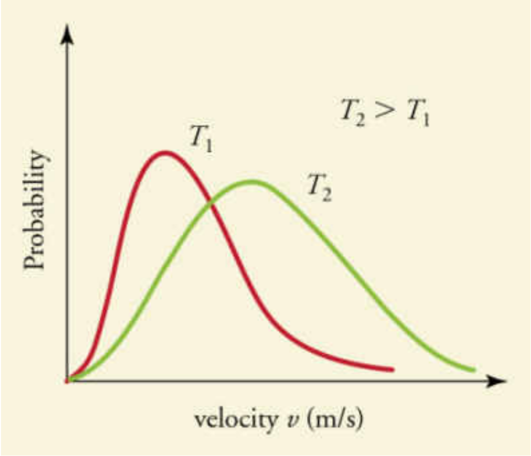

Figure 28. Maxwell distribution.[14]

3.2.3 Energy Minimization

Energy minimization is used to find a potential energy minimum near the starting structure. This is done to ensure no steric clashes or inappropriate geometries and to "relax" the system. If this is not done, the simulation could crash. Within GROMACS, three different methods may be used: steepest descent, conjugate gradients, or l-bfgs (limited-memory Broyden-Fletcher-Goldfarb-Shanno quasi-Newtonian minimizer). We chose the steepest descent as the algorithm as it is robust and brings the protein to the nearest local minimum very quickly; however, the conjugate gradient algorithm is slower but brings the protein very near to the minimum energy.

The steepest descent algorithm works by first calculating both forces and potential energy. Next, a maximum displacement, h_n, is applied and new positions of the force and potential energy are found. This is described in equation 3.9

$$\mathbf{r}_{n+1} = \mathbf{r}_n + \frac{\mathbf{F}_n}{max(|\mathbf{F}_n|)} h_n \tag{3.9}$$

where vector $\mathbf{r}$ is the vector used to define the 3N coordinates and $\mathbf{F}_n$ is the force, i.e. negative gradient of the potential. This process is repeated over and over again as long as the move is accepted. New positions occur when $\mathrm{V}_{n+1} < \mathrm{V}_n$ which results in $\mathrm{h}_{n+1} = 1.2\mathrm{h}_n$. Rejected positions occur when $\mathrm{V}_{n+1} \geq \mathrm{V}_n$ which results in $\mathrm{h}_n = 0.2\mathrm{h}_n$.

The minimization of energy stops when either the simulation has reached the number of force evaluations specified or the absolute value of the force term is smaller than a specified value ϵ. ϵ may be described through the root mean square force f that a harmonic oscillator would exhibit at temperature T, equation 3.10,

$$f = 2\pi \upsilon \sqrt{2mkT} \tag{3.10}$$

where υ is the oscillator frequency, m is the reduced mass, and k is the Boltzmann constant.[?]

Energy minimization was ran using the GROMACS MD engine, mdrun.

3.2.4 Equilibration

Equilibration is used to obtain a state of equilibrium between the ions, solvent, i.e. water, and α-synuclein. If this was not done, the system could potentially collapse. Therefore, the solvent and ions are placed around the protein based on the temperature. Here we wished to study the protein at four different temperatures: 293K, 310K, 323K, and 348K; where 310K is the average human body temperature. We conducted this first phase in the NVT ensemble, also known as the isothermal-isochoric or canonical. Once the solvent reached equilibrium with the protein at the different temperatures, pressure was applied in order to obtain proper density. This second phase was conducted in the NPT ensemble, also known as isothermal-isobaric. Like the energy minimization step, equilibration was run using mdrun.

3.2.5 Periodic Boundary Conditions

Because we are simulating a system that is relatively small, there is a lot of unwanted boundary with its environment, i.e. vacuum. Our goal is to simulate a large system of water and α-synuclein. In order to circumvent this problem, we used periodic boundary conditions.

Periodic boundary conditions are able to create no boundaries between the system and surroundings by first creating the system within a box. This box is then duplicated many times and the system is surrounded by these many boxes. A scheme of periodic boundary conditions in two-dimensions can be seen in Figure 29. We used periodic boundary conditions in all directions.

GROMACS combines periodic boundary conditions with the minimum image convention. This is when short-range non-bonded interaction terms are applied to the closest image of one particle. This method is not accurate for long-range electrostatics so lattice sum methods such as Ewald Sum, PME, and PPPM are applied.

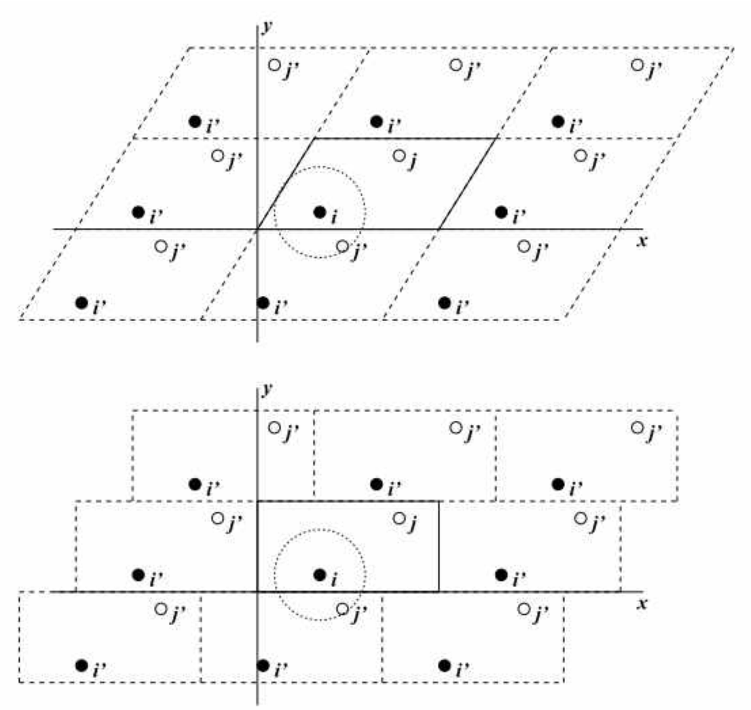

Figure 29. Periodic boundary conditions.[?]

We used a unit cell as our system. This box is defined by the box vectors **a**, **b** and **c**. In order for GROMACS to be able to use these vectors, they must satisfy the following criteria:[?]

$$a_y = a_z = b_z = 0 \tag{3.11}$$

$$a_x > 0,\ b_y > 0,\ c_z > 0 \tag{3.12}$$

$$|b_x| \leq \frac{1}{2}a_x,\ |c_x| \leq \frac{1}{2}a_x,\ |c_y| \leq \frac{1}{2}b_y(3.13)$$

3.2.6 Neighbor Searching

Because calculating the energy of the system is expensive timewise, determining what particles do not contribute to the energy of a single particle is important. This is known as neighbor searching.

Non-bonded pair forces are calculated for pairs, i, j, as long as the distance r_{ij} between them is less than a the radius criteria, R_c. The only case in which non-bonded forces are calculated even if it is less than R_c is when the force is a fully bonded interaction. GROMACS keeps track of the non-bonded interactions for all of these particles by using a *pairlist*. This list contains atoms i, displacement vectors of these atoms, as well as all the particles j within the radius of atom i.

In order to create this neighbor list, i.e., all particles within the cut-off criteria, neighbor searching must be utilized. Neighbor searching uses periodic boundary conditions which allows for the use of a grid search. Figure 30 shows a grid search in two dimensions.[13]

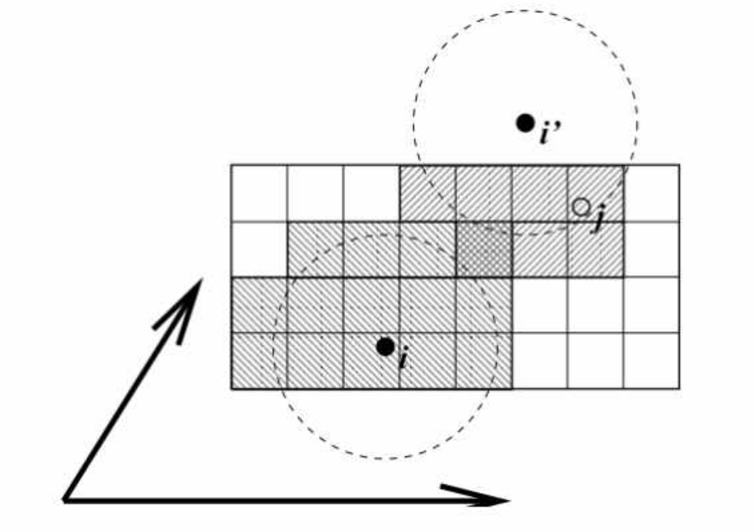

Figure 30. Grid search.[13]

3.2.7 Output Control

The output control gives commands on when to update certain files. There are five commands: nstxout, nstvout, nstxtcout, nstenergy, and nstlog. nstxout gives the frequency on when to write coordinates to the output trajectory file. nstvout writes velocities to the output trajectory file. nstxtcout writes coordinate to the xtc trajectory file. nstenergy writes energies to the energy file. Finally, nstlog writes energy to the log file. In all cases except nstxtcout, the last parameters are always written.[13] Updating files occurred every 1000 steps.

3.2.8 Temperature Coupling

Because we intended to simulate a system that contained a constant temperature, i.e., 293 K, 310 K, 323 K, and 348 K, we used a constant temperature ensemble, NVT. A thermostat was needed to ensure proper sampling of this canonical ensemble at constant temperature. Temperature, which reflects the average energy, i.e., kinetic energy, of the system, is calculated through the equipartition function. Therefore, a thermostat is needed to guarantee that the average temperature is correct.

There are different thermostats to choose from within GROMACS. These include weak coupling scheme of Berendsen, extended ensemble Nos$\acute{e}$-Hoover scheme or the velocity rescaling scheme. We chose the velocity rescaling scheme, also known as V-rescale, for studying α-synuclein in water and the Nos$\acute{e}$-Hoover scheme for studying carbon nanotubes. Both will be discussed.

The velocity rescaling scheme is a modification of the Berendsen so this thermostat will first be described. Berendsen temperature coupling mimics that of first-order kinetics of an outside heat source with a temperature of T_o. The difference in temperature of the system to the external heat source is slowly corrected through equation 3.14.

$$\frac{dT}{dt} = \frac{T_o - T}{\tau} \tag{3.14}$$

From equation 3.14, the temperature difference decays exponentially with a time constant τ. The strength of the coupling can be varied depending upon the work needed. For equilibration, the coupling time can be short, i.e. 0.01 ps. However, for reliable equilibrium simulations, the time may be much longer, i.e. 0.5 ps.

The disadvantage of using the Berendsen thermostat is that it suppresses the fluctuations of the kinetic energy, and, therefore, will not produce an accurate canonical ensemble. However, a thermostat that does produce an accurate NVT ensemble is the velocity rescaling thermostat.

The velocity rescaling thermostat uses an additional stochastic term that creates an accurate kinetic energy distribution, see equation 3.15, thus producing a correct NVT ensemble.

$$dK = (K_o - K)\frac{dt}{\tau_T} + 2\sqrt{\frac{KK_o}{N_f}}\frac{dW}{\sqrt{\tau_T}} \tag{3.15}$$

Here K is the kinetic energy, N_f is the number of degrees of freedom, and dW is a Wiener process. The other excellent feature of the velocity rescaling thermostat is that it takes advantage of the Berensen thermostat in that it is a first order decay of temperature and there are no oscillations involved.[85]

The Nos*é*-Hoover scheme (used for carbon nanotubes)

3.2.9 Pressure Coupling

Just as temperature is able to be coupled, pressure may be coupled to the system. There are different types of algorithms that can be used such as the Berendsen algorithm, extended ensemble Parrinello-Rahman, and the

Martyna-Tuckerman-Tobias-Klein (MTTK). We chose the Parrinello-Rahman algorithm, which can be easily combined with other temperature coupling algorithms.

During the NVT equilibration, pressure coupling was turned off. However, during the NPT equilibration, pressure coupling was turned on in order to equilibrate pressure using the Parrinello-Rahman approach.

The Parrinello-Rahman pressure coupling will provide constant pressure simulations, and, in theory, give an accurate NPT ensemble. This barostat obeys the matrix equation of motion in equation 3.16

$$\frac{d\mathbf{b^2}}{dt^2} = V\mathbf{W^{-1}}\mathbf{b}^{'\mathbf{-1}}(\mathbf{P} - \mathbf{P}_{ref}) \tag{3.16}$$

where the box vectors are represented by the matrix $\mathbf{b}$, V is the volume of the box, $\mathbf{W}$ is the matrix parameter that controls the strength of the coupling, and $\mathbf{P}$ and $\mathbf{P}_{ref}$ are the current and reference pressures, respectively.

For the particles, the equations of motion are altered. Under normal circumstances, both the Nos*é*-Hoover thermostat and the Parrinello-Rahman barostat are applied. For simplistic purposes, the Parrinello-Rahman modification is shown in equations 3.17 and 3.18.

$$\frac{d^2\mathbf{r}_i}{dt^2} = \frac{\mathbf{F}_i}{m_i} - \mathbf{M}\frac{d\mathbf{r}_i}{dt} \tag{3.17}$$

$$\mathbf{M} = \mathbf{b}^{-1}\left[\mathbf{b}^{-1}\frac{d\mathbf{b}'}{dt} + \frac{d\mathbf{b}}{dt}\mathbf{b}'\right]\mathbf{b}'^{-1} \tag{3.18}$$

The inverse mass parameter matrix $\mathbf{W}^{-1}$ figures two things: the strength of the coupling and how the box can be deformed. It is defined by equation 3.19

$$\left(\mathbf{W}^{-1}\right)_{ij} = \frac{4\pi^2\beta_{ij}}{3\tau_p^2 L} \tag{3.19}$$

where β is the isothermal compressibility, τ_p is the pressure time constant, and L is the largest box matrix element.[86,87]

3.3 Important properties

3.3.1 Root Mean Square Deviation

Root mean square deviation (RMSD) was calculated using the program *g_rms*. This program compares the final structure after molecular dynamics to that of a reference structure using least-square fitting. Calculating the RMSD is shown in equation 3.20

$$RMSD\left(t_1, t_2\right) = \left[\frac{1}{M}\sum_{i=1}^{N} m_i \left\|\mathbf{r}_i(t_1) - \mathbf{r}_i(t_2)\right\|^2\right]^{1/2} \tag{3.20}$$

where $M = \sum_{i=1}^{N} m_i$ and $\mathbf{r}_i(t)$ is the position of atom i at position t.[13]

RMSD can be calculated based on a number of different regions. For example, evaluating RMSD could include comparing the main chain, the protein plus hydrogen atoms, side chains, Cα of the backbone, as well as other regions to the reference structure and the final structure.[13]

3.3.2 Radius of Gyration

The radius of gyration measures the compactness of the protein, for example, how folded or unfolded it is. GROMACS uses the program *g_gyrate* to calculate this by evaluating he root mean square distance between its center of gravity and its ends. More specifically, *g_gyrate* calculates the radius of gyration based off of a group of atoms, which are mass weighted, and the radii of gyration about the x, y, and z axes, as a function of time. α-synuclein was fitted along the backbone atoms, i.e. N, Cα, and C. The equation used to obtain the radius of gyration is seen in equation 3.21

$$R_g = \left(\frac{\sum_i \|\mathbf{r}_i\|^2 m_i}{\sum_i m_i} \right)^{1/2} \tag{3.21}$$

where mi is the mass of atom i and $\mathbf{r}_i$ is the position of atom i with respect to the center of mass of the molecule.[13]

3.3.3 Density

Density can be calculated using the program *g_density*. This program calculates the partial density across the box by considering the masses. This tool becomes practical when considering the distribution of atoms or groups along the interface. To determine the density for the entire isothermal- isobaric, i.e. NPT, ensemble, the program *g_energy* should be used.[13]

3.3.4 Energies

The program *g_energy* is useful for the verification of some or all energies as well as different properties, i.e. total pressure, pressure tensor, density, box-volume and box-sizes, by extracting either energy components or distance restraint data from an energy file. The result allows the user to choose from a list of set energies such as potential, kinetic or total energy, or specific contributions such as Lennard-Jones or dihedral energies.[13]

CHAPTER IV

MODELING α-SYNUCLEIN IN AQUEOUS SOLUTIONS

4.1 Force fields

A force field represents the parameters of a potential that are used to calculate forces in molecular dynamics simulations. The goal in the creation of a force field is to be able to describe interactions between particles, mainly atoms.

4.1.1 Model for alpha-synuclein

The force field applied to one protein of alpha-synuclein to a system of water was the optimized potential for liquid simulations, all atom model (OPLS-AA). This force field is based on liquid-state simulations[88] and has been shown to correctly compute liquid state thermodynamic properties.[89]

Most force fields divide potential functions into two categories: bonded and nonbonded interactions. Bonded interactions include covalent bond-stretching, angle-bending and torsion potentials. Nonbonded interactions include Lennard-Jones repulsion and dispersion as well as electrostatics.[12] For the OPLS-AA, the nonbonded parameters, i.e., charge–charge and van der Waals terms, were calculated from liquid state calculations. However, bonded parameters, i.e., stretching, bending, and torsional terms, were fitted using quantum chemical calculations.[88]

The total energy of the system is calculated as the sum of the nonbonded energy, bond stretching and angle bending terms, and torsional energy, see equation 4.1.

$$E_{total} = E_{nonbonded} + E_{bond} + E_{angle} + E_{torsion} \tag{4.1}$$

We will first look at the bonded interactions and then the nonbonded parameters.

Like mentioned previously, bonded parameters consist of bond-stretching, angle-bending, and torsion potentials. Both bond-stretching and angle-bending are depicted in Figure 31.

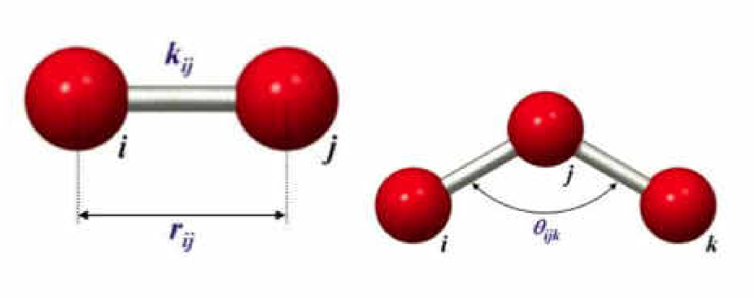

Figure 31. Bond stretching and angle bending between atoms i, j, and k.[15]

Bond stretching is defined by harmonic potentials. Harmonic potentials are both strong and fluctuate little around their equilibrium values, see Figure 32 below. The potential can be described through a parabolic equation, equation 4.2.

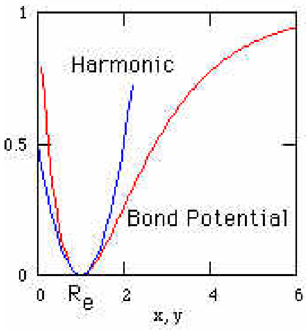

Figure 32. Harmonic Potential. Shows a deep well around the equilibrium bond length.[16]

$$V = \frac{1}{2}k(R - R_{eq})^2 \tag{4.2}$$

where k is the force constant, R is the bond length and subscript eq refers to equilibrium values. The bond equilibrium values are found through x-ray data while force constants are derived by fitting to experimental vibrational frequency data.[15] Below, equations 4.3 and 4.4 are the equations used to obtain bond stretching and angle bending energies.

$$E_{bond} = \sum_{bonds} K_r (r - r_{eq})^2 \tag{4.3}$$

$$E_{angle} = \sum_{angle} K_\Theta (\theta - \theta_{eq})^2 \tag{4.4}$$

where r is bond length, θ is bond angle, and K encompasses the force constant.

The torsional term is described in equation 4.5 and is summed over all of the dihedral angle, i.

$$E_{torsion} = \sum_i \frac{V_i^1}{2}\left[1 + cos(\phi_i)\right] + \frac{V_2^i}{2}\left[1 - cos(2\phi_i)\right] + \frac{V_3^i}{2}\left[1 + cos(3\phi_i)\right] \tag{4.5}$$

A dihedral angles is shown in Figure 33.

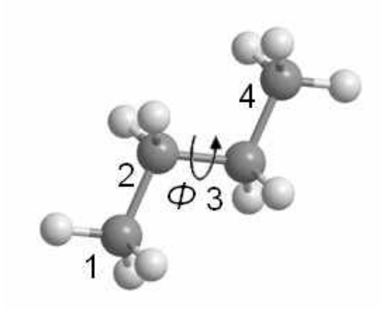

Figure 33. Dihedral angle. Defined by three bond vectors.[17]

The dihedral potential, V, is represented by a cosine expansion. Because the dihedrals are free rotating, the angle may have any value within 360° but this depends on the barrier between low energy conformations.[90]

The nonbonded energy was calculated as the sum of the Coulomb and Lennard-Jones contributions for pairwise intra- and intermolecular interactions[88] as shown in equation 4.6.

$$E_{nonbonded} = \sum_{i<j} \left[\frac{q_i q_j e^2}{r_{ij}} + 4\epsilon_{ij} \left(\frac{\sigma_{ij}^{12}}{r_{ij}^{12}} + \frac{\sigma_{ij}^{6}}{r_{ij}^{6}} \right) \right] f_{ij} \tag{4.6}$$

Coulomb's law, first part of equation 4.6, describes the electrostatic interaction between two point charges, i.e., atoms i and j.[91] This can be seen in the first part of the above equation where e is known as the Coulomb's constant, electric force constant, or electrostatic constant and r_{ij} is the distance separating the two point charges. The Coulomb's constant was derived by Maxwell using the speed of light, magnetic permeability and electric permittivity. The attractive and repulsive forces are also described by Coulomb's law because if both point charges are the same, there is repulsion. If both, however, have opposite charges, they are attracted towards each other.

The Lennard-Jones potential takes into account the van der Waals forces because of dipole-dipole interactions as well as Pauli repulsion due to repulsive forces.[15] An example of a Lennard-Jones potential can be seen in Figure 34. As a molecule moves closer to another molecule, their electrons and nuclei interact with each other causing a potential energy of interaction. The potential increases dramatically as two particles move closer than their equilibrium bond length and, thus, repulsion occurs. The potential decreases as two particles move farther away from their equilibrium bond length and, thus, attraction occurs.[18]

The Lennard-Jones potential term can be seen in the second part of equation 4.6. Here, ϵ_{ij} is the depth of the potential well, σ_{ij} is the distance between atoms i

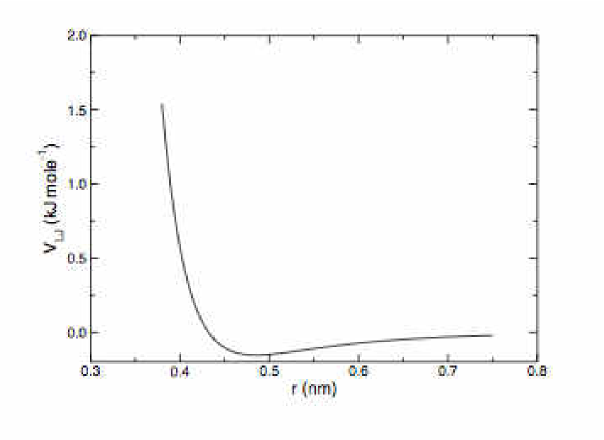

Figure 34. Lennard-Jones Potential.[18]

and j where the inter-particle potential is zero, r_{ij} is the distance between atoms i and j, and f_{ij} is a scaling factor.[88] This "6–12" potential has both an attractive, sixth-power, and repulsive, twelfth-power, term. The scaling factor is used to limit computational time as it would not need to consider every bonded interaction, i.e. energy would be zero. f_{ij} is 0 when atoms i and j are either connected by one or two valence bonds, i.e. 1–2 or 1–3 pairs. f_{ij} is 0.5 when the atoms are connected through three bonds, i.e. 1, 4 interactions, and 1.0 for all other interactions.

Combination rules for the parameters, σ_{ij} and ϵ_{ij}, are used to help describe the interaction energy between two different non-bonded atoms, i.e. i and j. There are many different types of combination rules and knowing which one to use is based on the force field being utilized. The geometrical average works best with the chosen force field, optimized potential for liquid simulations, all atom model.[88] The geometrical average is given by equations 4.7 and 4.8

$$\sigma_{ij} = (\sigma_{ii}\sigma_{jj})^{\frac{1}{2}} \tag{4.7}$$

$$\epsilon_{ij} = (\epsilon_{ii}\epsilon_{jj})^{\frac{1}{2}} \tag{4.8}$$

4.1.2 Water Model

There are many different solvent models to choose from. In our simulations, we used water as the solvent. The water models are classified by the amount of points used to describe the model (which can range from 2-site to 6-site models), the flexibility of the molecule, as well as the polarization effects. For water models, the most common are SPC, SPC/E, TIP3P, and TIP4P. For our solvent, we chose the three-site model, SPC/E (Simple Point Charge Extended model), which is a modification of SPC. This provides a better density and diffusion constant than the SPC model. The result is that the SPC/E model provides simplicity and computational efficiency for molecular dynamics. SPC/E is a three-site model, which is characterized as having three interaction sites, correlating to three atoms (two hydrogens and one oxygen). A point charge is appointed to each atom, plus oxygen receives the Lennard-Jones parameters. The SPC/E assigns a rigid geometry, i.e planar, instead of assuming an ideal tetrahedral shape. Figure 35 shows a water molecule as defined by the SPC/E model. Table 2 lists the different parameters used for the SPC/E water model where σ is the Lennard-Jones parameter for oxygen, and q_1 and q_2 are the charges of hydrogen and oxygen respectively.[23]

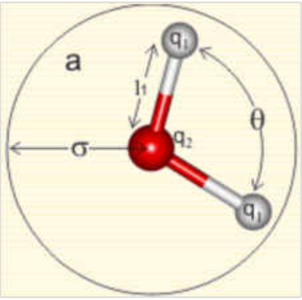

Figure 35. Simple Point Charge Extended (SPC/E) Model.[19]

Table 2. Parameters of the SPC/E water model.[23]

Parameters	SPC/E
$\sigma(\mathring{A})$	3.166
$\epsilon(kJmol^{-1}$	0.650
$l_1(\mathring{A})$	1.000
$q_1(e)$	+0.4238
$q_2(e)$	-0.8476
$\theta°$	109.47

4.2 Set-up

4.2.1 Energy minimization

Four simulations were ran at different temperatures: 293 K, 310 K, 323 K, 348 K. The energy of the entire system was minimized using the command, *mdrun*, see Figure 36 below. The potential energy reached an adequate plateau of -1.025x10$^{9}kJmol^{-1}$ to ensure no steric clashes or inappropriate geometries.

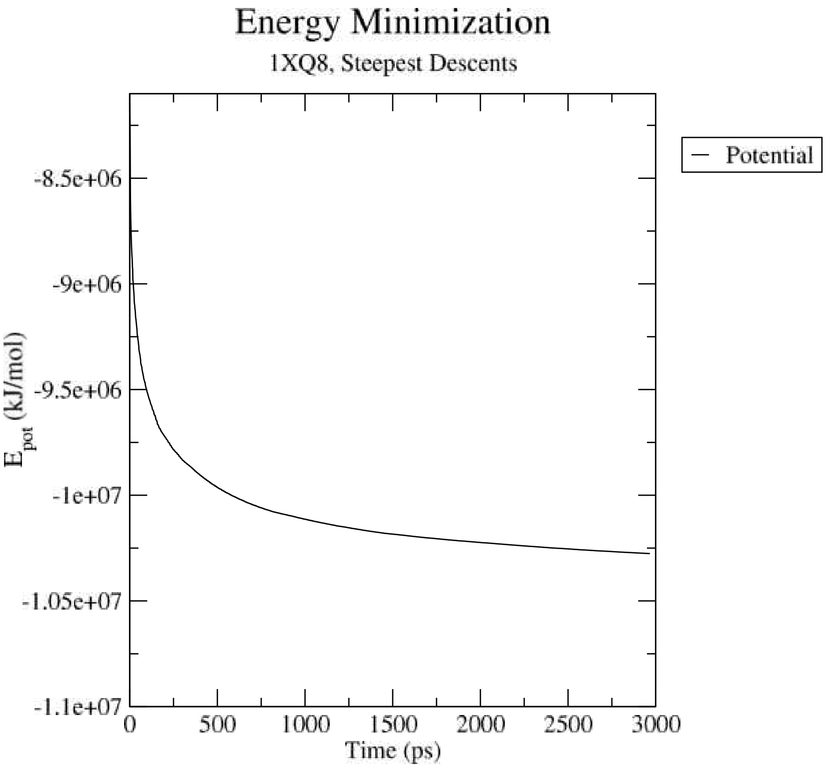

Figure 36. Energy Minimization

The energy minimized system can be seen in Figure 37.

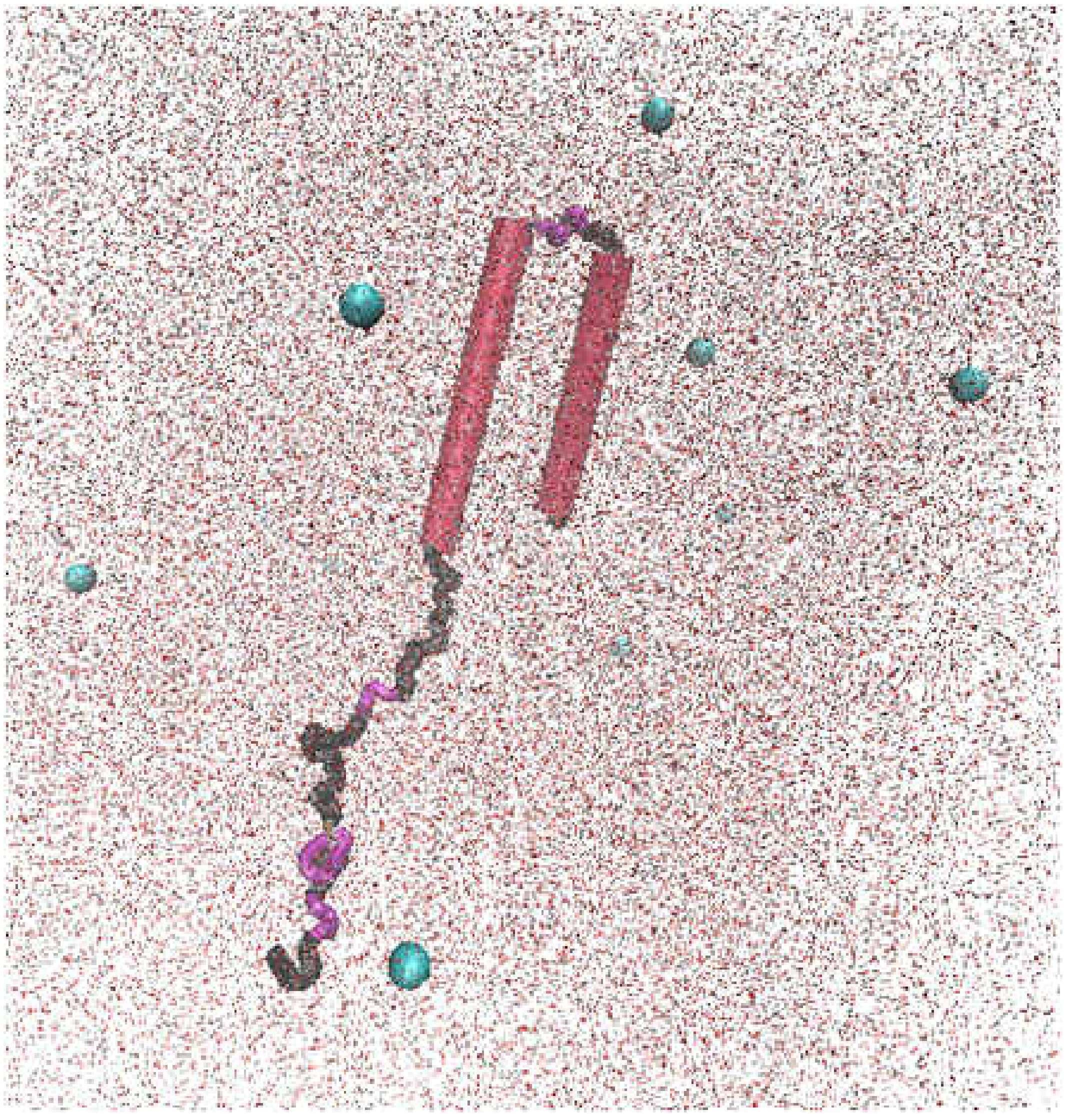

Figure 37. Energy minimization of the aqueous system where the tubes are the alpha-helices, black regions are the coils, and violet regions are the turns. Blue spheres are represented as sodium ions.

4.2.2 NVT Equilibration

The systems were equilibrated to the set temperatures, see Figure 38 and Table 3, by using the velocity rescaling thermostat and the program in GROMACS, *mdrun*.

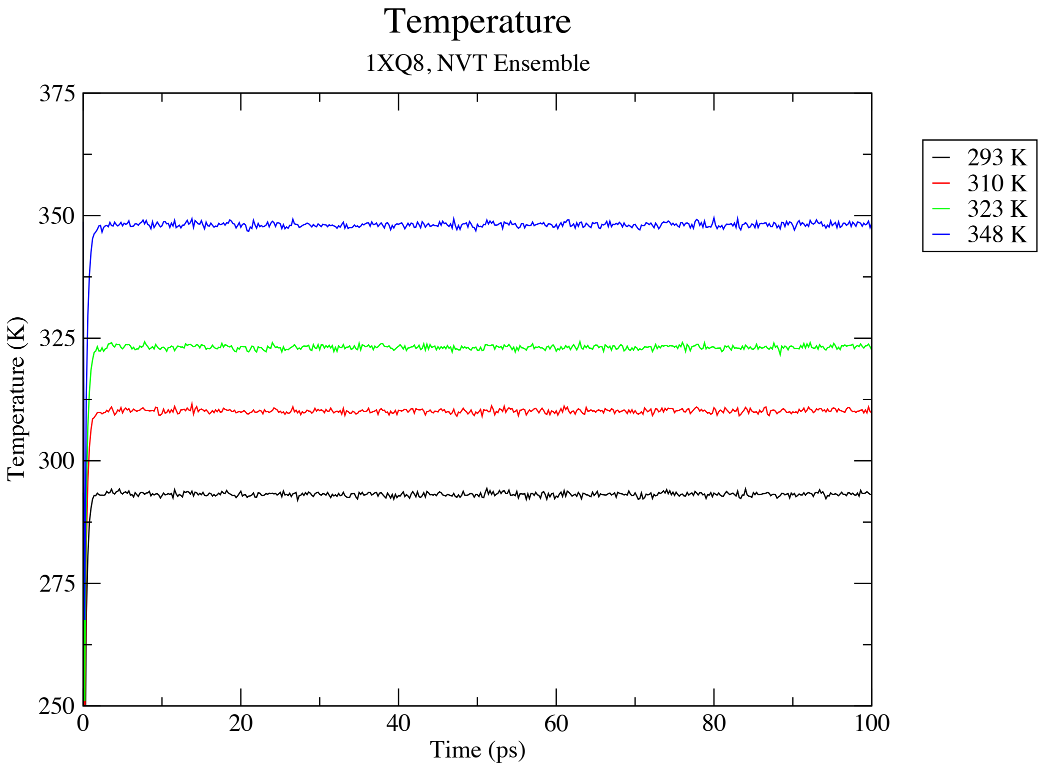

Figure 38. Temperatures for four different simulation runs.

The resulting configurations of α-synuclein in the four different systems are illustrated in Figure 39. There is not much deviation amongst the structures.

Table 3. Average temperature and standard deviation associated with each simulation.

T_{sim}, K	<T>, K	σ
293	292.82	4.97
310	309.78	5.31
323	322.75	5.57
348	347.70	6.08

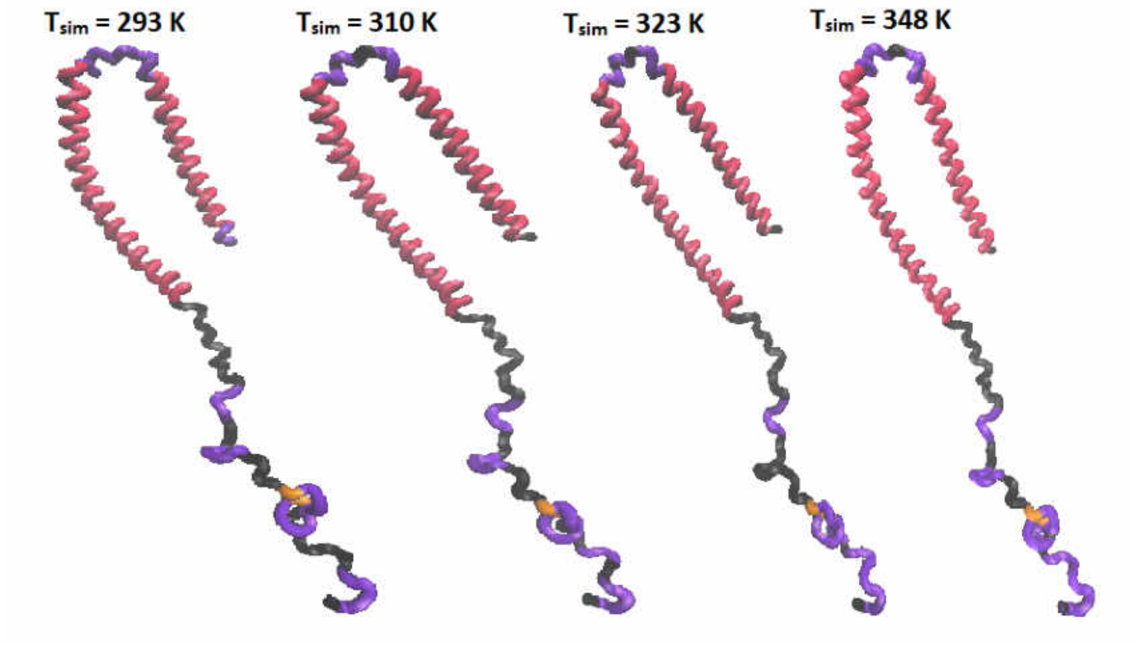

Figure 39. Configurations of α-synuclein at four different simulation runs. Here, the alpha helices are denoted by red, bet a bridges are denoted by orange, turns are denoted by violet, and coils are denoted by black.

4.2.3 NPT Equilibration

Pressure was also equilibrated, in all systems, to 1 bar by using the pressure coupling of the Parrinello-Rahman barostat. The GROMACS program, *mdrun*, was also utilized. There were large fluctuations of pressure, see Figure 40, due to it being a macroscopic property. This property can only be measured through a time average. The variation as well as the speed of oscillation depends on the number of atoms in the system (decreases by the number of particles), the type of pressure coupling used, and the value of pressure coupling constants.[13] Since all four different simulations were equilibrated to around 1 bar, see Table 4, only one plot was shown to illustrate this. In both pressure and temperature equilibration simulations, the number of steps was 5,000 which was equivalent to 100 ps.

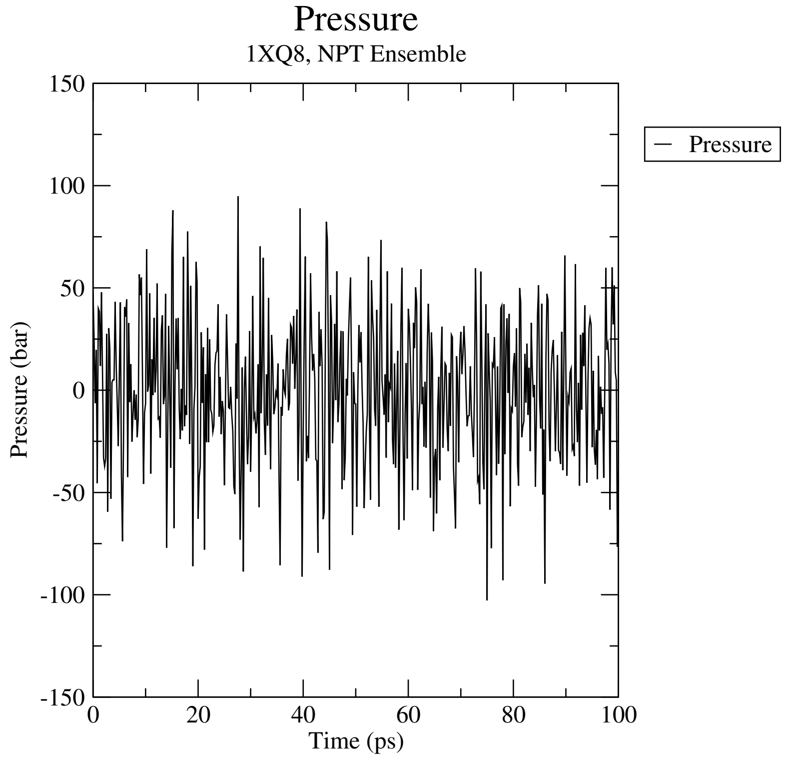

Figure 40. Pressure for the simulation at 310K.

Table 4. Average pressure and standard deviation associated with each simulation.

P_{sim}	<P>, bar	σ
P_{293}	1.05	34.50
P_{310}	0.974	34.82
P_{323}	0.989	34.96
P_{348}	1.0712	42.68

From the temperature and pressure data, density could be calculated using *g_energy*, see Figure 41 below. The results were as expected since at colder temperatures, i.e., 293 K, the protein would constrict, and, at higher temperatures, i.e., 348 K, the protein would become more relaxed, thus having a lower density.

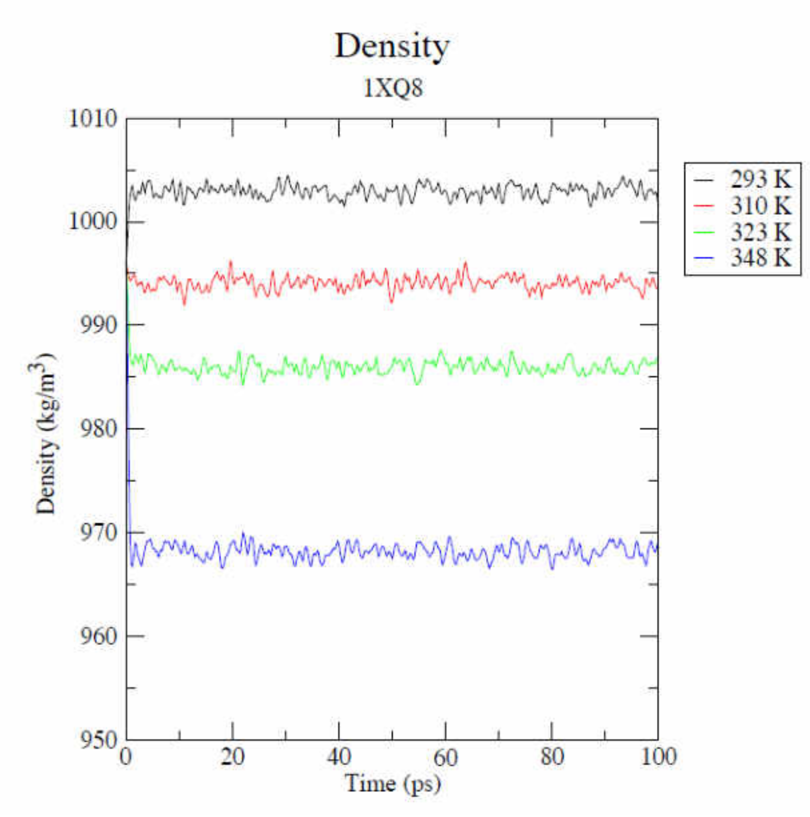

Figure 41. Density for all four simulations.

Table 5 displays the average and standard deviations of the different densities.

Table 5. Average density and standard deviation associated with each simulation.

T_{sim}, K	$< \rho >$, kg/m^3	σ
293	1002.91	0.72
310	994.08	0.61
323	986.02	0.88
348	968.29	1.86

4.3 Properties of α-synuclein

4.3.1 RMSD

For the RMSD calculation, we compared the backbone of the protein to the reference structure and the final structure, as can be seen in Figure 42. Our reference structure was that of the initial .pdb structure obtained from the Protein Data Bank once it was minimized in the equilibrated system, see Figure 36. The RMSD compared to the equilibrated α-synuclein indicates that the protein is not stable as their is no plateau.

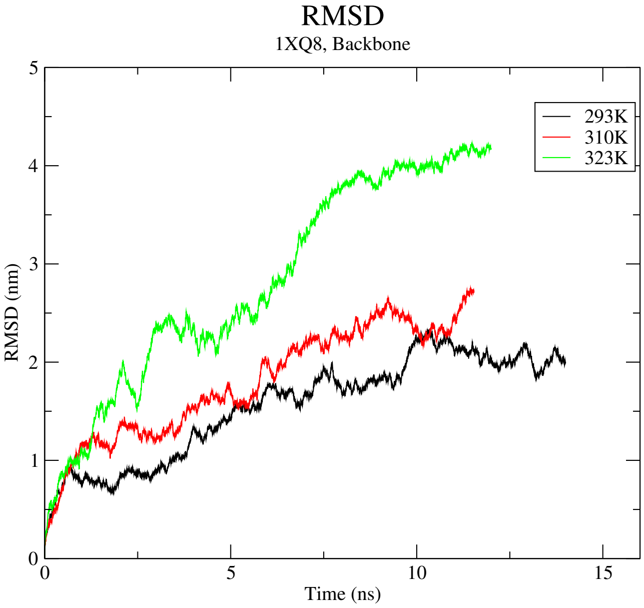

Figure 42. RMSD at four different temperatures.

4.3.2 Radius of gyration

The radius of gyration at four different temperatures is given in Figure 43. At all four simulations, α-synuclein appears to fold and unfold over time, resulting in an unstable conformation. This can clearly be seen in Figure 44 as the final configuration is shown for each simulation.

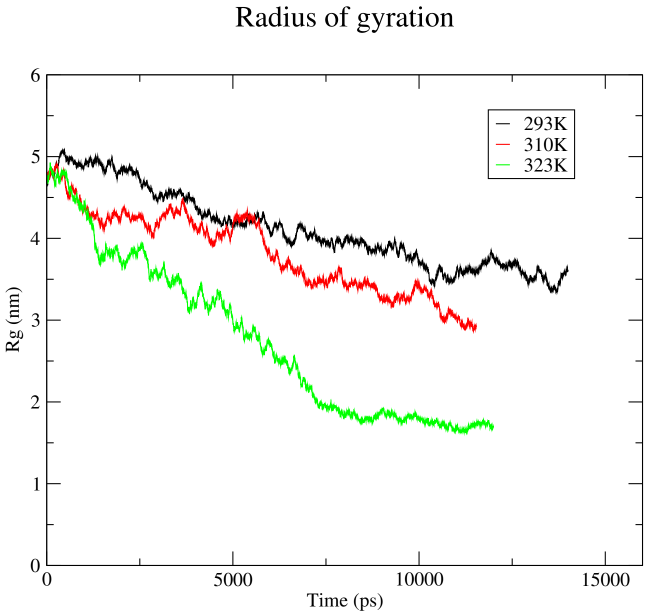

Figure 43. Radius of gyration at four different temperatures.

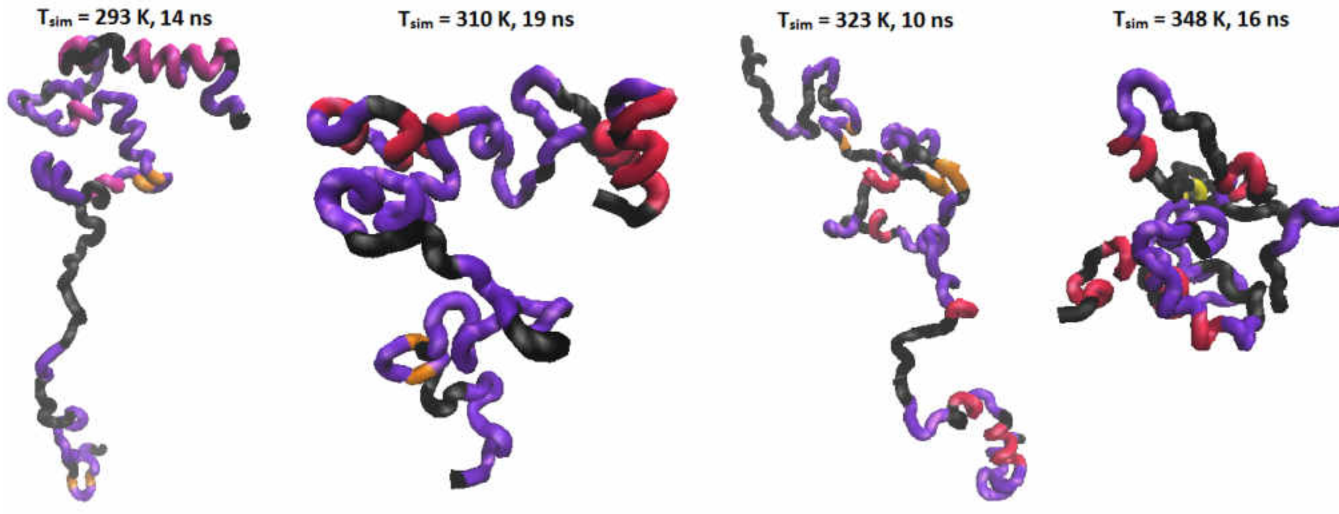

Figure 44. Ending configurations of α-synuclein.

4.4 Conclusion and future work

Molecular simulations of α-synuclein in water at four different temperatures, i.e., 293 K, 310 K, 323 K, and 348 K, were studied using GROMACS, a molecular dynamics package. Energy minimization was first used to ensure no steric clashes or inappropriate geometries for the electroneutral system. The potential energy plateaued to around $-1.025x10^9$ kJ mol^{-1}. Energy minimization was followed by equilibration of both temperature and pressure, using a correct ensemble, which allowed for the determination of density. Molecular dynamics were then employed to study the trajectory of the protein. Analysis showed the RMSD of all four proteins at the different temperatures were not stable compared to that of the equilibrated protein. The radius of gyration indicated that the protein was folding and unfolding.

In the future, we hope to simulate the aggregation of α-synuclein in an aqueous environment. This would be done through Wang-Landau (WL) sampling with Monte Carlo (MC) simulations. Furthermore, we intend to simulate α-synuclein in a lipid bilayer, since this is where it is naturally found, Figure 45. Lipid parameters have been written and can be easily incorporated within GROMACS. Molecular dynamics could then be used to study the trajectory of the protein through time. Finally, aggregation could be observed within the bilayer system using WL sampling and MC simulations.

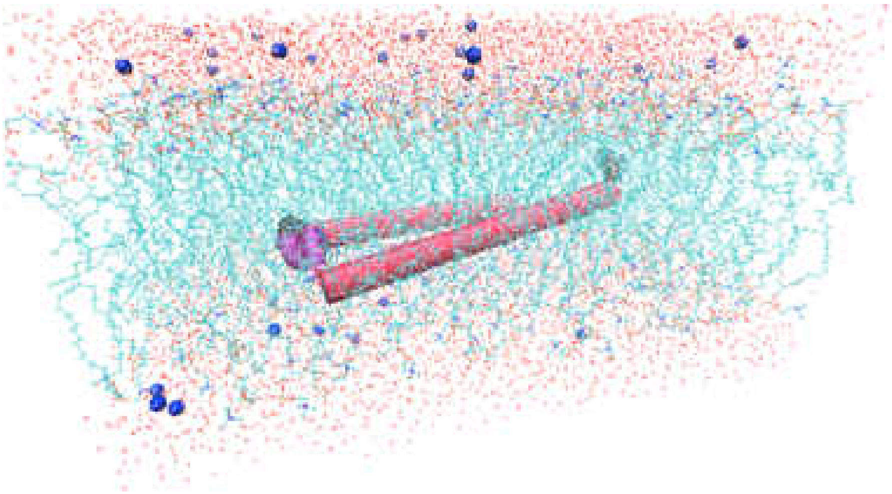

Figure 45. Future work involving α-synuclein, a libid bilayer, water, and ions.

CHAPTER V

DRUG DELIVERY FOR NEURODEGENERATIVE DISEASE

5.1 Case study: Amantadine

As mentioned previously in the Introduction, there have been no cures for any of the neurodegenerative diseases mentioned, only drugs that help slow the progression and manage symptoms. An array of different drugs have been proposed for the controlling of symptoms of Parkinson's disease. One such class of drugs are the aminodamantanes. It was thought, from the 1960s to the late 1980s, that these drugs managed symptoms of PD through dopaminomimetic activity. It was not until the 1990s that a new mechanism, and, therefore, a new therapeutic approach appeared, i.e. N-methyl-D-aspartate (NMDA) receptor antagonism.[92]

The aminodamantane's, such as amantadine (Figure 46), role in Parkinson's disease is due to its inhibition of NMDA receptors,[93] see Figure 47. This receptor, which is a specific type of ionotropic glutamate receptor, is found in the basal ganglia; it is important for the general nature of the central nervous system and could have an impact on learning and memory.[94] This type of receptor is an object of interest for the development of drugs for Parkinson's disease because of the critical dopamine-glutamate interactions.[95] NMDA receptors respond to glutamate (an essential excitatory transmitter existing in the brain) and are termed based on their selective agonist, N-methyl-D-aspartate.[96] When amantadine binds to this receptor, it causes a blockage in the channel's receptors.[97–100] This, then, causes the channel gates to close at a higher rate resulting in an impediment of current flow through the receptor's channels.[101]

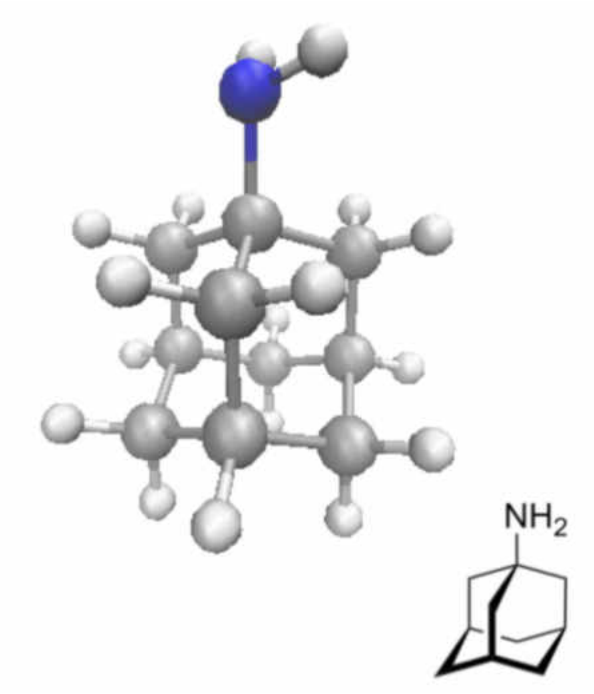

Figure 46. Amantadine, also known as 1-aminoadamantane.

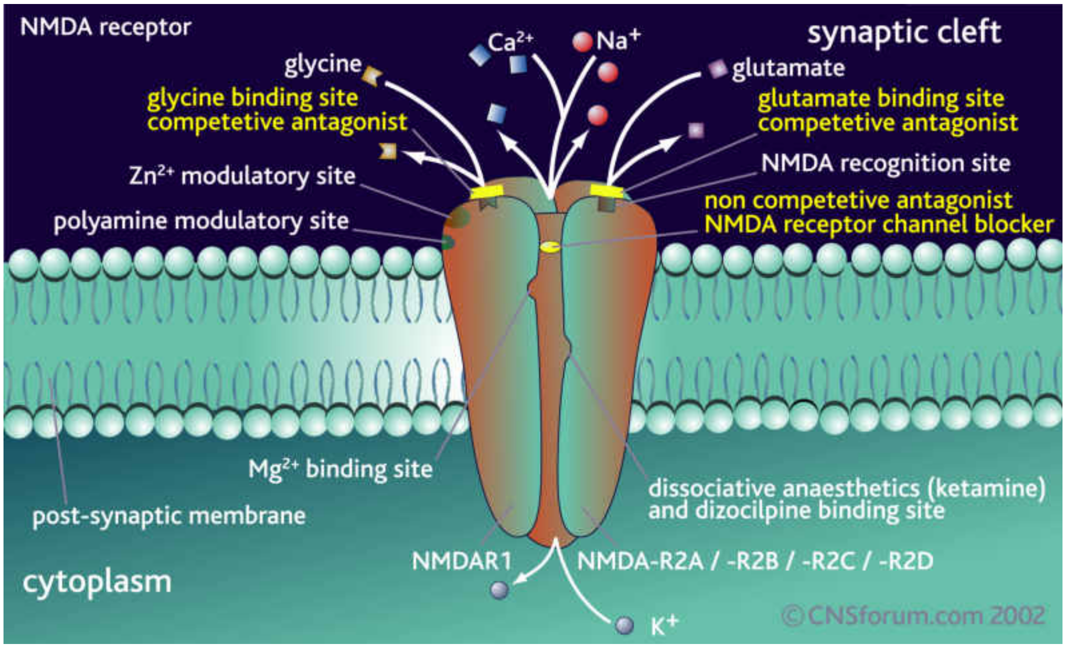

Figure 47. NMDA receptor. This receptor can be influenced by a number of antagonists including: competitive antagonists at the glycine and glutamate binding sites, as well as non-competitive NMDA receptor channel blockers. When an antagonist binds to either the glycine or glutamate site, the channel is blocked from activation and opening.[20]

Single walled carbon nanotubes (SWCNs) have been used in the drug delivery system (DDS) because of the advancement of the carbon nanotube (CNT) solubility. CNTs, themselves, have large inner volume resulting in the possibility of being nano-drug carriers or nanovectors for drug delivery.[102–105] SWCNs are able to be used with various drugs and proteins because of their ability to be chemically functionalized. The nanotubes also have a particular size and shape that enables them to selectively cross biological barriers allowing them to be a great resource for DDS applications.[102,106–108]

Four SWCNs were selected in order to study the affects of adsorption and diffusion within the nanomaterial: SWCN (8,8), SWCN (12,12), SWCN (16,16), and SWCN (20,20), with diameters ranging from 10.9 $\AA$ to 27.1 $\AA$. SWCNs can be thought of as wrapping a one-atom-thick layer of graphene into a seamless tube. The way the carbon nanotubes are rolled can result in different shapes, and, therefore, a naming system using a pair of indices (n,m) occurred. Figure 48 shows the naming convention for these nanoporous structures. One structure that can be produced is the zigzag (n,0) structure, Figure 49. This develops when the carbon-carbon bonds are parallel to the cylinder's axis and creates an open end, "zig-zag" pattern. In Figure 48, this could be represented by rolling (0,0) to (7,0), creating SWCN (7,0). The next structure that can be produced is the armchair arrangement, see Figure 49. This occurs when n equals m creating carbon-carbon bonds that are perpendicular to the cylinder's axis. For example, in Figure 48, one would roll (0,0) to a point represented by $n = m$, e.g., (5,5). This nanomaterial would then be labeled as SWCN (5,5). Both of these structures are classified as achiral since they have a superimposable mirror image. The last structure that could be produced are chiral, Figure 49, when n does not equal m and neither indices are equal to 0. For example, rolling (0,0) to (5,2) would produce SWCN (5,2).[21]

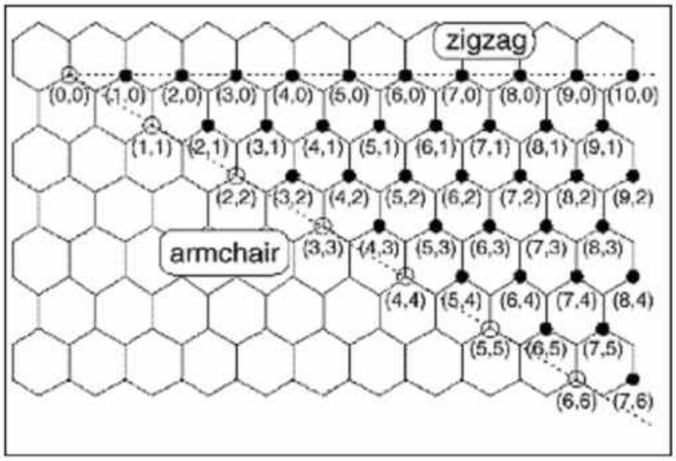

Figure 48. Labeling convention for SWCNs.[21]

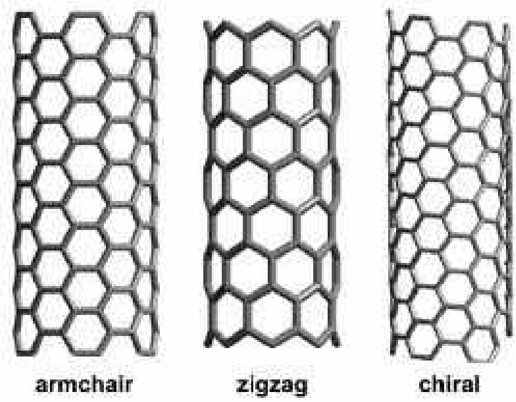

Figure 49. SWCNs possible shapes. Armchair occurs when n = m resulting in carbon-carbon bonds being perpendicular to the tube's axis. Zigzag (n,0) where the carbon-carbon bonds are parallel to the tube's axis. Chiral occurs when m $\neq$ n.[22]

The transport mechanism of these SWNCs have been difficult to explore experimentally. We, therefore, have studied the adsorption and diffusion of these nanomaterials.

5.2 Adsorption and diffusion in single-walled carbon nanotubes

5.2.1 Expanded Wang-Landau simulations

Due to the difficulty of studying large drug molecules adsorbing into nanoporous materials, different methods have arised. One such method is finding the preferred orientations and/or positions of the molecule and then inserting it into the nanomaterial.[84] Another method, which we used, was the Expanded Wang-Landau (EWL) simulations. We chose this method because it allows for (1) a uniform sampling of the number of molecules, i.e. amantadine, adsorbed in a porous material, i.e single-walled carbon nanotubes (SWCN), (2) the insertion/deletion of large molecules by dividing the insertion and deletion of molecules into a large number of steps and (3) the determination of a highly accurate estimate of the grand canonical partition function for the system. The method, which will be illustrated below, has been shown to produce accurate results recently.[109,110]

In order to describe Expanded Wang-Landau (EWL) simulations, Wang-Landau (WL) sampling will first be described.

Wang-Landau sampling allows for all number of particles N to be sampled evenly. In traditional Monte Carlo (MC) methods, Boltzmann sampling is used. The drawback of this is that there is a very low probability for the system to have an order parameter between the vapor and liquid states, which causes sampling to be uneven as the simulation would get stuck in one state or the other, Figure 50. The use of WL sampling allows us to bias the probability function which then has the same probability function value over the specified range, Figure 51. This, then, allows for all states of the system to be sampled equally.[111,112]

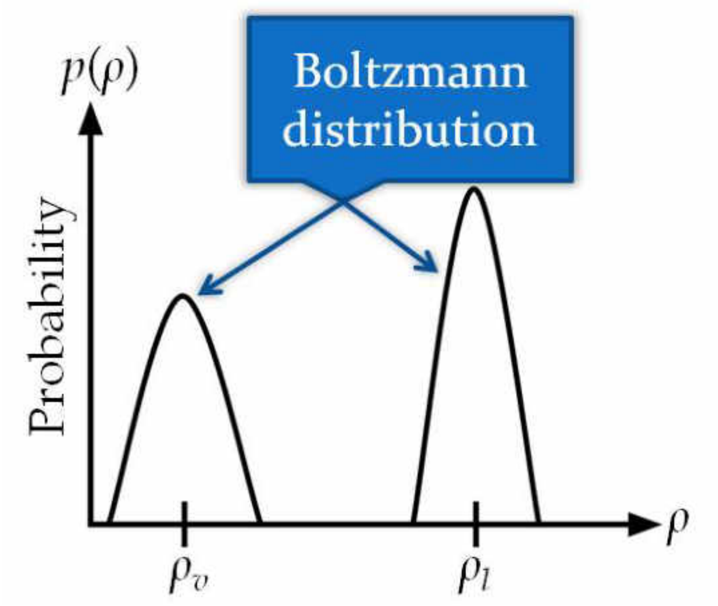

Figure 50. Boltzmann sampling.

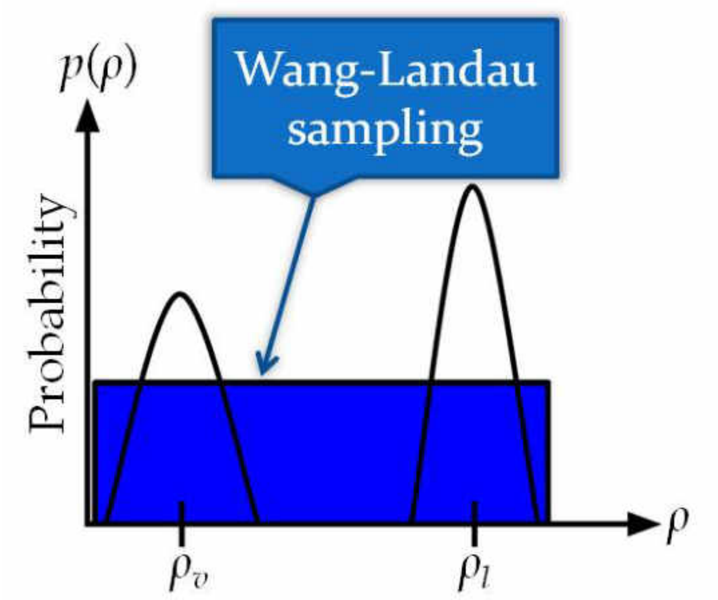

Figure 51. Wang-Landau sampling.

The Expanded Wang-Landau method uses the simplified expanded grand-canonical (SEGC) partition function so the derivation of this function will first be described.

The canonical partition function is described by equation 5.1

$$Q(N,V,T) = \frac{V^N}{N!\Lambda^{3N}} \int \exp(-\beta U(\Gamma)) d\Gamma \tag{5.1}$$

where there are N molecules, at volume V, temperature T, $\Lambda = h/\sqrt{2\pi m k_B T}$ is the thermal de Broglie wavelength and $U(\mathbf{\Gamma})$ is the internal energy of the system of N molecules in the specific configuration, $\mathbf{\Gamma}$. The integration is performed over $\mathbf{\Gamma}$, thus over the coordinates of the N molecules of the system.

We can then use equation 5.1 to obtain the grand canonical partition function given in equation 5.2.

$$\Theta(\mu,V,T) = \sum_{N=0}^{\infty} Q(N,V,T)\exp(\beta\mu N), \tag{5.2}$$

where μ is the chemical potential, $\beta = \frac{1}{k_B T}$.

In order to obtain the expanded grand canonical (EGC) partition function, insertion and deletion of molecules needed to be accounted for through an efficient scheme, which would result in a change of N. In order to do this, insertion and deletion were divided into M different stages, where M is an integer. The system, during the simulation, would have both N molecules as well as a fractional particle in stage l, where $0 \leq l \leq M-1$. The fractional molecule is allowed to interact with full particles by a coupling parameter ξ_l. Throughout the simulation, l is allowed to change causing N to change as well. In order to account for the fractional molecule plus N molecules, the grand-canonical partition function was expanded. To do this, (i) the sum over all N and l were taken instead of only N and (i) a weighting function, denoted by ψ (l,N), is added. The weighting function is normally determined through numerical calculations[113–115] which allows for the optimization of the sampling of the system around a specific value N. The expanded grand canonical (EGC) partition function[116–122] is then given by equation 5.3

109

$$\Theta_{\mathrm{EGC}}(\mu, V, T) = \sum_{N=0}^{\infty} \sum_{l=0}^{M-1} Q(N, V, T, l)\mathrm{exp}(\beta\mu N + \psi(l, N)) \tag{5.3}$$

where $Q(N,V,T,l)$ is the canonical partition function for a system of N full particles and a fractional particle at stage $l > 0$ given by

$$Q(N, V, T, l) = \frac{V^{N+1}}{N!\Lambda^{3N}\Lambda_l^3} \int \mathrm{exp}(-\beta U(\Gamma))d\Gamma \tag{5.4}$$

where Λ_l is the thermal de Broglie wavelength for a fractional particle in stage l > 0 and Γ represents a specific configuration of the system made up of N full particles and a fractional particle.

Simplifying the EGC partition factor enables the simulations to converge faster. To do this, we let $\psi(l,N) = 0$ for all l and N since the weighting function has no affect on the grand-canonical partition function because the Wang-Landau sampling is used, i.e., samples uniformly. Also, we let the mass of the fractional particle be the same as the full particle, and therefore $\Lambda_l = \Lambda$. The partition function of a simplified grand canonical (SEGC) ensemble can then be seen in equation 5.5

$$\Theta_{\mathrm{SEGC}}(\mu, V, T) = \sum_{N=0}^{\infty} \sum_{l=0}^{M-1} Q(N, V, T, l)\mathrm{exp}(\beta\mu N) \tag{5.5}$$

where the canonical partition function for or $0 < l < M$ is as follows

$$Q(N, V, T, l) = \frac{V^{N+1}}{N!\Lambda^{3N}} \int \mathrm{exp}(-\beta U(\Gamma))d\Gamma \tag{5.6}$$

The Wang-Landau sampling is now applied within the SEGC partition function. Having a fractional particle l, there are two possibilities for the joint Boltzmann distribution depending on the value of l,

$$p(\Gamma, N, l) = \begin{cases} \frac{V^{N+1}\exp(\beta\mu N - \beta U(\Gamma))}{N!\Lambda^{3(N+1)}\Theta_{SEGC}(\mu,V,T)} & \text{for } 0 \text{ ¡ l ¡ M} \\ \\ \frac{V^{N}\exp(\beta\mu N - \beta U(\Gamma))}{N!\Lambda^{3N}\Theta_{SEGC}(\mu,V,T)} & \text{for } \text{l} = 0 \end{cases} \tag{5.7}$$

Then, the probability distribution, $p(N, l)$, can be obtained by equation 5.8

$$p(N, l) = \int p(\Gamma, N, l) d\Gamma = \frac{Q(N, V, T, l)\exp(\beta\mu N)}{\Theta_{SEGC}(\mu, V, T)} \tag{5.8}$$

The biased distribution for $0 < l < M$ is then

$$\begin{aligned} p_{bias}(\Gamma, N, l) = \frac{p(\Gamma, N, l)}{p(N, l)} &= \frac{\frac{V^{N+1}\exp(\beta\mu N - \beta U(\Gamma))}{N!\Lambda^{3(N+1)}\Theta_{SEGC}(\mu,V,T)}}{\frac{Q(N,V,T,l)\exp(\beta\mu N)}{\Theta_{SEGC}(\mu,V,T)}} \\ &= \frac{V^{N+1}\exp(-\beta U(\Gamma))}{Q(N, V, T, l)N!\Lambda^{3(N+1)}} \end{aligned}$$

and the biased distribution for $l = 0$ is as follows

$$p_{bias}(\Gamma, N, l = 0) = \frac{p(\Gamma, N, l = 0)}{p(N, l = 0)} = \frac{\frac{V^{N}\exp(\beta\mu N - \beta U(\Gamma))}{N!\Lambda^{3N}\Theta_{SEGC}(\mu,V,T)}}{\frac{Q(N,V,T,l=0)\exp(\beta\mu N)}{\Theta_{SEGC}(\mu,V,T)}} = \frac{V^{N}\exp(-\beta U(\Gamma))}{Q(N, V, T, l = 0)N!\Lambda^{3N}} \tag{5.9}$$

The MC acceptance criterion from an old state ($\mathbf{\Gamma}_o$, N_o and fractional number l_o) to a new state ($\mathbf{\Gamma}_n$), N_n and l_n) is given generally by

$$acc(o \to n) = min\left[1, \frac{p_{bias}(\Gamma_n, N_n, l_n)}{p_{bias}(\Gamma_o, N_o, l_o)}\right] \tag{5.10}$$

Specifically, there are four different MC acceptance criteria depending on both the value of l and if the adsorbates are atoms or molecules. In our case, we deal with molecular fluids, so the internal degrees of freedom of rotation and vibration, q_{int} need to be accounted for. The acceptance criteria is then

$$acc(o \rightarrow n) = min\left[1, \frac{Q(N_o, V, T, l_o)V^{N_n} q_{int}^{N_n} N_o! \Lambda^{3N_o} \exp(-\beta U(\Gamma_n))}{Q(N_n, V, T, l_n)V^{N_o} q_{int}^{N_o} N_n! \Lambda^{3N_n} \exp(-\beta U(\Gamma_o))}\right] \tag{5.11}$$

The WL sampling algorithm in the SEGC ensemble now works by estimating the value of $Q(N, V, T, l)$ and visiting both values of N and fractions l. Two different histograms are kept. One histogram is used to keep track of the visited values of N while the other keeps track of the visited values of l. When the simulation has finished converging, $Q(N, V, T, l)$ is provided up to a multiplicative constant. Because $Q(N = 0, V, T, l = 0) = 1$, $Q(N, V, T, l)$ can then be obtained. The grand canonical partition function is then ascertained by using a Laplace transform as seen in equation 5.12

$$\Theta(\mu, V, T) = \sum_{N=0}^{\infty} Q(N, V, T, l = 0) \exp(\beta \mu N) \tag{5.12}$$

The use of EWL simulations allowed us to study adsorption of amantadine in single-walled carbon nanotubes (SWCNs) at T = 298 K.

Through EWL simulations, we found the absolute adsorbed of amantadine within the nanotube by equation 5.13

$$N_{ads} = \sum_{N=0}^{\infty} N p(N) \tag{5.13}$$

5.2.2 Adsorption isotherms for Amantadine

Amantadine loading can be seen in Figure 52 where the loading is denoted in mg of amantadine per gram of SWCN. The loading is expressed as a function of reduced pressure P/P_0 where P_0 is the vapor pressure of amantadine at 298 K.[123]

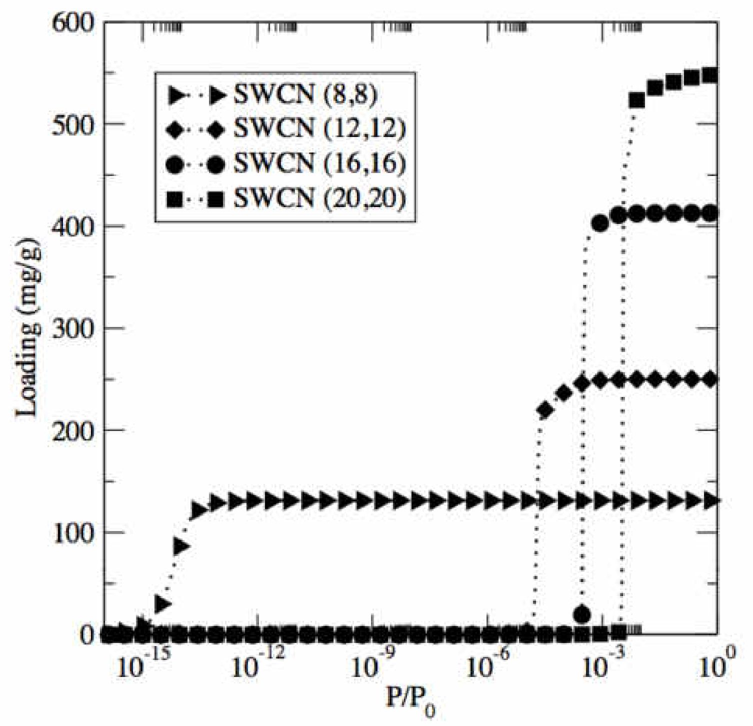

Figure 52. Adsorption isotherms of amantadine at T = 298K at four different SWCNs.

We can see by both Figure 53 and Table 6, that the amount adsorbed is dependent upon the diameter of the single-walled carbon nanotubes - the larger the diameter, the better the adsorption of amantadine. Looking at Figure 53, it is noted that as the diameter of the nanotube decreases, the isotherm step is shifted towards lower pressure. This effect can be seen especially when the SWCN becomes roughly the same size as the amantadine molecule, i.e., SWCN (8,8). This is consistent with other findings when GCMC simulations were used to study the adsorption of N2 in single-walled carbon nanotubes.[124]

Table 6. Loading based off of different SWCNs.

SWCNs	Diameter ($\mathring{A}$)	Loading (mg/g)
SWCN (8,8)	10.9	131
SWCN (12,12)	16.3	250
SWCN (16,16)	21.7	412
SWCN (20,20)	27.1	554

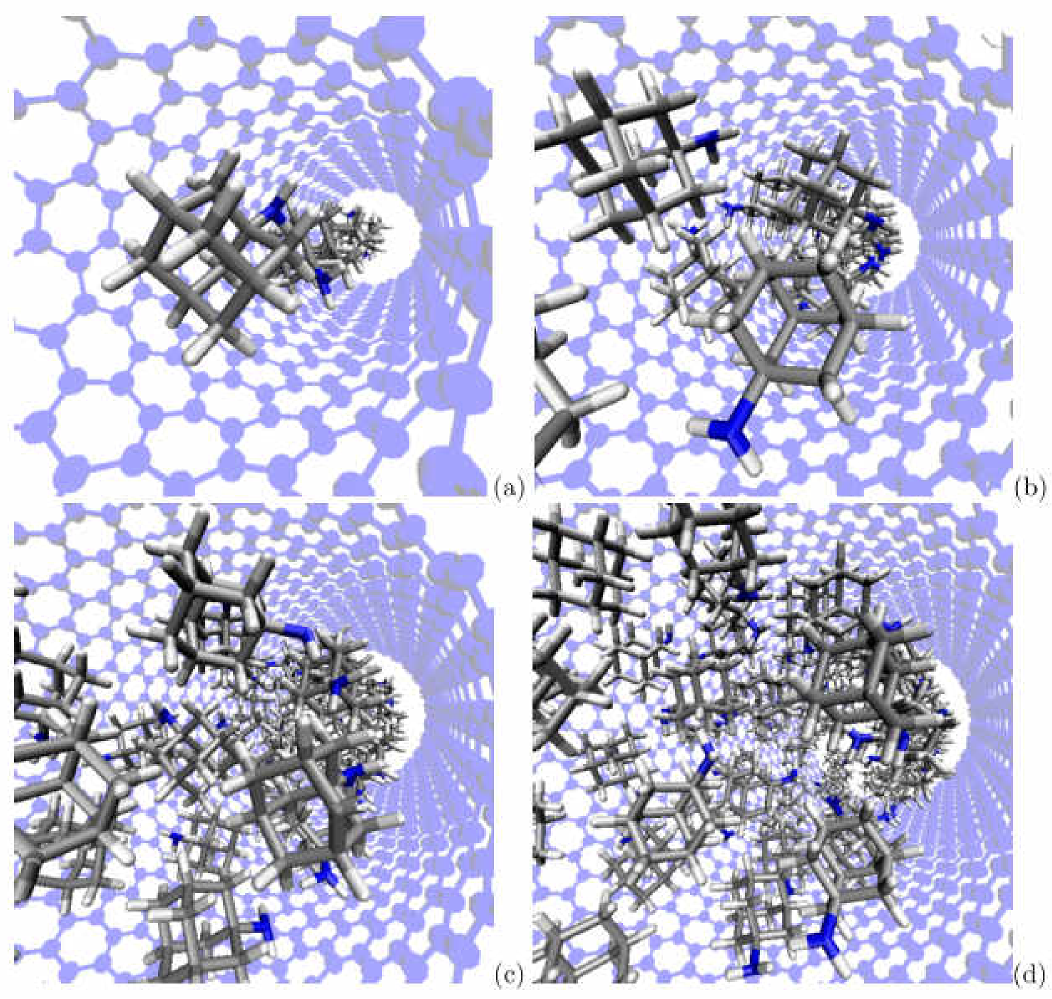

Figure 53. Amantadine adsorbed in single-walled carbon nanotubes at T = 298 K and P = P_0 for (a) SWCN (8,8), (b) SWCN (12,12), (c) SWCN (16,16), and (d) SWCN (20,20).

To explore amantadine's structure when acting as the adsorbed fluid, we plotted the density profiles obtained at all four nanotubes at the saturation pressure, see Figure 54. The density profiles were found using equation

$$\rho(R) = \frac{< N(R, R + \Delta R) >}{\pi((R + \Delta R)^2 - R^2)L} \tag{5.14}$$

where $< \mathrm{N(R,R + \Delta R)} >$ is the average number of amantadine molecules within the cylindrical shell, enclosed between the two cylinders of radii R and R + ΔR. The radius interval ΔR is equal to one hundredth of the nanotube's radius.

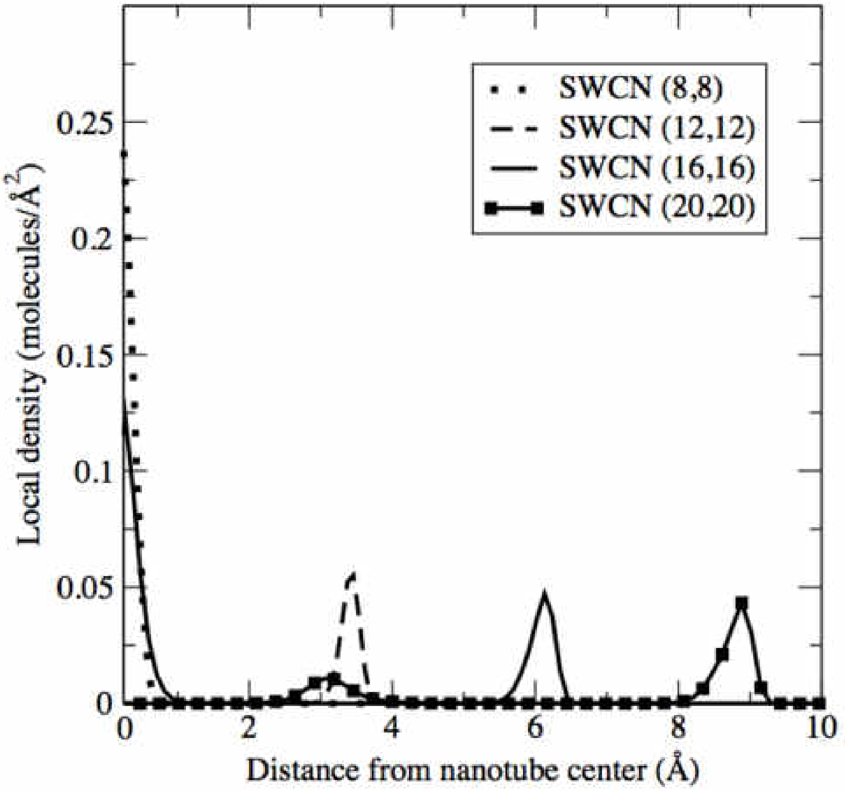

Figure 54. Density profiles for amantadine adsorbed in single-walled carbon nanotubes at T = 298 K and P = P_0 for (a) SWCN (8,8), (b) SWCN (12,12), (c) SWCN (16,16), and (d) SWCN (20,20).

We observed a single peak for SWCN (8,8) located on the central axis of the nanobute indicating that the system was organized in a "line" along the axis of the nanotube. This can also be seen in Figure 55a. Another single peak for SWCN (12,12) was observed where the maximum occurred at 3.3 $\AA$. However, the structure that resulted, Figure 55b, was different when compared to SWCN (8,8). For the smallest diameter, i.e., SWCN (8,8), amantadine is organized into a single layer, taking the shape of the cylindrical tube. When the diameter is allowed to increase, the confined amantadine's structure evolves. Looking at both SWCN (16,16) and SWCN (20,20), it was observed through the density profile, Figure 54c and d, that both nanotubes featured two peaks. For SWCN (16,16), one peak occurred at the central axis of the nanotube while the other occurred around 6.1 $\AA$. The resulting structure, seen in Figure 55c, shows a bilayer-type of structure - one layer occurring along the the "line" of the axis of the nanotube and the other occurring as a cylindrical layer around the first. The density profile of SWCN (20,20), Figure 54d, indicates one peak occurred at 3 $\AA$ while the other peak occurred at 8.5 $\AA$. The corresponding structure can then be seen in Figure 55d. Comparing SWCN (16,16) and SWCN (20,20), the larger diameter, i.e., SWCN (20,20), contained more than the bilayer structure that was observed for SWCN (16,16), but it was not large enough to result in two cylindrical layers around the single layer at the axis.

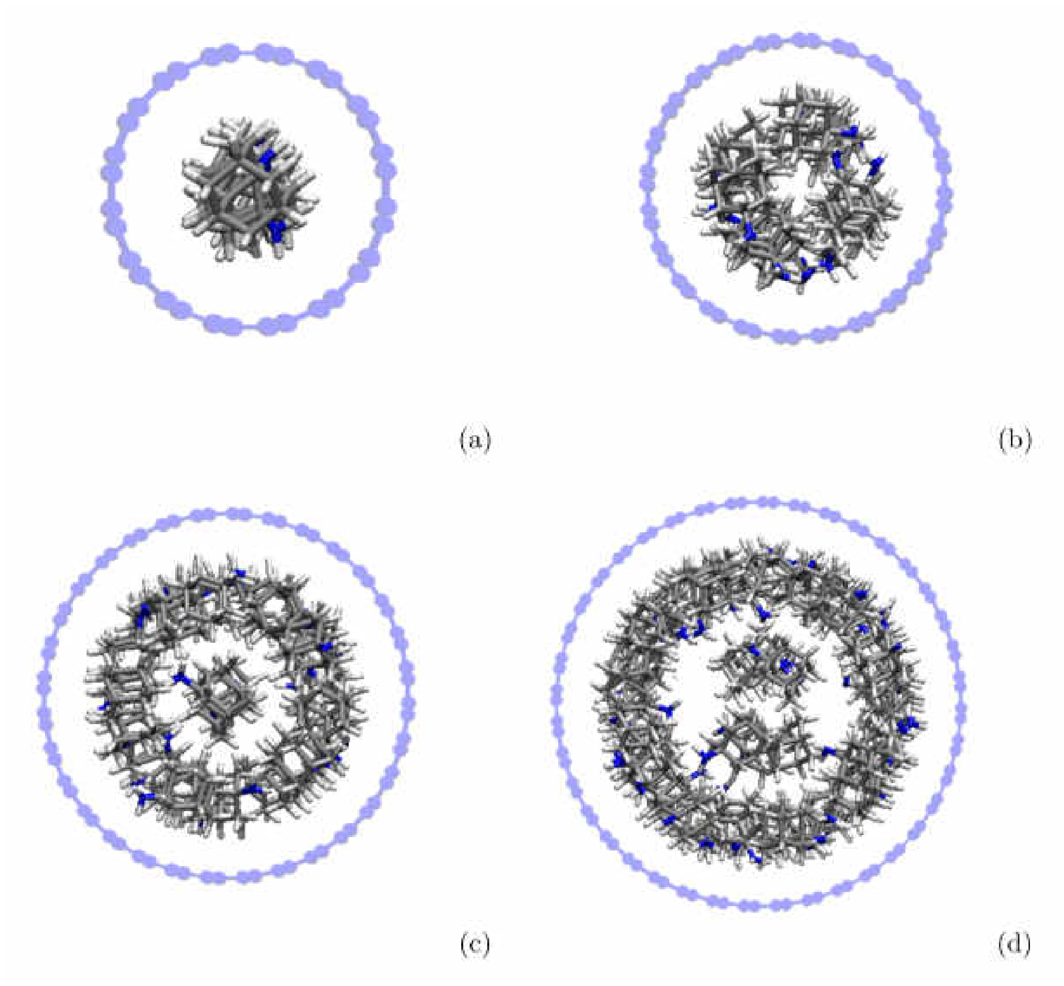

Figure 55. Structures for amantadine when adsorbed in single-walled carbon nanotubes at T = 298 K and P = P0 for (a) SWCN (8,8), (b) SWCN (12,12), (c) SWCN (16,16), and (d) SWCN (20,20).

5.2.3 Diffusion process for Amantadine

Next, we looked at the diffusion process using molecular dynamics. During the simulations, the axial positions, i.e., along the z-axis, were stored and later used when the post-processing of the simulations in order to characterize self-diffusion occurred. Self-diffusion in single-walled carbon nanotubes is defined by equation 5.15 as the long-time self-diffusivity D_s in the axial (z) direction.

$$\lim_{t\to\infty}\left\langle \frac{1}{N}\sum_{i=1}^{N}\left[z_i(t)-z_i(0)\right]^2\right\rangle = 2D_s t \tag{5.15}$$

We plotted the average mean square displacement along the axis of SWCN (16,16) against time on a linear plot using various loadings of amantadine ranging from 47 mg/g to 280 mg/g, Figure 56a. At short times, we observed the expected behavior as the system was in the ballistic regime. At intermediate times, the system changed to being in the subdiffusive regime, as expected. Finally, the Fickian regime was ascertained. The Fickian regime is characterized when the mean square displacement shows linear variation against time. The slope is then related to the self-diffusivity D_s based on equation 5.15.

While in the Fickian regime, we calculated the turnover point as seen in equation 5.16.

$$\frac{d\,log < (z(t)-z(0))^2 >}{d\,log\,t} = 1 \pm 0.15 \tag{5.16}$$

We then used this to graph the turnover points for three different loadings of amantadine in SWCN (16,16), Figure 56b.

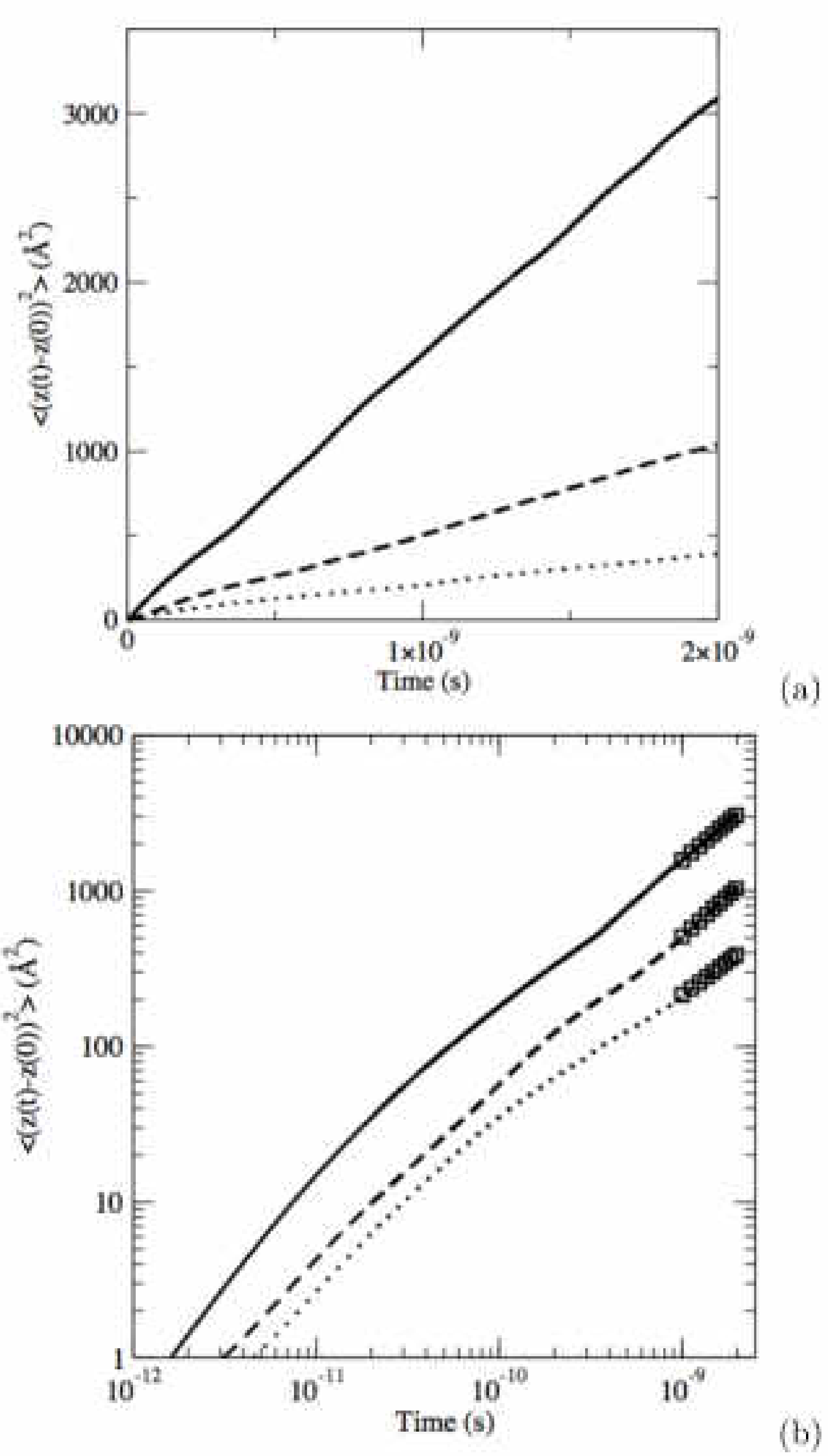

Figure 56. (a) RMSDs at various loadings of amantadine within SWCN (16,16). (b) LOG-LOG plot of RMSDs showing the expected linear behavior (shown as squares) in the Fickian regime.

Finally, we looked at the self-diffusivity D_s for amantadine at SWCN (8,8), SWCN (12,12), SWCN (16,16), and SWCN (20,20) at various loadings (in mg of amantadine per g of SWCN), Figure 57. Generally, for all four nanotubes, as the loading increases, the self-diffusivity D_s decreases. This conceptually makes sense because as the density of the fluid increases, there would be less diffusion for amantadine. It was found that the rate at which D_s decreases is dependent upon the loading for the larger diameter nanotubes, i.e. SWCN (16,16) and SWCN (20,20). The self-diffusivity of SWCN (16,16) decreases dramatically until the loading is around 230 mg/g. Comparing the loading of 47 g/mg to that of 234 mg/g, the D_s at 234 mg/g is divided by three. As the loading is increased at 234 mg/g, D_s decreases at a more moderate rate. Between loadings of 234 mg/g and 412 mg/g, D_s decreases by 25%. When looking at SWCN (20,20), D_s decreases dramatically until the loading si around 300 mg/g. Comparing the loadings of 150 mg/g to 300 mg/g, D_s is divided by 2.3. D_s then decreases at a moderate rate at higher loadings, i.e. from 300 mg/g to 524 mg/g; decreasing by 15%. The various changes in the rate at which D_s decreases, can be attributed to the structural changes that are taking place within the nanotubes. When loading is increased, the adsorbed amantadine molecules transition from being in a single layer system to being in a bilayer system. Being in a single layer structure as the loading is increased causes an increase in the density of the outer cylindrical layer resulting in the dramatic decrease of D_s. Once the transition occurs and the system has a bilayer structure, amantadine molecules aggregate to the center of the nanotube. When loading is increased, there is a much more moderate decrease in D_s.

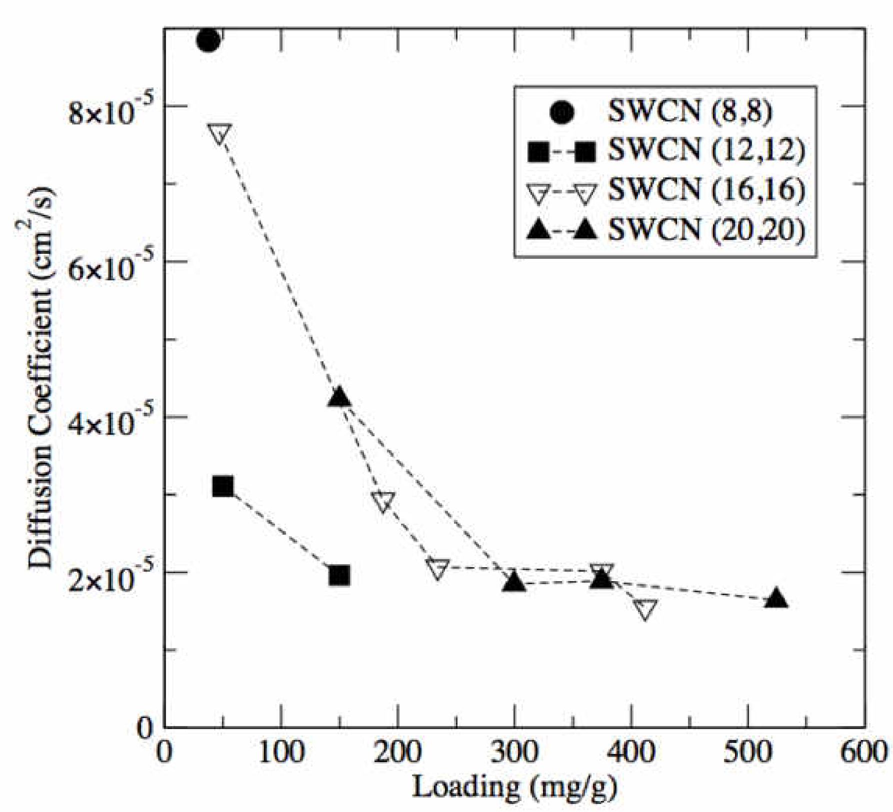

Figure 57. Self-diffusivities of amantadine adsorbed at the four different SWCNs as a function of the loading.

5.3 Conclusion and future work

Expanded Wang-Landau (EWL) simulations were used to study the adsorption of amantadine in four different single walled carbon nanotubes (SWCNs). EWL simulations allowed for the determination of the grand canonical partition function, which then assisted in the computation of thermodynamic properties. Depending upon the diameter and the amantadine loading, different structures arose. Monolayers, which occurred for high loadings and small SWCNs, i.e., SWCN (8,8) and SWCN (12,12), were characterized as either a line of amantadine along the central axis or a cylindrical layer appearing close to the inner surface. The second structure that appeared were bilayers. Bilayers, which occurred for high loadings and large SWCN, i.e., SWCN (16,16) and SWCN (20,20), were characterized as having both a line of amantadine along the central axis and a cylindrical layer close to the inner surface of the nanotube. Finally, self-diffusion was studied to look at amantadine's transport. For larger SWCNs, there was a dramatic decrease in the rate of self-diffusion as a function of increased amantadine loading followed by a moderate decrease. This was associated to a transition of the amantadine fluid from a monolayer to a bilayer.

The molecular simulations applied to this system resulted in accurately predicting adsorption and diffusion properties of amantadine at the four SWCNs. We hope to further this study by looking at the interactions of dopamine as well as looking further into the drug delivery of amantadine to the NMDA receptor.

CHAPTER VI

GENERAL CONCLUSIONS

Molecular simulations are a useful tool for the study of biological systems. Due to the costliness and difficulty of experimental studies, molecular simulations provide a great advantage in that they can help predict what phenomena will occur. From this outcome, experimental studies can use the knowledge to fine tune their techniques. We have applied molecular simulations to key aspects of neurodegenerative diseases where we studied α-synuclein in an aqueous environment as well as amantadine in single-walled carbon nanotbues (SWCNs). It was found for α-synuclein that at four different temperatures, the protein was unstable, folding and unfolding through time. For amantadine, different configurations of amantadine were observed depending upon the diameter of the nanotube as well as the loading. The self-diffusion coefficients changed dramatically when the transition of the amantadine fluid from a monolayer to a bilayer occurred.

REFERENCES

1. Lang, A. E.; Lozano, A. M. Parkinson's Disease. *N. Engl. J. Med.* **1998**, *339*, 1044–1053.

2. Blennow, K.; de Leon, M. J.; Zetterberg, H. Alzheimer's Disease. *Lancet* **2006**, *368*, 387–403.

3. Lücking, C. B.; Brice, A. Alpha-Synuclein and Parkinson's Disease. *Cell. Mol. Life Sci.* **2000**, *57*, 1894–1908.

4. Paleček, E.; Ostatná, V.; Masaík, M.; Bertoncini, C. W.; Jovin, T. M. Changes in Interfacial Properties of α-Synuclein Preceding its Aggregation. *Analyst* **2008**, *133*, 76–84.

5. Cookson, M. R. α-Synuclein and Neuronal Cell Death. *Mol. Neurodegener.* **2009**, *4*, 9.

6. Gibb, W. R.; Lees, A. J. The Relevance of the Lewy Body to the Pathogenesis of Idiopathic Parkinson's Disease. *J. Neurol. Neurosurg. Psychiatry* **1988**, *51*, 745–752.

7. Lee, H.-J.; Patel, S.; Lee, S.-J. Intravesicular Localization and Exocytosis of α-Synuclein and its Aggregates. *J. Neurosci.* **2005**, *25*, 6016–6024.

8. Desplats, P.; Lee, H.-J.; Bae, E.-J.; Patrick, C.; Rockenstein, E.; Crews, L.; Spencer, B.; Masliah, E.; Lee, S.-J. Inclusion Formation and Neuronal Cell Death through Neuron-to-Neuron Transmission of α-synuclein. *Proc. Natl. Acad. Sci.* **2009**, *106*, 13010–13015.

9. Tsigelny, I. F.; Bar-On, P.; Sharikov, Y.; Crews, L.; Hashimoto, M.; Miller, M. A.; Keller, S. H.; Platoshyn, O.; Yuan, J. X.-J.; Masliah, E. Dynamics of α-synuclein Aggregation and Inhibition of Pore-Like Oligomer Development by β-Synuclein. *FEBS J.* **2007**, *274*, 1862–1877.

10. Nguyen, H. D.; Hall, C. K. Molecular Dynamics Simulations of Spontaneous Fibril Formation by Random-Coil Peptides. *Proc. Natl. Acad. Sci. USA* **2004**, *101*, 16180–16185.

11. Ma, B.; Nussinov, R. Stabilities and Conformations of Alzheimers β-Amyloid Peptide Oligomers (Aβ1622, Aβ1635, and Aβ1035): Sequence Effects. *Proc. Natl. Acad. Sci.* **2002**, *99*, 14126–14131.

12. Lindahl, E. *Introduction to Molecular Dynamics with GROMACS: Molecular Modeling Course 2007: Simulation of Lysozyme in Water*; 2007.

13. Apol., E.; Apostolov, R.; Berendsen, H. J. C.; Buuren, A. v.; Bjelkmar, P.; van Drunen, R.; Feenstra, A.; Groenhof, G.; Kasson, P.; Larsson, P.; Al., E. *GROMACS USER MANUAL: Version 4.5.4.*; 2010.

14. Kinetic Theory: Atomic and Molecular Explanation of Pressure and Temperature. `http://cnx.org/content/m42217/latest/?collection=col11406/latest(accessedApr29,2013).`

15. Force fields.

16. Harmonic Potential. `http://cat.middlebury.edu/~chem/chemistry/class/physical/quantum/help/harmonic/harmonic.html`.

17. Dihedral angle.

18. Silbey, R. J.; Alberty, R. A.; Bawendi, M. G. *Physical Chemistry John Wiley & Sons*; 2005.

19. Water Structure and Behavior. Water Models.

20. CNSforum. NMDA antagonist. `http://www.cnsforum.com/imagebank/item/hrl\_rcpt\_sys\_NMDA\_antag/default.aspx(accessedOct7,2013).`

21. AZoNano. Carbon Nanotubes - Structure, Naming and Properties of Carbon Nanotubes (Buckytubes). `http://www.azonano.com/article.aspx?ArticleID=983(accessedOct8,2013).`

22. Bhagat, R. Yale National Initiative. Nanotechnology and Clean Water: How Safe is Our Drinking Water?

23. Berendsen, H. J. C.; Grigera, J. R.; Straatsma, T. P. The Missing Term in Effective Pair Potentials. *J. Phys. Chem.* **1987**, *91*, 6269–6271.

24. Parkinson, J. *An Essay on the Shaking Palsy*; Printed by Whittingham and Rowland for Sherwood, Neely, and Jones, 1817.

25. National Institute of Neurological Disorders and Stroke: Parkinson's Disease Backgrounder. `Http://www.ninds.nih.gov/disorders/parkinsons\_disease/parkinsons\_disease\_backgrounder.htm(accessedJun30,2013).`

26. U.S. Library of Medicine: Parkinson's disease. `http://www.ncbi.nlm.nih.gov/pubmedhealth/PMH0001762/(accessedJun30,2013).`

27. Moore, D. J.; West, A. B.; Dawson, V. L.; Dawson, T. M. Molecular Pathophysiology of Parkinson's Disease. *Annu. Rev. Neurosci.* **2005**, *28*, 57–87.

28. Gelb, D. J.; Oliver, E.; Gilman, S. Diagnostic Criteria for Parkinson Disease. *Arch .Neurol.* **1999**, *56*, 33–39.

29. Antonini, A. Levodopa in the Treatment of Parkinsons Disease: An Old Drug Still Going Strong. *Clin. Interv. Aging* **2010**, *5*, 229–238.

30. Mckeith, I.; Mintzer, J.; Aarsland, D.; Burn, D.; Chiu, H.; Cohen-Mansfield, J.; Dickson, D.; Dubois, B.; Duda, J. E.; Feldman, H.; Al., E. Review Dementia with Lewy Bodies. *Lancet Neurol.* **2004**, *3*, 19–28.

31. Baba, M.; Nakajo, S.; Tu, P.-h.; Lee, V. M.; Trojanowski, J. Q.; Iwatsubo, T. Aggregation of alpha-synuclein in Lewy bodies of Sporadic Parkinsons Disease and Dementia with Lewy bodies. *Am. J. Pathol.* **1998**, *152*, 879–884.

32. Aarsland, D.; Ballard, C. G.; Halliday, G. Are Parkinson's Disease with Dementia and Dementia with Lewy bodies the Same Entity? *J. Geriatr. Psychiatry Neurol.* **2004**, *17*, 137–145.

33. McKeith, I. G.; Galasko, D.; Kosaka, K.; Perry, E. K.; Kickson, D. W.; Hansen, L. A.; Salmon, D. P.; Lowe, J.; Mirra, S. S.; Byrine, E. J. Consensus Guidelines for the Clinical and Pathologic Diagnosis of Dementia with Lewy Bodies (DLB): Report of the Consortium on DLB International Workshop. *Neurology* **1996**, *47*, 1113–1124.

34. Byrne, E. J.; Lennox, G. G.; Godwin-Austen, R. B.; Jefferson, D.; Lowe, J.; Mayer, R. J.; Landon, M.; Doherty, F. J. Dementia Associated with Cortical Lewy Bodies: Proposed Clinical Diagnostic Criteria. *Dement. Geriatr. Cogn. Disord.* **1991**, *2*, 283–284.

35. Mebane-Sims, I. 2009 Alzheimer's Disease Facts and Figures. *Alzheimer's & Dementia* **2009**, *5*, 234–270.

36. O'Brien, J. T.; Erkinjuntti, T.; Reisberg, B.; Roman, G.; Sawada, T.; Pantoni, L.; Bowler, J. V.; Ballard, C.; DeCarli, C.; Gorelick, P. B.; Al., E. Vascular Cognitive Impairment. *Lancet Neurol.* **2003**, *2*, 89–98.

37. Brookmeyer, R.; Johnson, E.; Ziegler-Graham, K.; Arrighi, H. M. Forecasting the Global Burden of Alzheimer's Disease. *Alzheimer's & Dementia* **2007**, *3*, 186–191.

38. Alzheimer's Disease Research: A Program of the American Health Assistance Foundation. Frequently Asked Questions. `http://www.ahaf.org/alzheimers/questions/frequentlyasked.html(accessedNov28,2012)`.

39. Mayo Clinic. Alzheimer's disease. `http://www.mayoclinic.com/health/alzheimers-stages/AZ00041(accessedNov28,2012)`.

40. Hashimoto, M.; Hsu, L. J.; Xia, Y.; Takeda, A.; Sisk, A.; Sundsmo, M.; Masliah, E. Oxidative Stress Induces Amyloid-Like Aggregate Formation of NACP/α-Synuclein in Vitro. *NeuroReport* **1999**, *10*, 717–721.

41. DeKosky, S. T.; Scheff, S. W. Synapse Loss in Frontal Cortex Biopsies in Alzheimer's Disease: Correlation with Cognitive Severity. *Ann. Neurol.* **1990**, *27*, 457–464.

42. Masliah, E. The Role of Synaptic Proteins in Alzheimer's Disease. *Ann. NY Acad. Sci.* **2000**, *924*, 68–75.

43. Uversky, V. N. α-Synuclein Misfolding and Neurodegenerative Diseases. *Curr. Protein Pept. Sci.* **2008**, *9*, 507–540.

44. Maroteaux, L.; Campanelli, J. T.; Scheller, R. H. Synuclein : A Neuron-Specific Protein Localized to the Nucleus and Presynaptic Nerve Terminal. *J. Neurosci.* **1988**, *8*, 2804–2815.

45. Jensen, P. H.; Nielsen, M. S.; Jakes, R.; Dotti, C. G.; Goedert, M. Binding of α-Synuclein to Brain Vesicles is Abolished by Familial Parkinson's Disease Mutation. *J. Biol. Chem.* **1998**, *273*, 26292–26294.

46. Davidson, W. S.; Jonas, A.; Clayton, D. F.; M., G. J. Stabilization of Alpha-Synuclein Secondary Structure upon Binding to Synthetic Membranes. *J. Biol. Chem.* **1998**, *273*, 9443–9449.

47. Stefanis, L.; Kholodilov, N. G.; Burke, R. E.; A., G. L. Regulation of Synuclein-1 in Response to NGF Treatment in Rat Pheochromocytoma PC12 Cells. *Soc. Neurosci.* **1999**, *25*, 27–13.

48. Hsu, L. J.; Mallory, M.; Xia, Y.; Veinbergs, I.; Hashimoto, M., Y.; Yoshimoto, M.; Thal, L. J.; Saitoh, T.; Masliah, E. Expression Pattern of Synucleins (Non-Aβ Component of Alzheimer's Disease Amyloid Precursor Protein/α-Synuclein) During Murine Brain Development. *J. Neurochem.* **1998**, *71*, 338–344.

49. Bayer, T. A.; Jäkälä, P.; Hartmann, T.; Egensperger, R.; Buslei, R.; et Al., F. P. Neural Expression Profile of α-Synuclein in Developing Human Cortex. *NeuroReport* **1999**, *10*, 2799–2803.

50. Abeliovich, A.; Schmitz, Y.; Fariñas, I.; Choi-Lundberg, D.; Ho, W. H.; Castillo, P. E.; Shinsky, N.; Verdugo, J. M. G.; Armanini, M.; Ryan, A.; Al., E. Mice Lacking α-Synuclein Display Functional Deficits in the Nigrostriatal Dopamine System. *Neuron* **2000**, *25*, 239–252.

51. Fumitaka, K.; Suzuki, M.; Naoki, S.; Go, K.; Ohta, E.; Tamura, K.; Maruyama, H.; Ichikawa, T. Stimulatory Effect of α-synuclein on the Tau-Phosphorylation by GSK-3β. *FEBS J.* **2011**, *278*, 4895–4904.

52. Krüger, R.; Kuhn, W.; Müller, T.; Woitalla, D.; Graeber, M.; Kösel, S.; Przuntek, H.; Epplen, J. T.; Schols, L.; Riess, O. AlaSOPro Mutation in the Gene Encoding αsynuclcin in Parkinson's Disease. *Nat. Genet.* **1998**, *18*, 106–108.

53. Polymeropoulos, M. H.; Lavedan, C.; Leroy, E.; Ide, S. E.; Dehejia, A.; Dutra, A.; Pike, B.; Root, H.; Rubenstein, J.; Boyer, R.; Al., E. Mutation in the α-Synuclein Gene Identified in Families with Parkinson's Disease. *Sci.* **1997**, *276*, 2045–2047.

54. Singleton, A. B.; Farrer, M.; Johnson, J.; Singleton, A.; Hague, S.; Kachergus, J.; Hulihan, M.; Peuralinna, T.; Durtra, A.; Nusbaum, R.; Al., E. α-Synuclein Locus Triplication Causes Parkinson's Disease. *Science* **2003**, *302*, 841.

55. Wood, S. J.; Wypych, J.; Steavenson, S.; Louis, J. C.; Citron, M.; Biere, A. L. α-synuclein Fibrillogenesis is Nucleation-Dependent IMPLICATIONS OF PARKINSON'S DISEASE. *J. Biol. Chem.* **1999**, *274*, 19509–19512.

56. Dikiy, I., Eliezer, D. Folding and Misfolding of Alpha-Synuclein on Membranes. *Biochim. Biophys. Acta.* **2012**, *1818*, 1013–1018.

57. Goldberg, M. S.; Lansbury, P. T. J. Is There a Cause-and-Effect Relationship Between α-synuclein Fibrillation and Parkinson's Disease? *Nat. Cell Biol.* **2000**, *2*, E115–E119.

58. L., N.; J., W. S.; S., S.; Y., J.; M., W. G.; D., A.; Kaufman, S. A.; Martin, F.; Sitney, K.; Denis, P.; Al., E. Both Familial Parkinsons Disease Mutations Accelerate α-Synuclein Aggregation. *J. Biol. Chem.* **1999**, *274*, 9843–9846.

59. A., C. K.; Lee, S. J.; Rochet, J. C.; Ding, T. T.; Williamson, R. E.; Lansbury, P. T. J. Acceleration of Oligomerization, not Fibrillization, is a Shared Property of Both Alpha-Synuclein Mutations Linked to Early-Onset Parkinsons Disease: Implications for Pathogenesis and Therapy. *Proc. Natl. Acad. Sci. USA* **2000**, *97*, 571–576.

60. Crowther R. A., Jakes R., S. M. G.; M., G. Synthetic Filaments Assembled from C-Terminally Truncated Alpha-Synuclein. *FEBS Lett.* **1998**, *436*, 309–312.

61. Sofic, E.; Riederer, P.; Heinsen, H.; Beckmann, H.; Reynolds, G. P.; Hebenstreit, G.; Youdim, M. B. H. Increased iron (III) and Total Iron Content in Post Mortem Substantia Nigra of Parkinsonian Brain. *J. Neural Transmiss.* **1988**, *74*, 199–205.

62. R., P. S.; Ju-Hyun, L.; H., K. D.; S., C. C.; S., K. Y. Self-Oligomerization of NACP, the Precursor Protein of the Non-Amyloid β/A4 protein (Aβ) Component of Alzheimers Disease Amyloid, Observed in the Presence of a C-Terminal Aβ fragment (residues 2535). *FEBS Lett.* **1998**, *421*, 73–76.

63. Hughes, A. J.; Daniel, S. E.; L., K.; Lees, A. J. Accuracy of Clinical Diagnosis of Idiopathic Parkinson's disease. A Clinico-Pathological Study of 100 Cases. *J. Nerol. Neurosurg. Psychiatry* **1992**, *55*, 181–184.

64. E., D. P.; M., T. V. Phase and Electron Microscopic Observations of Lewy Bodies and Melanin Granules in the Substantia Nigra and Locus Coeruleus in Parkinson's Disease. *J. Neuropathol. Exp. Neurol.* **1965**, *24*, 398–414.

65. Braak, H.; Tredici, K. D.; Rüb, U.; de Vos, R. A. I.; Jansen Steur, E. N. H.; Braak, E. Staging of Brain Pathology Related to Sporadic Parkinsons Disease. *Neurobiol. Aging* **2003**, *24*, 197–211.

66. Li, J.-Y.; Englund, E.; Holton, J. L.; Soulet, D.; Hagell, P.; Lees, A. J.; Lashley, T.; Quinn, N. P.; Rehncrona, S.; Björklund, A.; Al., E. Lewy Bodies in Grafted Neurons in Subjects with Parkinson's Disease Suggest Host-To-Graft Disease Propagation. *Nat. Med.* **2008**, *50*, 501–503.

67. Kordower, J. H.; Chu, Y.; Hauser, R. A.; Freeman, T. B.; Olanow, C. W. Lewy Body-Like Pathology in Long-Term Embryonic Nigral Transplants in Parkinsons Disease. *Nat. Med.* **2008**, *14*, 504–506.

68. George, J. M.; Jin, H.; Woods, W. S.; Clayton, D. F. Characterization of a Novel Protein Regulated During the Critical Period for Song Learning in Zebra Finch. *Neuron* **1995**, *15*, 361–372.

69. He-Jin, L.; Choi, C.; Lee, S.-J. Membrane-Bound α-Synuclein Has a High Aggregation Propensity and the Ability to Seed the Aggregation of the Cytosolic Form. *J. Biol. Chem. Chem* **2002**, *277*, 671–678.

70. Borghi, R.; Marchese, R.; Negro, A.; Marinelli, L.; Forloni, G.; Zaccheo, D.; Abbruzzese, G.; Tabaton, M. Full Length α-Synuclein is Present in Cerebrospinal Fluid from Parkinson's Disease and Normal Subjects. *Neurosci. Lett.* **2000**, *287*, 65–67.

71. El-Agnaf, O. M.; Salem, S.; Paleologou, K. E.; Cooper, L. J.; Fullwood, N. J.; Gibson, M. J.; Curran, M. D.; Court, J. A.; Mann, D. M.; Ikeda, S.-I.; Al., E. α-Synuclein Implicated in Parkinsons Disease is Present in Extracellular Biological Fluids, Including Human Plasma. *FASEB J* **2003**, *17*, 1945–1947.

72. Rubartelli, A.; Cozzolino, F.; Talio, M.; Sitia, R. A Novel Secretory Pathway for Interleukin-1 Beta, a Protein Lacking a Signal Sequence. *EMBO J.* **1990**, *9*, 1503–1510.

73. Elliott, G.; OHare, P. Intercellular Trafficking and Protein Delivery by a Herpesvirus Structural Protein. *Cell* **1997**, *88*, 223–233.

74. Lee, H.-J.; Suk, J.-E.; Bae, E.-J.; Lee, J.-H.; Paik, S. R.; Lee, S.-J. Assembly-Dependent Endocytosis and Clearance of Extracellular a-Synuclein. *Int. J. Biochem. Cell Biol.* **2008**, *40*, 1835–1849.

75. Mendez, I.; Viñuela, A.; Astradsson, A.; Mukhida, K.; Hallett, P.; Robertson, H.; Tierney, T.; Holness, R.; Dagher, A.; Trojanowski, J. Q.; Al., E.

Dopamine Neurons Implanted into People with Parkinsons Disease Survive without Pathology for 14 years. *Nat. Med.* **2008**, *14*, 507–509.

76. Lee, S.-J. Origins and Effects of Extracellular α-synuclein: Implications in Parkinson's Disease. *J. Mol. Neurosci.* **2008**, *34*, 17–22.
77. Ding, T. T.; Lee, S. J.; Rochet, J. C.; Lansbury, P. T. J. Annular Alpha-Synuclein Protofibrils are Produced When Spherical Protofibrils are Incubated in Solution or Bound to Brain-Derived Membranes. *Biochem.* **2002**, *41*, 10209– 10217.
78. Jean-Christophe, R.; Fleming, O. T.; Conway, K. A.; Ding, T. T.; Volles, M. J.; Lashuel, H. A.; Bieganski, R. M.; Lindquist, S. L.; Lansbury, P. T. Interactions Among α-Synuclein, Dopamine, and Biomembranes: Some Clues for Understanding Neurodegeneration in Parkinsons Disease. *J. Mol. Neurosci.* **2004**, *23*, 1–2.
79. Ulmer, T. S.; Bax, A.; Cole, N. B.; Nussbaum, R. L. Structure and Dynamics of Micelle-Bound Human α-Synuclein. *J. Biol. Chem.* **2005**, *280*, 9595–9603.
80. Serio, T. R.; Cashikar, A. G.; Kowal, A. S.; Sawicki, G. J.; Moslehi, J. J.; Serpell, L.; Arnsdorf, M. F.; Lindquist, S. L. Nucleated Conformational Conversion and the Replication of Conformational Information by a Prion Determinant. *Science* **2000**, *289*, 1317–1321.
81. Balbach, J. J.; Ishii, Y.; Antzutkin, O. N.; Leapman, R. D.; Rizzo, N. W.; Dyda, F.; Reed, J.; Tycko, R. Amyloid Fibril Formation by Aβ16-22, a Seven-Residue Fragment of the Alzheimers β-Amyloid Peptide, and Structural Characterization by Solid State NMR. *Biochem.* **2000**, *39*, 13748–13759.
82. Santini, S.; Mousseau, N.; Derreumaux, P. In Silico Assembly of Alzheimer's Aβ16-22 Peptide into β-Sheets. *J. Am. Chem. Soc.* **2004**, *126*, 11509–11516.
83. GROMACS., G. F. F. F. A. GROMACS. Fast. Flexible. Free. About GROMACS. `http://www.gromacs.org/About\_Gromacs`.
84. Frenkel, D.; Smit, B. *Understanding Molecular Simulations*; Academic Press, San Diego, CA, 2002.
85. Bussi, G.; Donadio, D.; Parrinello, M. Canonical Sampling Through Velocity Rescaling. *J. Chem. Phys.* **2007**, *126*, 014101.
86. Parrinello, M.; Rahman, A. Polymorphic Transitions in Single Crystals: A New Molecular Dynamics Method. *J. Appl. Phys.* **1981**, *52*, 7182.
87. Nosé, S.; Klein, M. L. Constant Pressure Molecular Dynamics for Molecular Systems. *Mol. Phys.* **1983**, *50*, 1055–1076.

88. Kaminski, G. A.; Friesner, R. A.; Tirado-rives, J.; Jorgensen, W. L. Evaluation and reparametrization of the OPLS-AA force field for proteins via comparison with accurate quantum chemical calculations on peptides. *J. Phys. Chem. B* **2001**, *28*, 6474–6487.

89. Jorgensen, W. L.; Severance, D. Aromatic-aromatic interactions: free energy profiles for the benzene dimer in water, chloroform, and liquid benzene. *JACS* **1990**, *112*, 4768–4774.

90. Mackerell, A. D. Empirical force fields for biological macromolecules: overview and issues. *J. Comp. Chem* **2004**, *25*, 1584–1604.

91. Premier mémoire sur lélectricité et le magnétisme. *Histoire de lAcadémie Royale des Sciences* **1785**, 569–577.

92. Danysz, A.; Parsons, C. G.; Kornhuber, J.; Schmidt, W. J.; Quack, G. Aminoadamantanes as NMDA Receptor Antagonists and Antiparkinsonian Agents - Preclinical Studies. *Neurosci. Biobehav. R.* **1997**, *21*, 455–468.

93. Blanchet, P. J.; Metman, L. V.; Chase, T. N. Renaissance of amantadine in the treatment of Parkinsons disease. *Adv. Neurol.* **2003**, *91*, 251–257.

94. Trippier, P. C.; Jansen Labby, K.; Hawker, D. D.; Mataka, J. J.; Silverman, R. B. Target- and mechanism-based therapeutics for neurodegenerative diseases: strength in numbers. *Journal of medicinal chemistry* **2013**, *56*, 3121–47.

95. Hallett, P. J.; Standaert, D. G. Rationale for and use of NMDA receptor antagonists in Parkinson's disease. *Pharmacology & therapeutics* **2004**, *102*, 155–74.

96. Traynelis, S. F.; Wollmuth, L. P.; McBain, C. J.; Menniti, F. S.; Vance, K. M.; Ogden, K. K.; Hansen, K. B.; Yuan, H.; Myers, S. J.; Dingledine, R. Glutamate receptor ion channels: structure, regulation, and function. *Pharmacol. Rev.* **2010**, *62*, 405–496.

97. Kornhuber, J.; Bormann, J.; Hubers, M.; Rusche, K.; Riederer, P. Effects of the 1-amino-adamantanes at the MK-801-binding site of the NMDA-receptor-gated ion channel: a human postmortem brain study. *Eur. J. Pharmacol.* **1991**, *206*, 297–300.

98. Lupp, A.; Lucking, C. H.; Koch, R.; Jackisch, R.; Feuerstein, T. J. Inhibitory effects of the antiparkinsonian drugs memantine and amantadine on N-methyl-D-aspartate-evoked acetylcholine release in the rabbit caudate nucleus in vitro. *J. Pharmacol. Exp. Ther.* **1992**, *263*, 717–724.

99. Parsons, C. G.; Quack, G.; Bresink, I.; Baran, L.; Przegalinski, E.; Kostowski, W.; Krzascik, P.; Hartmann, S.; Danysz, W. Comparison of the

potency, kinetics and voltage-dependency of a series of uncompetitive NMDA re- ceptor antagonists in vitro with anticonvulsive and motor impairment activity in vivo. *Neuropharmacology* **1995**, *34*, 1239–1258.

100. Blanpied, T. A.; Boeckman, F. A.; Aizenman, E.; Johnson, J. W. Trapping channel block of NMDA-activated responses by amantadine andmemantine. *J. Neurophysiol.* **1997**, *77*, 309–323.

101. Blanpied, T. a.; Clarke, R. J.; Johnson, J. W. Amantadine inhibits NMDA receptors by accelerating channel closure during channel block. *The Journal of neuroscience : the official journal of the Society for Neuroscience* **2005**, *25*, 3312–22.

102. Bianco, A.; Kostarelos, K.; Prato, M. Applications of carbon nanotubes in drug delivery. *Curr. Opin. Chem. Biol.* **2005**, *9*, 674–679.

103. Klumpp, C.; Kostarelos, K. Functionalized carbon nanotubes as emerging nanovectors for the delivery of therapeutics. *BBA-Biomembranes* **2006**, *3*, 404–412.

104. Bhirde, A. A.; Patel, V.; Gavard, J.; Zhang, G.; Sousa, A. A.; Masedunskas, A.; Leapman, R. D.; Weigert, R.; Gutkind, J. S.; Rusling, J. F. Targeted killing of cancer cells in vivo and in vitro with EGF-directed carbon nanotube-based drug delivery. *ACS nano* **2009**, *3*, 307–316.

105. Pastorin, G.; Wu, W.; Wieckowski, S.; Briand, J. P.; Kostarelos, K.; Prato, M.; Bianco, A. Double functionalisation of carbon nanotubes for multimodal drug delivery. *Chem. Commun.* **2006**, *11*, 1182–1184.

106. Yang, W. R.; Thordarson, P.; Gooding, J. J.; Ringer, S. P.; Braet, F. Carbon nanotubes for biological and biomedical applications. *Nanotechnology* **2007**, *18*, 12.

107. Tasis, D.; Tagmatarchis, N.; Bianco, A.; Prato, M. Chemistry of carbon nanotubes. *Chem. Rev.* **2006**, *106*, 1105–1136.

108. Pastorin, G. Crucial functionalizations of carbon nanotubes for improved drug delivery: a valuable option. *Pharm. Res.* **2009**, *26*, 746–769.

109. Desgranges, C.; Delhommelle, J. Evaluation of the grand-canonical partition function using expanded Wang-Landau simulations. I. Thermodynamic properties in the bulk and at the liquid-vapor phase boundary. *J. Chem. Phys.* **2012**, *136*, 184107.

110. Desgranges, C.; Delhommelle, J. Evaluation of the grand-canonical partition function using expanded Wang-Landau simulations. II. Adsorption of atomic and molecular fluids in a porous material. *J. Chem. Phys.* **2012**, *136*, 184108.

111. Wang, F. G.; Landau, D. P. Efficient, multiple-range random walk algorithm to calculate the density of states. *Phys. Rev. Lett.* **2001**, *86*, 2050.

112. Wang, W. G.; Landau, D. P. Determining the density of states for classical statistical models: A random walk algorithm to produce a flat histogram. *Phys. Rev. E* **2001**, *64*, 056101.

113. Escobedo, F. A.; Abreu, C. R. On the use of transition matrix methods with extended ensembles. *J. Chem. Phys.* **2006**, *124*, 104110.

114. Trebst, S.; Huse, D. A.; Troyer, M. Optimizing the ensemble for equilibration in broad-histogram Monte Carlo simulations. *Phys. Rev. E* **2004**, *70*, 046701.

115. Shi, W.; Maginn, E. J. Improvement in molecule exchange efficiency in Gibbs ensemble Monte Carlo: Development and implementation of the continuous fractional component move. *J. Comput. Chem.* **2008**, *29*, 2520–2530.

116. Lyubartsev, A. P., Martsinovski, A. A., Shevkunov, S. V.; Vorontsov-Velyaminov, P. N. New approach to Monte Carlo calculation of the free energy: Method of expanded ensembles. *J. Chem. Phys.* **1992**, *96*, 1776.

117. Escobedo, F. A.; de Pablo, J. J. Expanded grand canonical and Gibbs ensemble Monte Carlo simulation of polymers. *J. Chem. Phys.* **1996**, *105*, 4391.

118. Abreu, C. R.; Escobedo, F. A. A general framework for non-Boltzmann Monte Carlo sampling. *J. Chem. Phys.* **2006**, *124*, 054116.

119. Singh, J. K.; Errington, J. R. Calculation of phase coexistence properties and surface tensions of n-alkanes with grand-canonical transition-matrix Monte Carlo simulation and finite-size scaling. *J. Chem. Phys. B* **2006**, *110*, 1369–1376.

120. Escobedo, F. A.; Martínez-Veracoechea, F. J. Optimized expanded ensembles for simulations involving molecular insertions and deletions. I. Closed systems. *J. Chem. Phys.* **2007**, *127*, 174103.

121. Escobedo, F. A. Optimized expanded ensembles for simulations involving molecular insertions and deletions. II. Open systems. *J. Chem. Phys.* **2007**, *127*, 174104.

122. Escobedo, F. A.; Martinez-Veracoechea, F. J. Optimization of expanded ensemble methods. *J. Chem. Phys.* **2008**, *129*, 154107.

123. Bazyleva, A. B.; Blokhin, A. V.; Kabo, A. G.; Kabo, G. J.; Emelyanenko, V. N.; Verevkin, S. P. Thermodynamic properties of 1-aminoadamantane. *J. Chem. Thermodyn.* **2008**, *40*, 509–522.

124. Arora, G.; Wagner, N. J.; Sandler, S. I. Adsorption and diffusion of molecular nitrogen in single wall carbon nanotubes. *Langmuir* **2004**, *20*, 6268–6277.